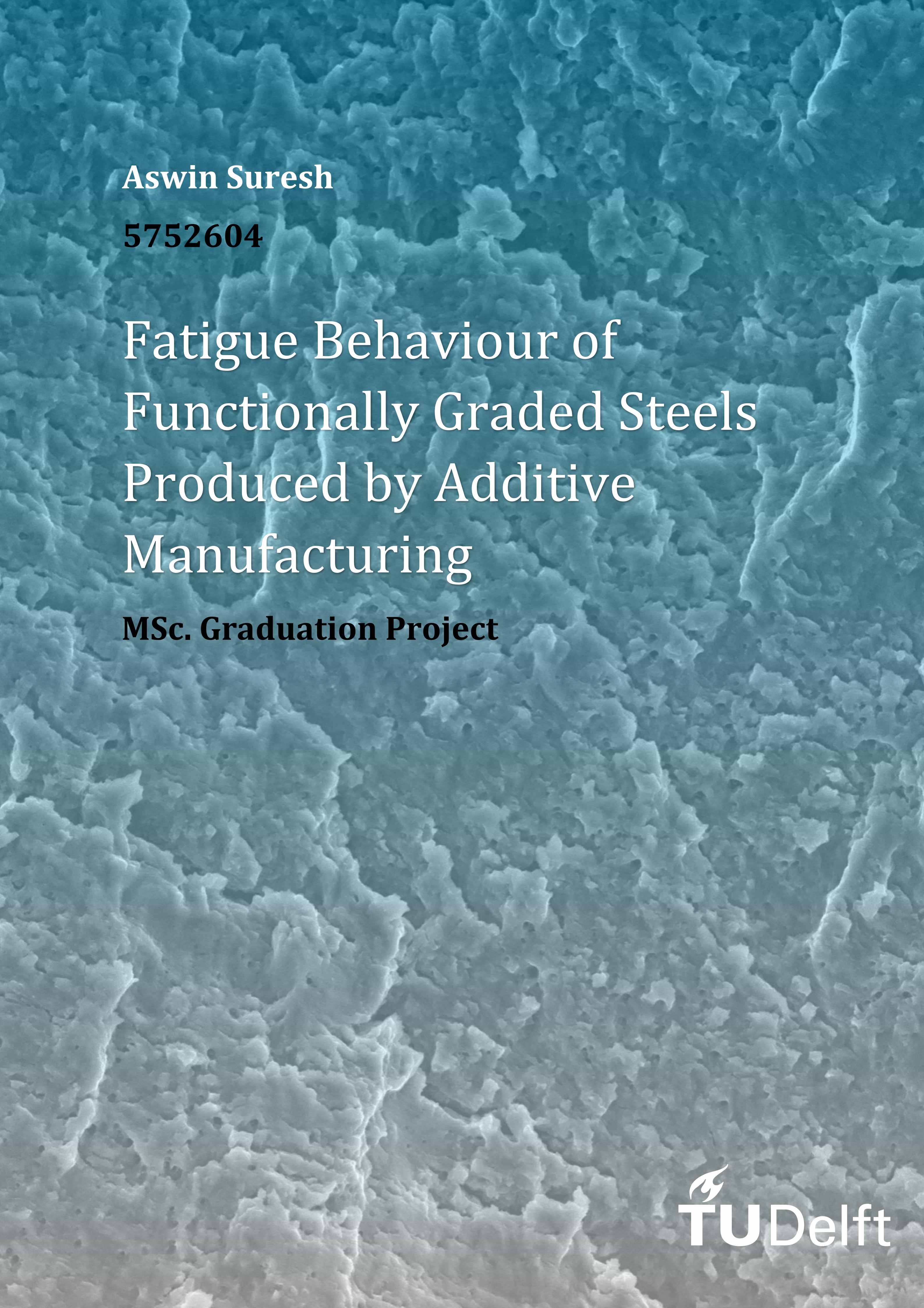

Aswin Suresh

5752604

Fatigue Behaviour of Functionally Graded Steels Produced by Additive Manufacturing

MSc. Graduation Project

Fatigue Behaviour of Functionally Graded Steels Produced by Additive Manufacturing

MSc. Graduation Project

By

Aswin Suresh
5752604

in partial fulfilment of the requirements for the degree of

Master of Science
in Materials Science and Engineering

at the Delft University of Technology,
to be defended publicly on May 30, 2024, at 10:30 am.

Supervisors:	Associate Prof. Dr. Vera Popovich ir. José Luis Galán Argumedo, PhD researcher
Thesis committee:	Associate Prof. Dr.ir. Marcel Hermans Associate Prof. Dr. Carey Walters

Abstract

Wire arc additive manufacturing (WAAM) can create large parts, due to its high deposition rate. WAAM can be used to create functionally graded materials (FGMs) such as a strong core of high strength low alloy (HSLA) steel and corrosion-resistant cladding of austenitic stainless (AUS) steel. However, HSLA and AUS steel are dissimilar metals with different microstructure and mechanical properties. Joining dissimilar metals with WAAM creates a complex interface with a different set of properties compared to parent materials. The current state of the art covers the microstructure, tensile properties, and hardness of such FGM. However, there is a lack of understanding about the fatigue properties at the interface. This study investigates the fatigue crack growth behaviour at the interface of ER70S-6 (HSLA steel) and ER316L (AUS steel). Initially, a benchmark study of the HSLA and AUS steel was done to obtain Paris parameters, threshold stress intensity range (ΔK_{th}), and hardness. HSLA steel showed 43 to 77% lower Paris slope parameters than AUS steel, which suggests a better fatigue resistance for HSLA steel. However, no significant difference in ΔK_{th} values was observed. The hardness of HSLA and AUS steel were 247.0±6.1 HV and 227.7±5.5 HV respectively, which suggests a correlation between hardness and fatigue resistance. Further analysis showed a power law relation between the Paris slope parameter and hardness for HSLA steel. This was attributed to the grain size. Smaller grain sizes improve fatigue resistance and increase hardness. Hence, hardness can be an indirect measure of fatigue resistance. Under constant ΔK experiments, AUS steel showed up to a 61.7% difference in fatigue crack growth rate (FCGR). The anisotropy in AUS steels is due to the large grain size in the range of 100 µm and the structure of the weld beads, resulting in heterogeneity. After the benchmark study, the graded materials were tested under similar conditions. The crack in the graded material grows from AUS steel to a 2 mm wide interface and then to HSLA steel. A variation of FCGR at the interface region was measured, notably 1) a decrease of 5.1E-05 to 6.1E-05 mm/cycle before the interface region, 2) a gradual increase of 5.5E-05 to 1.32E-04 mm/cycle within the interface region, and 3) a sudden increase of up to 3E-04 mm/cycle. To understand these behaviour microscopy, fractography, and electron backscatter diffraction (EBSD) analyses were utilised. The sudden increase of FCGR in HSLA steel was attributed to process-induced porous defects. The decrease of FCGR before the interface region was due to the increase in grain boundaries, secondary cracks, an increased crack closure effect, and martensite formation through transformation-induced plasticity (TRIP) in the interface region. The gradual acceleration of FCGR within the interface region was due to the martensite phases formed during solidification. The martensite formed during solidification had twice the hardness in comparison to HSLA steel. The martensite formed by the TRIP effect also resulted in 25-50% higher hardness near the crack flanks compared to the regions away from it. For the application of this FGM, the interface can act as a protective layer by reducing the FCGR. However, the martensite formed during solidification in the interface should be mitigated.

Acknowledgement

My first and sincere gratitude goes to my project supervisor Dr. Vera Popovich, for providing me with the opportunity to participate in this project and for offering constant support and an optimistic outlook when faced with challenges. Her guidance was vital to the progress made throughout the months. I sincerely believe that her feedback on planning, writing and presentation will play a significant role in my professional development throughout my career.

I could not have undertaken this journey without my daily supervisor ir. José Luis Galán Argumedo. My day-to-day interactions with him were full of discussions, clarifications, and debates. His support with the finite element analysis, material fabrication, and EBSD analysis was crucial for this project. His feedback on my writing has been vital for this work. I intend to learn and incorporate his enthusiasm and patience for my personal and professional development.

I also thank the thesis committee members, Dr.ir. Marcel Hermans and Dr. Carey Walters, for agreeing to be part of the committee and for taking the time to evaluate my work.

I am thankful to Elise Reinton for her utmost support with the test setup and programming. I am grateful to Dr.ir. Ton Riemslag for his support with the test setup and data processing. Both of their advice and recommendations were critical for the methodology development during this project. I am also grateful to Ella Shatila for her assistance during sample preparation and experiments. Her support was crucial for managing the large quantity of samples and experiments during this project.

I am also thankful to Raymon Dekker for his help with sample fabrication and to Daniel Stiekema for his help with manufacturing the test setup. Thanks also go to Sean Scott for his input and support with 3D printing facilities. I would also like to acknowledge the assistance provided by technicians and student assistants at the microscopy and welding labs.

Last, but certainly not least, I would like to mention my friends and family. My lab-mates and friends have made work at the lab and life during my master's more exciting. And I am extremely fortunate to have a loving and caring family back in India. Through their constant support and encouragement, I was able to find the motivation to keep moving.

Aswin Suresh
MSc student

May 24, 2024
TU Delft, The Netherlands

Table of Contents

List of Figures

List of Tables

1. Introduction

Functionally graded materials (FGM) can offer varying properties on a single structure. The term “functionally graded materials” was introduced in Japan in the 1980s, during the development of thermal barrier coatings [1], [2]. Some of the conventional manufacturing techniques for FGMs are chemical vapour deposition (CVD), centrifugal casting, and powder metallurgy (PM) [2], [3]. Although these techniques can manufacture FGMs ranging from thin film to large structures, they are accompanied by some trade-offs. For example, CVD is a high-energy intensity process and can produce harmful by-products, centrifugal casting is limited to radial gradients, and PM almost always contains pores that will degrade the thermal, mechanical, and corrosion properties [2], [3]. Considering the limitations of conventional techniques, additive manufacturing (AM) techniques have the potential for the production of FGMs and have gained increased attention in recent years [2], [3], [4], [5], [6].

AM of metals has slowly evolved from rapid prototyping to rapid manufacturing, now capable of replacing conventional manufacturing techniques [7]. AM builds a part layer-by-layer thereby reducing the amount of material wastage in addition to reducing the lead time and allowing greater flexibility in design complexity. As one of the main advances in the fourth industrial revolution, AM has found application in fields varying from aerospace and automobile to biomedical and architecture [8]. A variety of AM techniques are available for metals and a selection is made based on the application requirement. Wire arc additive manufacturing (WAAM) is a promising method for FGMs of large structures compared to other AM methods [9].

WAAM utilizes conventional welding processes such as gas metal arc welding (GMAW) or gas tungsten arc welding (GTAW), in combination with a robotic system. This provides a high degree of geometric freedom. WAAM has a high build-up rate and a variety of materials can be used as it utilizes conventionally used welding wires [10]. Recently, WAAM was used to manufacture ship propellers (Ramlab) [11], Pelton turbine blades (Hydroworld) [12], and organic-looking bridges [13]; these structures would be difficult to construct with conventional techniques. WAAM can also be used for modification or repurposing existing parts [13]. For structural applications of WAAM, stainless steels and mild steels received more focus than high-strength low alloy (HSLA) steels. However, there is a rising interest in HSLA steels especially for offshore wind energy due to the high strength-to-weight ratio compared to low-carbon steels [10], [14], [15].

HSLA steel components face two main challenges in marine environments: corrosion and ductile to brittle transition [16], [17]. HSLA steels are highly susceptible to stress corrosion cracking (SCC). Additionally, under arctic conditions below ductile to brittle transition temperature, the mechanical properties of HSLA steels are seen to deteriorate [16]. This is a hindrance to the application of HSLA steel components in marine environments. A solution may be to clad the HSLA steel with a corrosion-resistant material [18], [19]. Austenitic stainless (AUS) steels are corrosion-resistant and lack ductile to brittle transition temperature. WAAM can manufacture large FGM made of HSLA steel core and AUS steel cladding. Such a structure can also be utilised in the aerospace and energy industry [20].

However, bi-metal structures bring with them some challenges associated with the difference in phases. The joining of dissimilar metals creates a complex non-homogeneous interface that may have different mechanical properties from the individual materials. During the solidification process in welding, a variety of interplay takes place near the interface [21], [22]. One of the key features seen at the interface is the Type II boundary which is a preferential site for cracking [23]. In addition to these, properties like coefficient of thermal expansion (CTE) and thermal conductivity affect the cooling rate, which influences the microstructure. The current state of the art covers the microstructure, tensile properties and microhardness of such a FGM. However, the fatigue properties have not been investigated. This is necessary for reliable application. Though the theory of fracture mechanics associated with a non-homogeneous medium is complicated there are analytical, numerical, and finite elemental models that can be used for approximations [24], [25], [26], [27]. In this study, WAAM was used to build a FGM made of ER70S-6 (HSLA steel) and ER316L (AUS steel), and the fatigue crack growth behaviour at the interface region was studied.

2. State of the Art

2.1. Functionally Graded Materials

Functional Grading

Modern industrial development has brought with it the idea of structures with graded properties, which surpasses the constraints posed by homogeneous materials. A structure with graded properties is called functionally graded material (FGM) or functionally graded structure (FGS). Functional grading is applicable in various fields for numerous applications. Early examples of graded structures can be traced back to Japanese steel swords which have a graded transition from soft and tough core to hardened edge [28]. Other examples include carburising and nitriding treatment of steel gear teeth to impart hardness, fatigue resistance and wear resistance on its surface [28]. In the 1980s and 1990s, the primary focus of the application of graded structures was to control the thermal stresses when a component is exposed to high temperatures [2], [28], [29], [30], [31], [32], [33]. These graded structures were mainly applied in aerospace applications, solid-oxide fuel cells, and energy conversion systems using thermionic and thermoelectric materials. Over time, research has focussed on functional grading for lower-temperature applications as well. This research direction was motivated by a growing need to develop damage-resistant surfaces [28], [32]. Some examples include barrier coatings for structural components, articulating surfaces in hip and knee prostheses, and penetration-resistant materials for armour plates [28]. Researchers have also focused on functional grading to fabricate corrosion-resistant coatings. Examples include marine risers coated with corrosion-resistant material [19], a corrosion protection layer on Ti base [32], and cladding of ferritic steels with austenitic steels [18]. As FGM is a concept with a broad range of applications, it is necessary to narrow down the path of interest for the simplification of this study.

The motivation of this study is to understand additively manufactured metallic functionally graded structures. As a growing technology with immense capacity, additive manufacturing (AM) may have the potential to provide a feasible path for the fabrication of FGM. However, the AM of FGMs is still to be understood fully as the properties may vary with different material compositions and different AM techniques.

AM of FGMs

AM is capable of achieving gradients of different microstructural features by varying the process parameters. The different gradients of microstructure in FGMs can be classified as – structural gradients and chemical gradients [33], as seen in Figure 2.1. Examples of structural gradients include changes in grain size, twin thickness, lamellar thickness, porosities, and a combination of any of these. Change in these parameters may result in a change in mechanical properties such as ductility, fatigue resistance, and strength. A structural gradient can provide a combination of these properties on the same structure. Such accurate control of microstructures is possible through AM techniques with laser or electron beam. Ghorbanpour et al. [34] manufactured IN718 using selective laser melting (SLM) under different laser parameters. The structural gradient in this example is in the form of changing grain size. Higher laser power was reported to have larger grain size and elongation. Fogliatto et al. [35] investigated the influence of parameters of laser-based printing on porosities. They obtained a gradient structure having varying porosities. The main application for this FGM is for biomedical implants. Laser-based AM techniques are useful for smaller structures. For larger structures, WAAM is more suitable due to higher deposition rates [13]. However, WAAM has lesser resolution compared to laser baser techniques which could make it difficult to obtain complicated structural gradients.

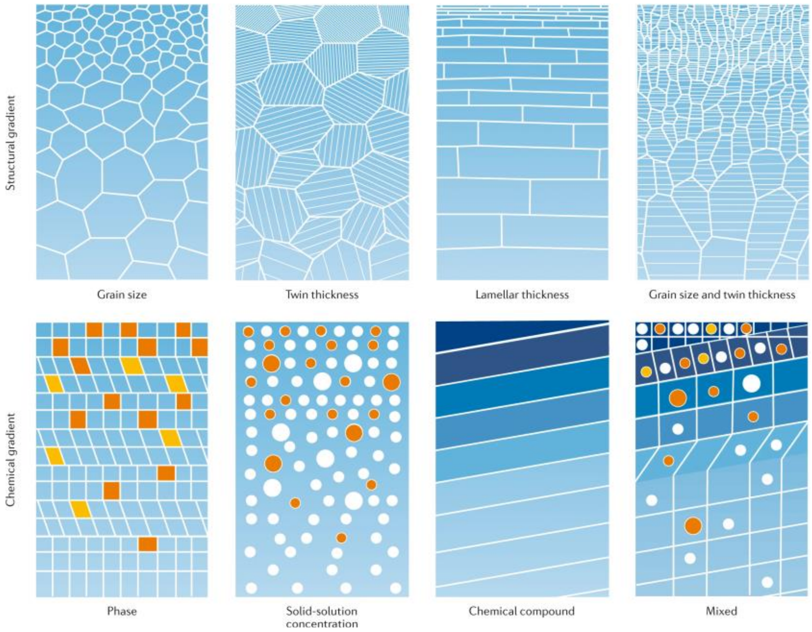

Figure 2.1 Structural and chemical gradients [33].

Structural gradients can also be present in combination with gradients in composition or chemical gradients. Some examples of chemical gradients are the distribution of phases, chemical components, and solid solution concentration. A gradient in the chemical composition will enable a gradient in properties associated with chemical bonding. These properties are relevant for functionalities such as load bearing, impact resistance, and non-mechanical applications. Most applications for chemical gradients are for biological applications [33]. In the case of metals, an example would be ferritic-austenitic steel dissimilar joint [9], [19]. Ayan et al. fabricated an FGM of ER70S-6 and 308LSi using WAAM. These two steels have different compositions and mechanical properties. From their research, Ayan et al. concluded that FGM structures with strong mechanical properties can be obtained through WAAM.

2.2. WAAM of FGMs

Wire Arc Additive Manufacturing

Wire arc additive manufacturing (WAAM) is one of several AM techniques for the production of metal structures. An electric arc in combination with a wire as deposition material is utilized in WAAM. It involves smaller cooling rates and higher heat input, which is beneficial for most commercially available materials. In WAAM, larger structures with higher deposition rates can be produced, when compared to other AM techniques [13].

WAAM can be classified based on the type of heat energy source [36], namely, Gas Metal Arc Welding (GMAW)-based, Gas Tungsten Arc Welding (GTAW)-based, and Plasma Arc Welding (PAW)-based. These WAAM processes have different deposition rates and time consumed for each material, based on which a selection is made for a particular application. In GMAW, heat is produced by an electric arc, being struck between the feedstock electrode (+ve terminal of the power supply) and the substrate (–ve terminal of the power supply). The electrode is shielded by an outwardly supplied shielding gas, which is an inert gas. GMAW-based WAAM has a higher deposition rate, better material utilization, low manufacturing cost, and environment-friendliness compared to the electron beam-based, laser beam-based, GTAW-based, and PAW-based AM technologies [13], [36], [37].

Manufacturing FGMs with WAAM may involve the melting of dissimilar metals. However, the melting of two metals together often does not result in a continuous structure with favourable properties. Alloys are designed by careful tailoring of element proportions and thermomechanical processing conditions to obtain consistent microstructural features with favourable properties. Even a small change in the composition and thermal history will result in a deviation of the properties of the alloy in terms of ductility, strength, and corrosion resistance. The creation of dissimilar joints often influences the composition and thermal history. Therefore, obtaining good metallurgical bonding between dissimilar alloys is a challenging task [6].

Dissimilar Joints with WAAM

A successful dissimilar joint will be as strong as the weaker alloy, given that the joint at the fusion line between both materials is of at least similar strength as the material with lower strength. However, the strength is also dependent on the gradient of the joint. An issue with dissimilar joints is the formation of sharp interfaces which create steep gradients. The steep property gradients will be prone to residual stresses which can lead to premature failures that are unknown in either of the base metals. Moreover, abrupt changes in the composition will also result in increased chemical potential gradients, which can drive alloying elements from one side to the other, where they could worsen the failure mechanisms [6]. The issues are different for different metal combinations.

Table 2.1 shows the cross-compatibility of different metals and the issues associated with joining them. The issues can be broadly divided into intermetallic formation and solubility limitations, thermal property mismatch, and other metallurgical effects. It may be noted that the biggest issue associated with dissimilar metal joints is melting temperature mismatch. For example, aluminium, magnesium, and copper have this issue when joining with most other metals. There are other problems present even when the melting temperatures are compatible. For example, in the ferritic-austenitic steel pair, the main issues are incompatibility in the coefficient of thermal expansion, martensite formation, and sensitisation due to carbon migration. Intermetallic formation is present almost always for titanium, nickel, zirconium, and aluminium.

Table 2.1 Alloy compatibility chart, showing a cross-comparison of various classes of engineering alloys and the major issues associated with joining them [6].

	AUS steel	**Martensitic and precipitation hardened SS**	**Low alloy steel**	**Ni**	**Al**	**Co**	**Cu**	**Mg**	**Zr**	**Refractory metals**
Titanium	IM, TM, CTE	IM, TM	IM, TM	IM, TM	IM, TM, CTE	IM, CTE*	TM, CTE	PS, TM, CTE, TC	None *	TM, TC
AUS steel	–	CTE	CTE, M, CM, S	IM, CM, S	IM, TM, CTE, TC	None*	PS, CTE, TC, TM	PS, TM, CTE	IM, CTE	IM, TM, CTE
Martensitic and precipitation hardened SS	–	–	CM, OM	None	IM, TM, CTE, TC	None*	PS, TC, TM	PS, TM, CTE*	IM*	IM, TM, CTE
Low alloy steel	–	–	–	M, CP, S	IM, TM, CTE, TC	None*	PS, TC, TM	PS, TM, CTE	IM*	IM, TM, CTE
Ni	–	–	–	–	IM, TM, CTE, TC*	None	TC, TM	TM, CTE*	IM*	IM, TM, CTE
Al	–	–	–	–	–	IM, TM, CTE*	IM, TM	IM	IM, TM, CTE*	IM, TM, CTE
Co	–	–	–	–	–	–	PS, TC*	TM, CTE*	IM, CTE*	IM, TM, CTE*
Cu	–	–	–	–	–	–	–	IM, TM, CTE, TC	IM, TM, CTE, TC*	PS, TM, CTE
Mg	–	–	–	–	–	–	–	–	PS, TM, CTE*	PS, TM, CTE*
Zr	–	–	–	–	–	–	–	–	–	IM*
Refractory metals	–	–	–	–	–	–	–	–	–	–
Intermetallic formation & solubility limitations IM - brittle intermetallic formation PS - poor solubility		Thermal property mismatch TM - melting temperature mismatch CTE - coefficient of thermal expansion mismatch TC - thermal conductivity mismatch		Other metallurgical effects CM - carbon migration OM - other species migration CP - carbide precipitation S - sensitisation M - martensite formation		None - no known issues *Limited data available				

It can be seen that dissimilar metal joint poses several challenges. These challenges need to be considered when choosing the materials for fabricating FGMs. The chosen materials should be soluble with each other. They should have similar thermal properties. It is also necessary to choose the right technique for fabrication. Some of these problems may be solved by controlling the heat input during the fabrication [6]. WAAM can accommodate a variety of heat inputs by controlling the printing parameters. However, when multiple layers are fabricated during WAAM, heat dissipation and thermal cycles also play a significant role in controlling the print quality. Using robotic systems, the path of printing can be kept under control. The deposition can be controlled by using the right metal transfer mode. For dissimilar metals Cold metal transfer (CMT) may be the ideal metal transfer mode. CMT provides low heat input with low spatter and the arc deposition mechanism. However, the complicated current waveforms and feeding of the wire make it challenging to understand the effects of welding parameters. Nevertheless, it may be the optimum choice for fabricating FGMs.

Design and Parameter Control in WAAM

Although welding has existed for many years, WAAM was made possible through the developments in robotics, control systems and computer-aided design (CAD). Most of the advancements are highlighted in Figure 2.2. CAD makes the design process more flexible. It allows the simulation of a design before it is fabricated. It also provides an opportunity for iterations with quick modifications. When integrated with a robotic system, the designs illustrated in a computer can be realised. Moreover, the imaging technologies which are part of the robotic system can monitor and provide feedback, thereby automatically controlling the process. An example of these imaging technologies is the laser scanner system, which can identify the surface of the part as it is being produced and provide feedback on the measurement of the part. Another example is the IR pyrometer, which can monitor the temperature at the surface, allowing time for the part to cool before depositing the subsequent layer. These systems can keep the process in check and maintain the accuracy [37], [38].

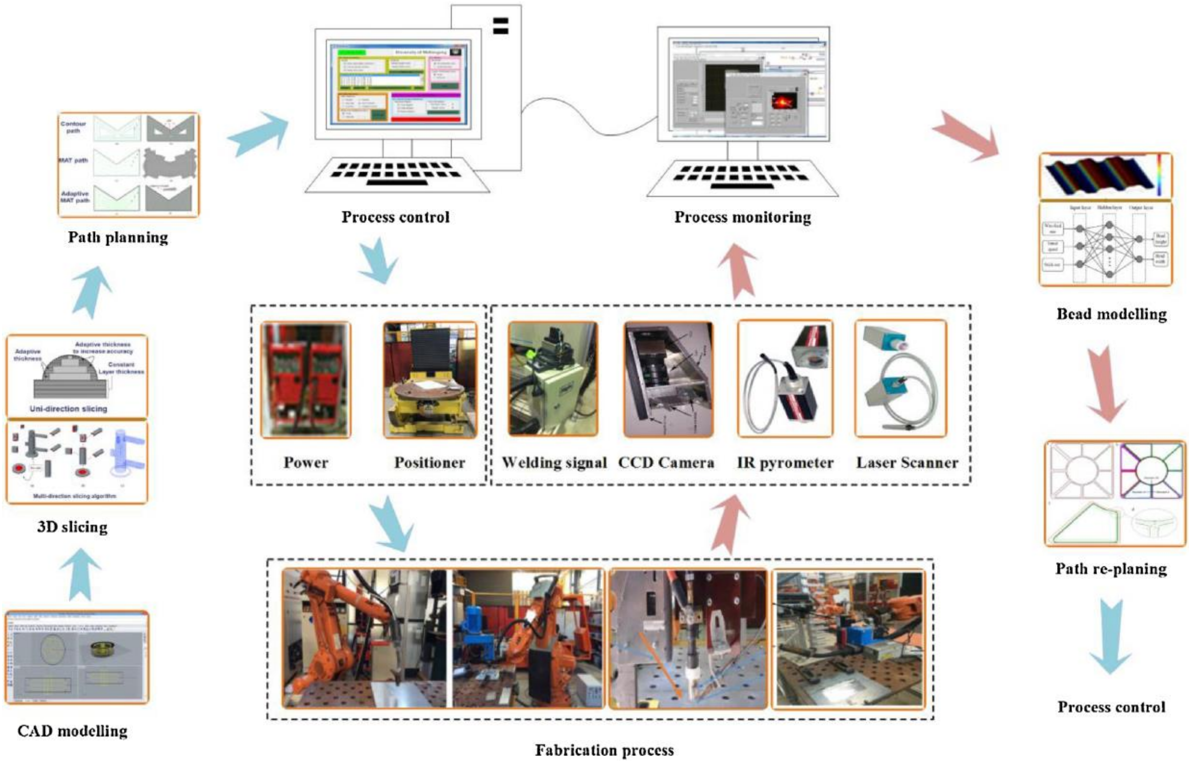

Figure 2.2 WAAM system design concepts [37].

Robotic systems can provide better control over the parameters. They can move with much higher precision than humans. The process parameters that are of primary concern for WAAM, are voltage, nominal current, wire feed rate (WFR), and travel speed (TS). These parameters affect the heat input, which affects the weld characteristics and the quality of the deposited structure [36]. A robotic system can have co-ordinated movement with desired TS, while simultaneously controlling the WFR, voltage, and nominal current. It may then be possible to systematically control the heat input.

Heat input affects the microstructure as well as the bead geometry. An excessive heat input results in the re-melting of previously deposited layers, which may deteriorate the macrostructure of the part. In contrast, a lower heat input enables uniform deposition on the surface without any overflowing or collapsing. Moreover, lower heat input is beneficial to reduce porosity in the part as the solubility of gas reduces with lower droplet temperature. However, with low heat input, the melt pool may not have sufficient time to spread before solidification. Higher heat input reduces the viscosity of the melt pool and allows it to spread evenly. Higher heat input is associated with higher WFR and TS, which also enables higher deposition rates. Hence the main question in WAAM is to find a balance between heat input and deposition rate [36].

Arc current and voltage also influence the quality of the part. Arc current affects the roughness of the beads, electrode burn-off rate, depth of fusion, and weld geometry. Higher arc current results in increased weld penetration, which results in stronger welds. Arc voltage also controls the weld penetration. Higher arc voltage results in wider, flatter, and shallow penetration depths [36]. Controlling the parameters is crucial to control the properties and to avoid any defects. In the next section, the common defects observed in WAAM will be discussed.

Defects in WAAM Products

Controlling the process parameters and choosing the right metal transfer mode is necessary to avoid defects. Many defects can be present in wire arc additive manufactured (WAAMed) parts, most of which are highlighted in Figure 2.3. Defects in WAAM can be caused due to various reasons such as poor programming strategies, unstable weld pool dynamics due to poor parameter setup, thermal deformation associated with heat accumulation, environmental influence (such as gas contamination) and other machine malfunctions. The defects may be more prominent in some materials compared to others.

Several researchers have studied the formation of defects in WAAMed materials. Wu et al. [37] reviewed the defects observed in numerous WAAM processed materials. The common defects reported are residual stress, crack, delamination, poor surface finish, deformation, porosity, oxidation, and rough surface. These are correlated with different materials in Figure 2.3. Though it is a good overview of common defects in WAAM, the attention given to steel is less compared to other materials. It might be more sensible to focus attention of this discussion on defects that are expected in HSLA and AUS steels. Zhang et al. [39] compared the microstructure of HSLA steels manufactured by WAAM and conventional casting. They observed several pores and investigated the influence of parameters on the pores. Long et al. [40] studied the microstructural evolution of WAAMed AUS steel and the effects of processing parameters. They observed cracks and pores as the main defects. For this section, the attention will be given on the formation of cracks and pores with focus on HSLA and AUS steels.

One of the main causes of crack formation is residual stress. Residual stress is inherent to all metal AM processes, including WAAM. It is the stress that remains in the material when all the external load is removed. Residual stress is caused by the solidification and shrinkage of the deposited layers due to repeated heating and cooling during the AM process. The more layers that are deposited, the higher will be the build-up of residual stress. Residual stress can lead to distortion of the part, loss of geometric tolerance, delamination of layers during deposition, as well as deterioration of fatigue performance and fracture resistance of the AM parts. If the residual stress is higher than yield stress but lower than the ultimate tensile strength, warping may occur. If the residual stress is higher than the ultimate tensile strength or fracture toughness of the material, cracks will start forming [36], [37].

Apart from residual stresses due to thermal signatures of the AM process, material characteristics also play a role in crack formation. These cracks can be either solidification cracks or grain boundary cracks. Solidification cracks depend mainly on the solidification nature of the material. It is usually caused by the obstruction of solidified grain flow or high strain in the melt pool. Grain boundary cracking is generated along the grain boundaries due to the differences between boundary morphology and potential precipitate formation [37].

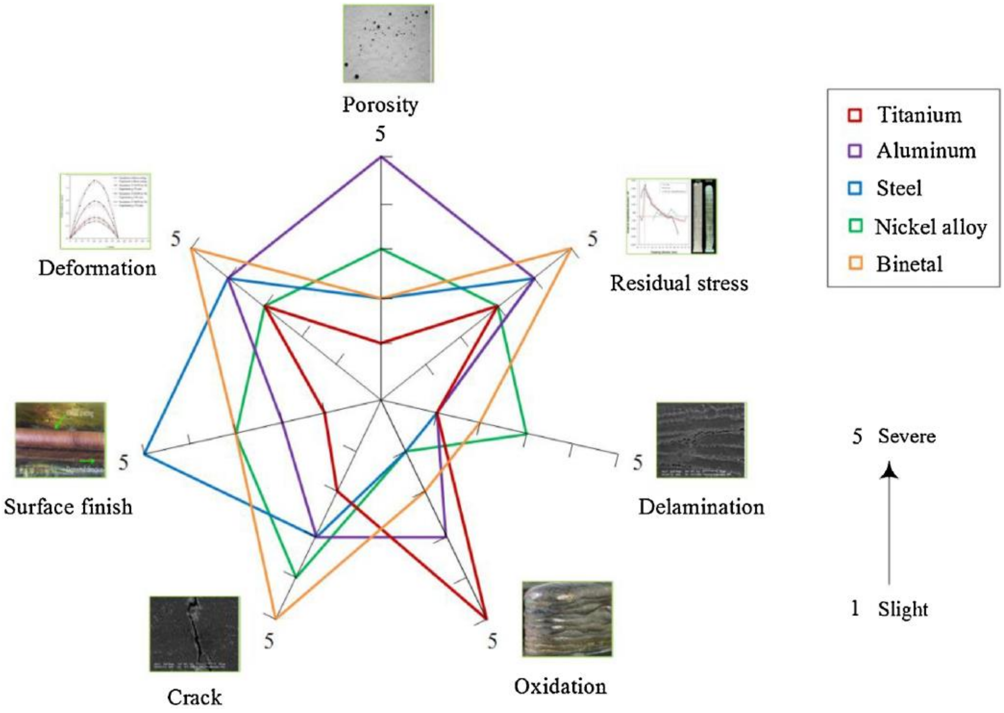

Figure 2.3 The correlation between materials and defects in WAAM processes [37].

Porosities may be caused by the contaminations present in the feed material. Contaminations such as moisture, grease, and other hydrocarbon compounds may be easily absorbed into the melt pool and subsequently generate pores during solidification. Porosity may also be caused by the process involved. These are non-spherical pores caused by poor path planning or unstable deposition processes. A complex deposition path may cause insufficient fusion or spatter, creating gaps or voids. Porosities will have adverse effects on the mechanical properties of a material. The strength of the material will be lowered, and the fatigue properties will be reduced due to the presence of micro-cracks [37].

Zhang et al. [39] correlated the heat input pore formation in HSLA steel. Higher heat input resulted in higher pore formation due to increased solubility of gases. This is related to lower WFS and TS. At higher WFS and TS the material has higher cooling rate. This prevents gases from escaping and cause pores. Long et al. [40] also found that lower heat input prevented the gases from escaping in AUS steel. The tensile testing of AUS steels showed coalescence of pores resulting in crack formation. It may be possible for these cracks to form through residual stresses.

Opportunities and Scope with WAAM

The choice of materials and processes that are studied stems from either a form of exploration or from the influence of immense demand from the industry. Functionally graded materials have immense potential to withhold tailored properties on each part of the structure based on the application. However, joining of dissimilar metals is accompanied with numerous challenges due to property mismatch. Choosing the right material and technique then becomes a crucial aspect for a study. Though there are several techniques available for FGM, WAAM is selected for reasons including high deposition rate, high degree of freedom, and available selection of materials [10].

From an industrial perspective, there is a rising interest in high-strength low alloy (HSLA) steels for structural applications, especially for offshore wind energy [10], [14], [15]. HSLA steels have a higher strength-to-weight ratio compared to low-carbon steels. Replacing low-carbon steels with HSLA steels may thus prove to be economical. However, HSLA is prone to corrosion under marine conditions. Moreover, it is susceptible to failure under low temperatures due to ductile to brittle transition. A solution to this problem is to form a cladding on the HSLA steel structure with austenitic stainless (AUS) steel. This is an example of functional grading, which will be considered for this study.

Many studies have been conducted on the application of WAAM for producing FGMs of steels [9], [19]. Chandrasekaran et al. [19] highlighted the application of WAAMed FGMs for marine risers. They implemented CMT-based WAAM to fabricate an FGM with C-Mn steel and duplex stainless steel. They noted the diffusion of elements at the interface which led to different properties at the interface. They also found that the interface formed due to coalescence of elements resulted in improved mechanical strength. The interface formed in an FGM is thus a heterogeneous material formed through complex solidification phenomena dependent on the composition and properties of the individual materials that are being joined. Therefore, studying the interface is one of the most critical aspects when implementing an FGM.

2.3. HSLA Steels and AUS Steels

High Strength Low Alloy Steels

HSLA steels are a class of steels that evolved from plain carbon or mild steels. Several research developments in the 1950s and 1960s resulted in the present-day HSLA steels. These advances provided an understanding of the interactions between different microalloying elements and process variables such as grain refinement, strength, and ductility. The microstructure of HSLA steels is similar to plain carbon steels, with smaller ferrite grains due to the presence of microalloying elements. HSLA steels contain about

0.15% C, 1.0% Mn, 0.6% Si, and 0.1% of other microalloying elements. The high strength is provided by grain refinement, substitutional strengthening by Mn and Si, and precipitation strengthening by micro-alloy precipitates [41].

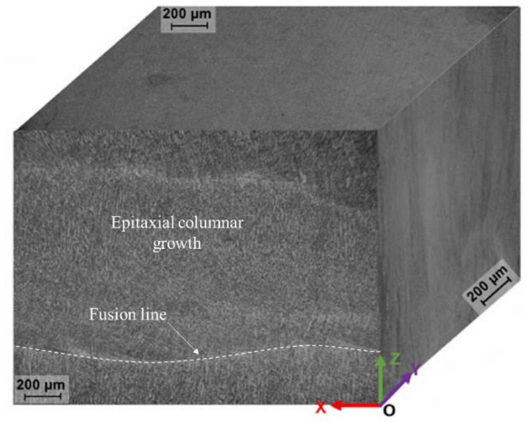

Figure 2.4 Three-dimensional macroscopic characteristic of a thin-wall WAAMed ER120S-G. The fusion line and the epitaxial growth are highlighted [39].

The microstructural features in WAAMed HSLA steel are different from when manufacturing with conventional techniques. Zhang et al. [39] compared microstructural characteristics of HSLA steel manufactured with CMT-based WAAM and casting. The welding consumable used for WAAM was ER120S-G. Casting of steel with similar composition was done using customized vacuum induction melting furnace. The macrostructure of WAAMed material exhibited epitaxial columnar growth morphology as shown in Figure 2.4. In Figure 2.5 the phases present in WAAMed and as-cast material are shown. The majority of the phase present in WAAMed material was α-Fe in the form of bainitic ferrite. However, γ-Fe in the form of austenite were also detected with volume fraction of around 5%. This was absent in cast material. The reason was attributed to the difference in the cooling rates. The cast material had the main constituent of BCC α-Fe. Near-cellular segregations were observed surrounding granular bainite as shown in Figure 2.6(a). The segregations were enriched in C, Ni, Mn, and Cr. The segregations in WAAMed material were in the form of bands as seen in Figure 2.6(b). Rodrigues et al. [42] studied WAAMed ER110S-G. They observed acicular morphologies of bainitic ferrite and absence of pearlite and polygonal ferrite. This was attributed to high cooling rates. They also reported 12% volume fraction of retained austenite. In another study, Rodrigues et al. [43] compared the effects of different heat inputs for WAAMed ER110S-G. In all cases ferrite, bainite and martensite-austenite (M-A) constituents were observed. These different morphologies of WAAMed HSLA steel parts may also result in different properties from conventional processes.

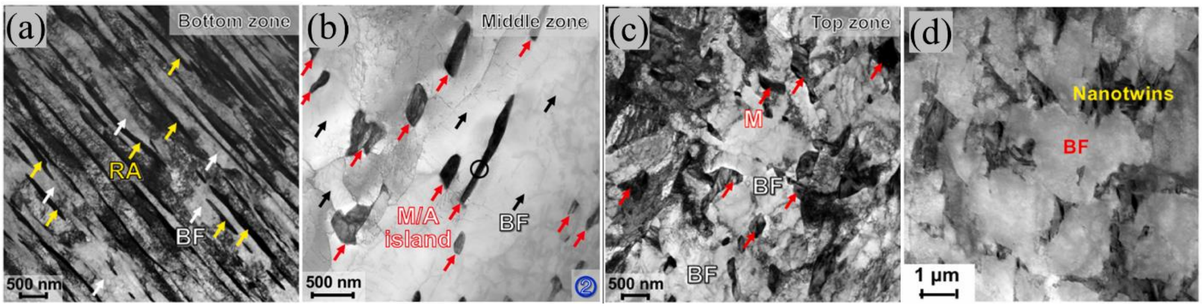

Figure 2.5 TEM bright-field images of WAAMed ER120S-G and conventionally cast steel with similar composition. (a) Bottom zone, (b) middle zone, and (c) top zone of the print. (d) As cast steel. RA – retained austenite, BF – bainitic ferrite, M/A – Martensite austenite, and M – martensite [39].

HSLA steel has good mechanical properties. It has a favorable strength-to-weight ratio when compared with low carbon steels. HSLA steels have a typical strength of 350 to 700 MPa, ultimate tensile strength of 450 to 850 MPa, and an elongation of 14% to 27%. For WAAMed HSLA steels, Rodrigues et al. [42] reported a yield strength of 707±33 MPa, ultimate tensile strength of 889±16 MPa, and elongation of 30±2.8%. These values are different along build direction and other directions, indicating anisotropy. The high strength of HSLA steels, however, is only high in comparison to plain carbon steel. Quenched and tempered high-carbon steels may have strengths of up to 1100 MPa with the loss of fracture toughness, fatigue resistance, weldability, and formability. Often certain properties are enhanced at the expense of others. For HSLA steels the trade-off comes in the form of lack of formability and ductility [41].

Herein comes one of the benefits associated with WAAM of HSLA steels. Since WAAM can create geometrically complex shapes without requiring formability, HSLA steels may be used in WAAM. Moreover, HSLA steels exhibit good weldability and is thus suitable to be used in WAAM. Research on WAAM of HSLA has focused on two aspects, namely, the development of different welding wires for different strength levels and the optimization of process parameters for manufacturing [44]. The different welding wires are ER70S-6, ER80, ER100, ER110S-G and ER120S-G. Researchers have studied WAAMed parts with these wires and have indicated a potential for them to replace conventional manufacturing. The process parameters for WAAM, which were discussed in the previous chapter, were also studied by researchers.

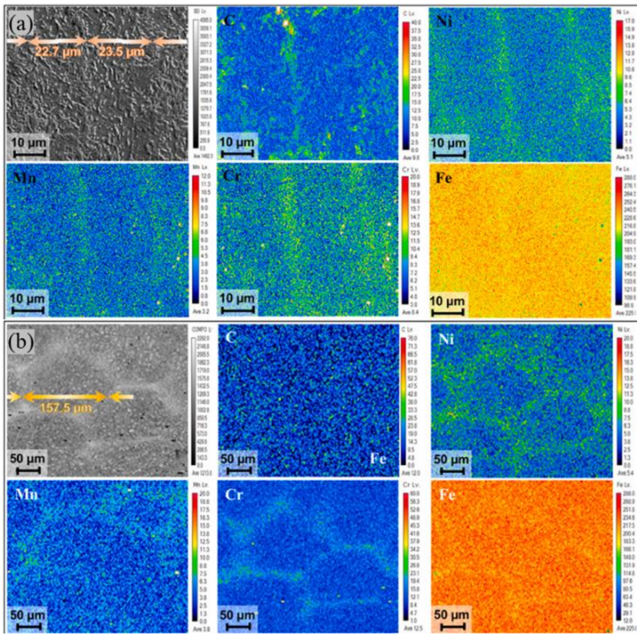

Figure 2.6 Electron probe micro-analyser characterizations exhibiting the element distribution mappings of (a) WAAMed ER120S-G and (b) as-cast steel of similar composition [39].

Some conclusions have been made by researchers concerning heat input and properties of the WAAMed part. Yildiz et al. [45] conducted a study on HSLA fabricated by WAAM with different WFS and TS parameters. The WFS/TS ratio is an indication of heat input. They found a linear relationship between bead dimensions and the heat input. Additionally, an inversely proportional relation was found between heat input and microhardness. They also found that the tensile properties remain uniform with testing directions. However, they did observe differences in elongation with testing direction.

Similar results were obtained by a study conducted by Rodrigues et al. [43] which aimed at determining the effects of thermal cycles during WAAM with ER110S-G. In their experiment, two walls with two different heat inputs were made. It was reported that the different heat inputs caused no significant microstructural changes and the presence of ferritic bainite, and M-A constituents were observed in both. A variation in hardness was seen along the build direction which is attributed to the cooling rate and the change in grain size. The micrographs along the build direction are shown in Figure 2.7.

The microstructural evolution of HSLA steels during WAAM is mainly a product of heat flow. As mentioned earlier, grain size and hardness were dependent on the heat input. However, in WAAM the residual heat of the previous layer also plays a role. The portion near to substrate cools faster. The portion away from the substrate accumulates heat from previous layers which affects the cooling rate. Yildiz et al. reported high amounts of martensite near the substrate [45]. Lesser amounts of martensite were reported away from the substrate. Rodrigues et al. reported increasing grain size along the build direction [43]. Moreover, acicular ferrite and bainite were also reported.

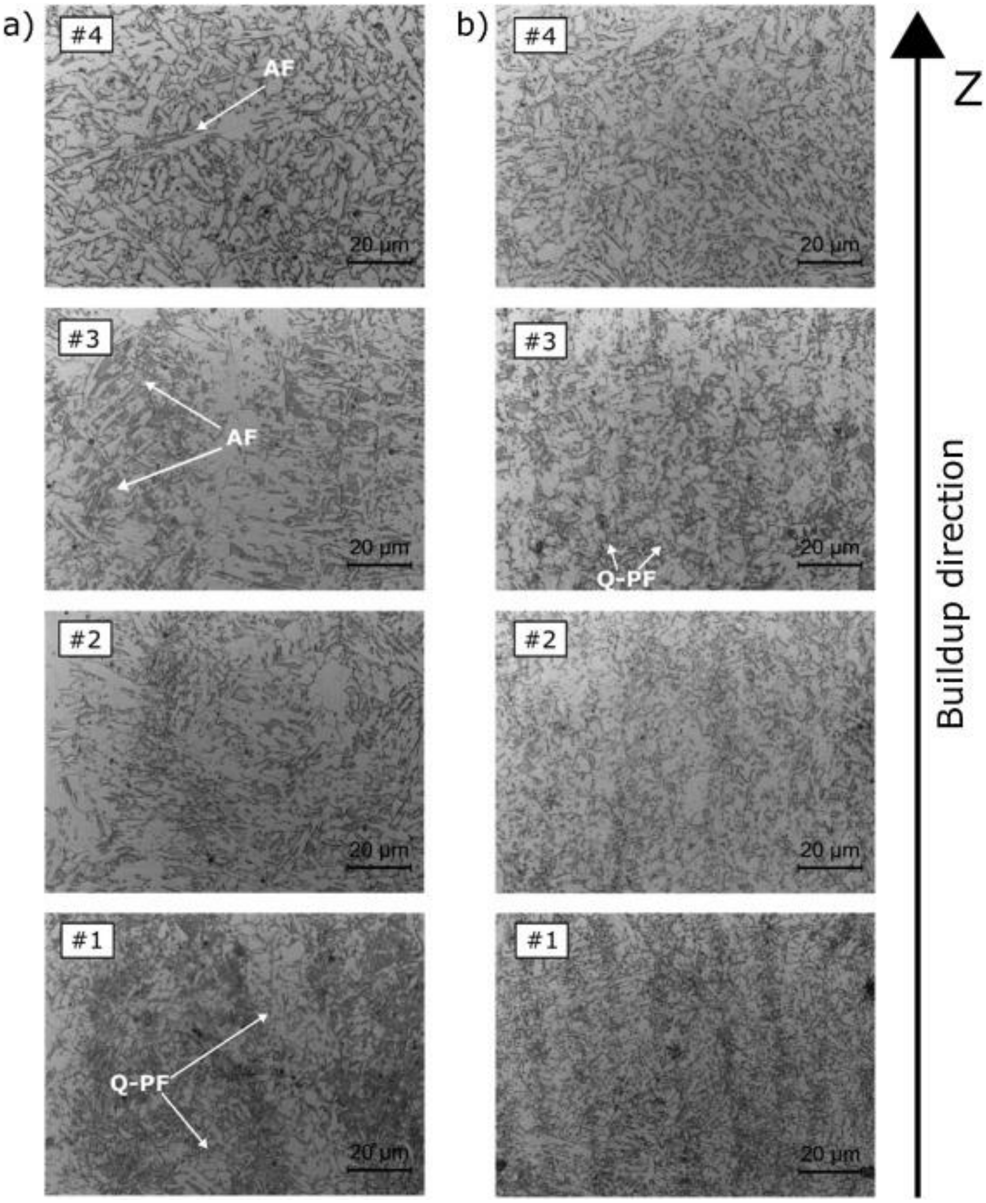

Figure 2.7 Cross-section micrographs of WAAMed ER110S-G: a) High heat input sample and b) Low heat input sample, along the height (AF: acicular ferrite; Q-PF: quasi-polygonal ferrite) [43].

The microstructure morphologies which are a consequence of heat flow may be explained with the solid-state transformation mechanisms. In HSLA steels, the solid-state transformations are in the regimes 1300 to 800 °C and 800 to 500 °C. The austenite that is formed during the first regime is transformed into ferrite morphologies in the second regime. During cooling, allotriomorphic ferrite forms at the prior austenite grain boundaries (PAGBs). This is followed by side-plate ferrite nucleation at austenite/ferrite boundaries and extends to untransformed austenite grains. Since the carbon content in HSLA steel wire feedstock is less than 0.2%, the impingement of allotriomorphs across austenite grains minimizes the possible growth of Widmanstatten ferrite. Hence, acicular ferrite is formed from the retained austenite with further cooling. Bainitic ferrite may form upon further cooling in the absence of potent inclusions and the remaining austenite may be enriched in carbon. Depending on the carbon content of the remaining austenite, the final cooling to room temperature may result in martensite or martensite-austenite

(M-A) [42], [43]. In WAAM, the cooling rate is faster than that required for formation of pearlite which explains its absence. If the cooling rate is increased drastically, formation of martensite can be promoted. An intermediate cooling rate may promote formation of bainite which could improve the mechanical properties.

A higher degree of microstructural control may be achieved as the WAAM technology develops with further research. This will provide tailored mechanical properties of WAAM products and conventional manufacturing may be replaced for certain applications. To control the mechanical properties of the as-built WAAM parts, researchers have investigated several deposition strategies. Several cooling strategies have also been investigated. This includes controlling the cooling rate of the deposited bead as well as maintaining the heat flow within the entire part. These strategies increase the efficiency of the manufacturing process and improve its potential for use in relevant engineering applications.

HSLA steels are used in several engineering sectors albeit facing some challenges. Currently, HSLA steels are used for structural applications in marine, engineering, and construction [44]. They are also widely used in oil pipelines and transport industries [46]. However, the corrosion of HSLA steels in seawater is of concern and has been studied extensively [17], [46], [47]. Cl^- ions in seawater cause pitting corrosion of carbon steels resulting in a reduction of the lifetime of the steel. For HSLA steels, the corrosion exacerbates stress corrosion cracking (SCC) failures [46]. Furthermore, HSLA is also susceptible to ductile to brittle transition at cryogenic temperatures [16], [48]. This may affect its utility in harsh environments such as arctic conditions. Cladding the structure with a resistant material may be a solution to these problems [18], as hinted in previous chapters. Stainless steels are suitable for forming cladding and thus an FGM with HSLA steels. Before a detailed discussion on this FGM pair, a brief discussion on stainless steel can be helpful.

Austenitic Stainless Steels

Stainless steels are a group of high-alloy steels based on the Fe–Cr, Fe–Cr–C, and Fe–Cr–Ni systems. The “stainless” nature of these steels is due to the presence of Cr above 10.5 wt%. The Cr forms a passive surface oxide and prevents further oxidation and corrosion under ambient, non-corrosive conditions. AUS steels are a type of stainless steels containing high austenite-stabilizing Ni as an alloying element. The addition of Ni above 8 wt% in the alloy makes the austenite phase stable at room temperature and below, thus forming AUS steel [49, Ch. 1]. AUS steels are corrosion resistant and not susceptible to ductile-to-brittle transition and thus are chosen for forming FGM with HSLA.

AUS steels have a typical strength of 230 to 260 MPa, an ultimate tensile strength of 600 to 800 MPa, and an elongation of 45% to 60% [50]. When concerning mechanical properties, the striking feature of AUS steels in comparison to HSLA is the ductility. Incidentally, AUS steels can be strengthened significantly by cold working. They are, however, not heat-treatable due to majority presence of austenite phase. AUS steels are generally considered to be weldable [49] and are a suitable material to be used in WAAM [51], [52].

Implementation of AUS steels in WAAM has been studied substantially in the literature. Most of the research is focused on tensile properties, fracture toughness, and microstructural development [53]. Laghi et al. [54] studied the tensile properties of 304L AUS steel produced by WAAM. They aimed to investigate the possible anisotropy in the product. For this, they conducted mechanical characterization along the transverse, longitudinal and diagonal directions with respect to the building direction. They reported the presence of anisotropy and indicated that the highest elastic and plastic properties were found along the diagonal direction. This anisotropy was related to the orientation of fine cellular sub-structures. Jing et al. [55] investigated the influence of heat input on strength and isotropy. Their works indicate that lower heat input results in fewer columnar grains and reduced anisotropy. This is related to the lower thermal gradient along the build direction, which prevents grain growth. This creates smaller and more equiaxed grains. Kumar et al. [56] studied the mechanism that controls the fracture toughness in stainless steel 316L manufactured by SLM, WAAM and wrought process. The fracture toughness of SLM samples were high, whereas for WAAM and wrought samples it was comparable. However, for manufacturing larger structures, WAAM is more suitable than SLM. Additionally, it can be noted that WAAM can provide properties that are good enough in comparison to conventional methods.

Kumar et al. [56] also compared SLM, WAAM and wrought processed parts, for their microstructure before and after fracture toughness experiments. For WAAM, a significant amount of δ-ferrite with vermicular morphology was observed in the microstructure. They have reported that these morphologies appear in a disconnected manner indicating different cooling rates as a function of distance. A small colour gradient in the inverse pole figure (IPF) was reported for the WAAM sample, indicating dislocations generated in the grains as a result of the thermal gradient. Additionally, among the three processes that were compared, the WAAM sample exhibited the least ductility. The deformation mechanism in WAAM samples is due to slip and creation of geometrically necessary dislocations (GNDs) at the interface of austenite and δ-ferrite. Beyond a certain limit, these interfaces act as debonding points and initiate the crack. Though Kumar et al. focused on fracture toughness, the interface between austenite and δ-ferrite may also be a concern for fatigue failure.

Similar to HSLA steels, the observed AUS steel microstructures are also a consequence of the heat flow during cooling of the material. The top layers dissipate heat more slowly compared to the bottom layers. Due to this larger grains are observed in top layers [57], [58]. An example is shown in Figure 2.8. The grain growth is typically in the direction of printing, with an austenite matrix and ferritic dendrites [55], [57]. This discussion on the formation of phases may be supported by a brief look into the solidification mechanisms, as seen with the HSLA steels.

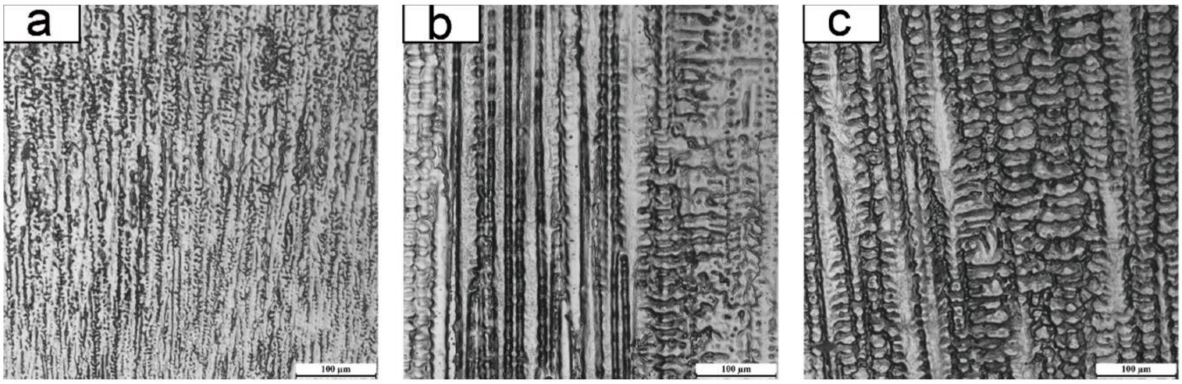

Figure 2.8 Microstructural photos of each region along the building direction of the as-deposited wall: (a) Bottom, (b) middle, and (c) top [58].

There are four solidification and solid-state transformations possible in AUS steel welds, namely, Type ‘A’, ‘AF’, ‘FA’, and ‘F’ [49, Ch. 6]. The former two have austenite as the primary phase, while the latter two have ferrite as the primary phase during the first stages of solidification. Type A has a fully austenitic, well-defined solidification structure. Type AF occurs when there are ferrite phases formed in the terminal phase of the solidification due to ferrite-promoting elements such as Cr and Mo. Type FA solidification has primarily a ferrite phase and austenite is formed at the end of the solidification. Type F has the complete formation of ferrite before transformation into acicular ferrite surrounded with austenite and Widmanstätten side plates. Type F is not common in AUS steel and is more characteristic of duplex steels. The type of solidification of AUS steel determines the amount and morphology of δ-ferrite in the austenite matrix. As discussed earlier, the interface between δ-ferrite and austenite can possibly act as debonding points.

During the solidification process, there will be the formation of single-phase interfaces within the AUS steel. The main types of single-phase interfaces in AUS steels are solidification subgrain boundaries (SSGB), solidification grain boundaries (SGB), and migrated grain boundaries (MGB). These interfaces may also be a primary source of defects associated with fusion zones. In addition to the single-phase interfaces, AUS steels may also be susceptible to defects through the formation of embrittling σ-phases [40], [49, p. 167]. These are formed by FeCr, which is hard and brittle. When present in a larger volume fraction, it can reduce ductility and toughness. Besides Cr, the addition of Mo, Nb, Si, W, V, Ti, and Zr may also promote the formation of σ-phases. Generally, retained ferrite increases the chances of formation of these phases. However, weld solidification cracks occur preferentially along SGBs. Under Type A solidification, these boundaries are very straight, contain no residual ferrite, and offer little resistance to crack propagation. In contrast, an SGB under type FA solidification contains a mixture of ferrite and austenite that complicates crack propagation.

Understanding the relation between microstructural development and WAAM parameters will aid in the prevention of defects. As hinted in the previous section, the purpose of the discussion on AUS steel here is to eventually discuss the implementation of stainless steel as cladding for HSLA steels. The main two purposes for cladding mentioned were the corrosion resistance in marine environments and the absence of ductile to brittle transition at lower temperatures. However, not all AUS steels are suitable for marine environments [49, p. 206]. Most of them are susceptible to SCC under Cl^-

environment. The marine-grade stainless steel 316L is suitable for such conditions [51]. The “L” in 316L indicates lower carbon content which helps in the prevention of SCC. Moreover, 316L or ER316L does not have a DBTT, and the mechanical properties do not deteriorate under lower temperature conditions. Thus, it may be possible to clad HSLA steels with AUS steels for applications in marine environments. Such a cladding results in the formation of an interface between ferritic and austenitic material. In the following section, the interface of ferritic steel and austenitic steel, representing the HSLA-AUS steel pair, will be discussed.

HSLA-AUS Steel Interface

In the sections and chapters so far, the discussions started with FGMs, followed by WAAM, and then finally HSLA steels and AUS steels. It is now possible to discuss the combination of these topics, which is, the FGM of HSLA steels and AUS steels produced by WAAM. This section will start the discussion with a general overview of FGM of ferritic and austenitic materials, which are the main phases constituting this material pair. Once a few studies have been briefed, the solidification phenomenon in a ferrite/austenite pair will be discussed. The section will conclude with some highlights on the main challenges faced by FGM of these pair and will provide some directions to explore this area of research.

There are several studies on dissimilar joints between ferritic and austenitic materials. These joints are often used in applications such as superheater tubes and vessel piping welds of nuclear energy generation facilities [59], [60]. Ferritic low-alloy steel provides good strength and AUS steels offer high-temperature strength, resistance to oxidation, and creep-rupture properties. Shin et al. [60] and Zuback et al. [59] have, however, expressed concerns over defects formed at the interface in dissimilar joints. Abrupt changes in chemical composition, microstructure, and physical properties may cause severe cracking, increasing the risk factor of such FGMs in nuclear facilities [57].

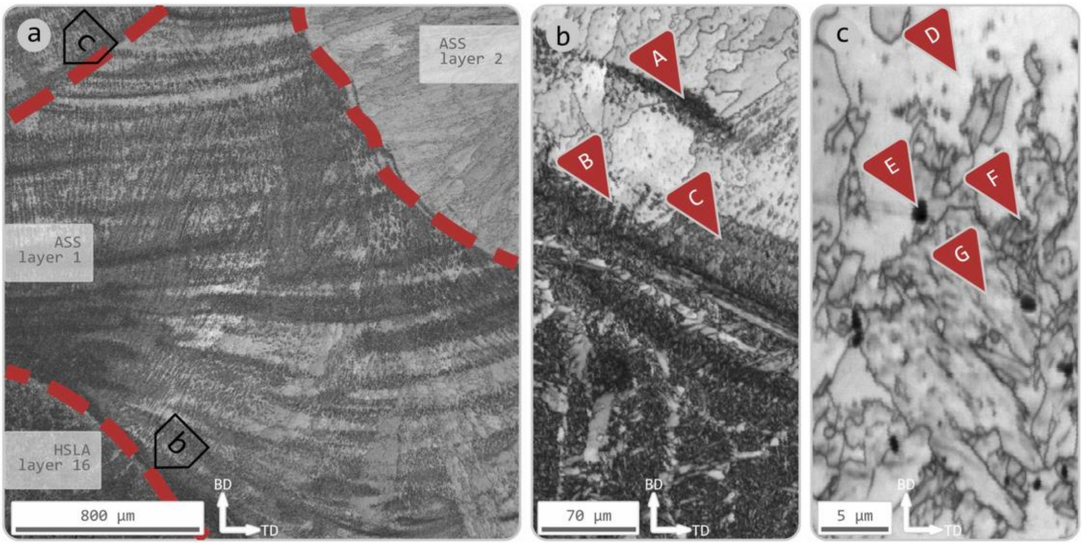

Figure 2.9 Microstructure at the interface region of functionally graded ER70S-6/ER316L manufactured by WAAM. (a) Low magnification EBSD Image Quality (IQ) map of ER70S-6 (layer 16) and ER316L (layer 1 and layer 2). (b) High magnification of the region around the dissimilar fusion boundary. (c) High magnification of bainitic / ferritic phase within the ER316L layer 1 and away from the dissimilar fusion boundary [20].

Zuback et al. reasoned the need for compositional gradients due to the carbon migration in dissimilar joints. A band of carbides forms at the austenite side of the interface, creating a carbon-depleted zone on the ferrite side. This depletion may lead to premature failures at the fusion line [56]. The carbon content of HSLA steels in their study and their references are similar to welding consumables such as ER70S-6. However, they have referred to DuPont et al. for reasoning of carbon diffusion. DuPont et al. [61] have discussed carbon diffusion for heat-treated dissimilar joints. They have not mentioned carbon diffusion after welding. Instead, a band of martensite was reported at the interface which led them to investigate with heat treatments. Galán Argumedo et al. [20] studied the microstructural characteristics of FGM of ER70S-6 and ER316L manufactured by WAAM. The microstructure at the interface of the two materials is shown in Figure 2.9. They also observed the presence of martensite (marker A) in the interface. Martensite was also observed at the fusion boundary (marker C), which corresponds to a type II boundary. Type II boundary is where grains from dissimilar material solidify parallel to the fusion line along the dissimilar boundary. In contrast, type I (marker B) boundaries are formed by grains solidifying perpendicular to the dissimilar boundary. Other microstructural features observed were austenite matrix (marker D), acicular ferrites (marker G), porosities (marker E), and lath packages (marker F). Yadav et al. [62] studied the functionally graded deposition of 316LSi and ER70S-6 fabricated through twin-WAAM. In their microstructural characterization, they note the increasing presence of bainite at the interface. They indicate that when the cooling rate is not sufficiently fast to form martensite and sufficient to prevent carbon migration and formation of pearlite, austenite is transformed into bainite. Hence, it is necessary to provide an ample amount of time for cooling when depositing the austenite material on the ferritic material. Thus, utilizing a ferritic material with low carbon content and providing sufficient cooling time during WAAM might prevent issues related to carbon migration.

There are also some other concerns over dissimilar joints. Shin et al. highlighted that dissimilar joints were susceptible to SCC. Additionally, some concerns regarding the difference in CTE were also indicated [60]. Nelson et al. [21], [22] reported the formation of type II boundary at the interface which may increase the chances of cracking. To understand these concerns further, a discussion on the solidification mechanism at the interface of the ferrite-austenite dissimilar joint may be helpful.

Nelson et al. [21], [22] conducted an extensive study on the microstructural evolution of the fusion boundary in ferritic-austenitic dissimilar weld metals. They used a high-purity iron substrate and welded with 70Ni-30Cu single-phase (FCC) as filler material using GTAW. While the solidification phenomena are dependent on the compositions and welding parameters, the study by Nelson et al. can serve as an example to get a basic understanding. They studied three parts of the welding region, namely, the fusion boundary (FB), the HAZ, and type II boundaries. Type II boundaries are formed by grains which are oriented parallel to the fusion line, which is contrary to the epitaxial nature of welds. They also investigated the three regions of cooling, namely, δ-ferrite temperature range, austenite (γ) temperature range, and α-ferrite temperature range.

The solidification phase at the fusion boundary involves the interaction between the different phases of ferritic and austenitic steels. Once the weld pool starts to cool, it enters the δ-ferrite temperature region. The initial solid forms through a heterogeneous nucleation event, due to the differences in composition, lattice parameter, and crystal structure between the substrate (BCC) and weld metal (FCC). The orientation of the newly formed grains aligns to the closest relationship with the partially melted substrate. As the weld and surrounding HAZ cool, the δ-γ interphase boundary in the HAZ approaches the fusion boundary. However, the δ-ferrite does not advance beyond the fusion boundary, as the weld metal is stable FCC [21], [22].

On further cooling, transformation from δ-ferrite to austenite takes please in both austenitic and ferritic material. Upon entering the austenite temperature range, the FB now becomes a metastable γ-FCC boundary (γ on the ferritic side and FCC on the austenitic side; this nomenclature may be useful for distinguishing austenite phase in ferritic and austenitic material). This forms a boundary of the same phase with different compositions. Furthermore, there is the presence of a steep thermal gradient and high strain energy at the FB, aided by lattice mismatch and difference in CTE. All of this contributes to residual stresses at FB. The γ-FCC boundary migrates into weld metal driven by the need to reduce free energy, thereby producing a type II boundary, as shown in Figure 2.10. One or any combination of these may also contribute to cracking-related issues in dissimilar welds [21], [22].

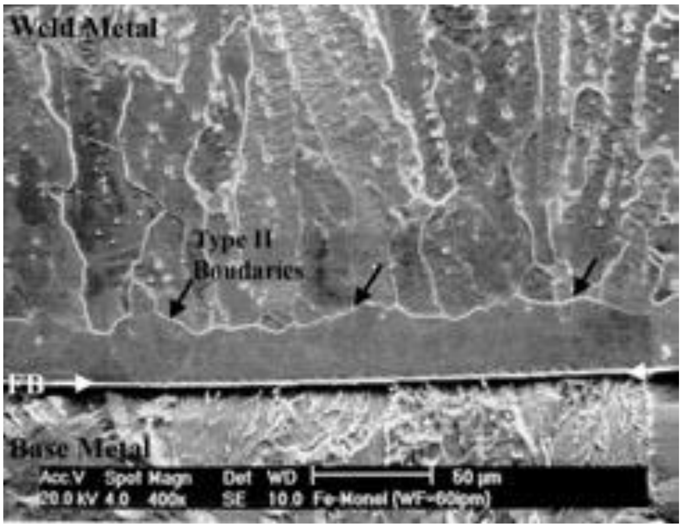

Figure 2.10 SE photomicrograph showing Type II boundaries (indicated by arrows) running parallel to the entire fusion boundary (48% BMD weld in Fe/70Ni-30Cu) [22].

Transformation from austenite phase to ferrite phase takes place upon approaching room temperature. When the welded region of weld metal and adjacent substrate enters the α-ferrite temperature range, the γ-α boundary approaches the FB from the HAZ. The α-ferrite nucleates in the austenite boundaries. As the temperature decreases, the growing α-ferrite crystals develop facets on the sides. Several other morphologies may also form, namely, Widmanstätten side plates or laths, intragranular blocky ferrite, and intragranular plates. However, the growth of α-ferrite will terminate at the FB because the weld metal is stable in FCC to below room temperature [21], [22]. The formation of type II boundary may be detrimental for the mechanical properties.

Mechanical Behaviour at the Interface

The formation of type II boundary at the interface into the austenitic material may cause cracking, as indicated in the previous section. Wang et al. [63] studied the behaviour of type II boundary for SA508-3/EQ309L weld overlay. They found that the element content was similar across the type II boundary. However, the hardness changes on the sides of the type II boundary. They also found that the type II boundary is weaker under tensile stress compared to shear stress. Under shear stress, type-II boundary suffers work hardening, while under tensile stress, type-II boundary cracks first before EQ309L necking.

In further discussions, ER70S-6 and ER316L will be chosen for study, representing HSLA steel and AUS steel respectively. This will help narrow the scope for this study. ER70S-6 is an HSLA steel with low carbon content which may help mitigate the issue regarding carbon migration at the interface to some extent. ER316L is a marine grade AUS steel which is less susceptible to SCC as discussed in the previous sections.

There are a few studies conducted on the material pair ER70S-6/ER316L [62], [64], [65], [66]. The focus of these studies has been on fabrication and the process parameters. The characterization techniques used for mechanical behaviour in these studies were microhardness and tensile properties. Yadav et al. [62] reported that the microhardness is highest at the interface. The tensile strength was reported to be superior to either of the individual materials. However, they have employed an alternative deposition technique, which is not entirely representative of weld cladding applications. For a cladding application, one material is followed by another. Suárez et al. [65] conducted a similar alternative deposition technique and obtained similar results in terms of mechanical properties. Gürol et al. [66] conducted a study on the deposition of this material pair one after the other, which is more representative of cladding. In the microstructure, they report the possibility of a carbon-depleted zone on the HSLA steel side and a carbon enrichment zone on the AUS steel side. However, they have not conducted any tests for measuring carbon composition across the interface. Instead, the reasoning for this diffusive process was supported with literature based on an HSLA steel with slightly higher carbon content. The microhardness is reported to be higher at the interface, as shown in Figure 2.11. Galán Argumedo et al. [20] also observed higher hardness at the interface and it was attributed to martensite islands in the interface region. In the study conducted by Ahsan et al. [64] the results on microhardness are similar to the ones discussed so far. In the latter two studies, the deposition is in the form of a single wall. For fabrication of large structures, the beads may be deposited side by side as well. This would be better represented by a multiwall deposit where the material is deposited in the form of a cuboid. Additionally, in cladding, the beads will be deposited on the surface of the large structure. Hence, a multi-wall deposit would be a closer approach for studying ferritic-austenitic FGMs for cladding.

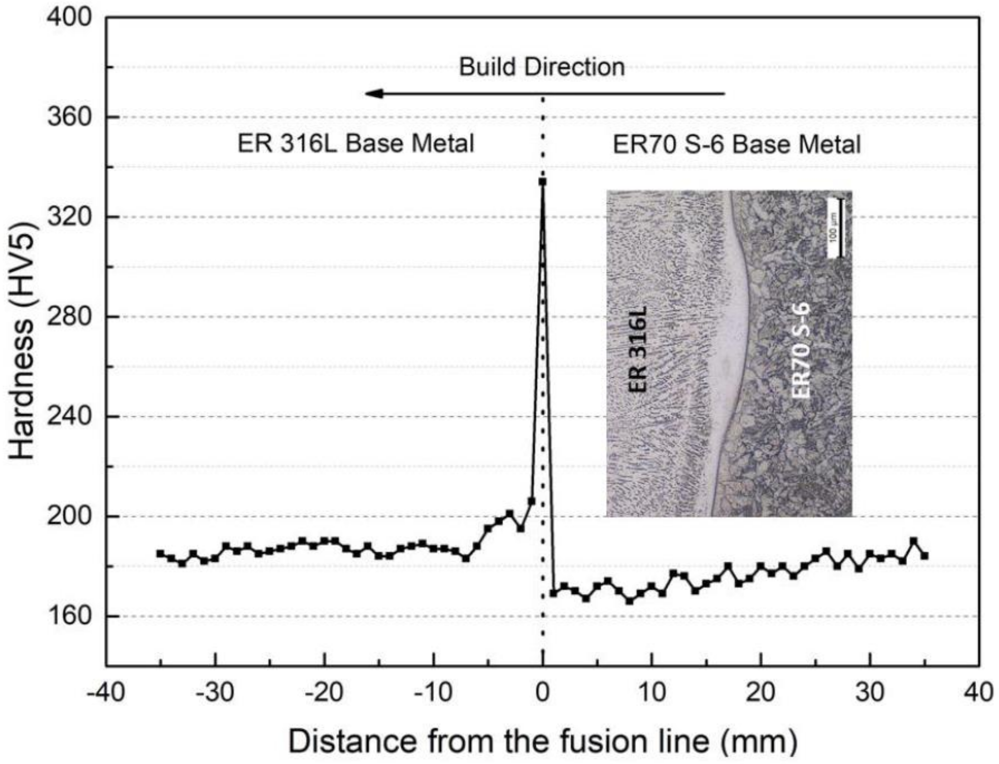

Figure 2.11 Vickers hardness test result of the as-deposited layers and interface [66].

It can be seen that most of the attention for this material pair has been on fabrication technique and the limited attention on mechanical properties has been on microhardness and tensile properties. This mandates a requirement for the understanding of the fatigue behaviour at the interface of the ER70S-6/ER316L pair. In the next chapter, the methodology for studying fatigue behaviour will be explored.

2.4. Fatigue Behaviour

Fatigue Study

Fatigue of structures is generally regarded as a significant problem [67]. Understanding the fatigue behaviour of materials is important for safe and economical application. When it comes to additively manufactured components, fatigue must be addressed separately. This is due to the process induced changes such as mechanical anisotropy, residual stress, and defects. Additionally, exposure to extreme environments must also be considered. For each new material and technique, a benchmark on fatigue crack growth tests is necessary for reliable application in the industry [68]. Understanding fatigue behaviour can be done either by modelling or by fatigue behaviour experiments. There are many theoretical models used to understand fatigue [69]. However, no model can be generalized for various loading and material conditions. Fatigue behaviour experiments can provide accurate benchmark for a material. This can also aid in further developments of models.

In the current study, the aim is to understand the fatigue behaviour of the material pair ER70S-6/ER316L. First the challenges associated with studying the fatigue behaviour of non-homogeneous materials will be discussed. This section will elaborate on the finite element method (FEM) based solutions from several researchers. Following this discussion, the basis of fatigue crack growth experiments to obtain the fatigue properties will be elaborated. Thereafter, the available benchmark of fatigue properties of mono-materials available in the literature will be discussed. After the discussion on mono-materials, the fatigue properties of various FGMs will be discussed. This will also serve as a guide to investigate the properties of the material pair of interest.

Fatigue Study of Non-homogeneous Materials

The main challenge in conducting fatigue behaviour studies on FGMs is the lack of standards. The standards for conducting fatigue crack propagation experiments, ASTM E647-23 [70] and ISO 12108 [71], are applicable only to homogeneous and linear-elastically stressed bodies. These standards cannot be used in FGMs, where the material is non-homogeneous. However, it is possible to model the FGMs using FEM to study the fatigue properties.

Several researchers [24], [72], [73], [74], [75] have conducted finite element method (FEM) based studies to investigate a suitable way to analyse FGMs. Erdogan [24] studied several fracture mechanics problems of FGMs and presented a number of stress intensity factor (K) solutions. Honein and Herrmann [74] proposed path-independent integrals for isotropic, linearly elastic bodies with smoothly varying elastic moduli and subjected to plane strain deformation fields. Gu and Asaro [73] studied crack deflections in FGMs. Several studies have been conducted to obtain suitable solutions to the stress intensity of FGMs.

However, it is also possible to obtain a customized K solution for materials of interest. This is of particular interest for additively manufactured materials where several types of non-homogeneity can be created. A customized K solution is much quicker in this case. Ghorbanpour et al. [75] obtained a customized K solution for their fatigue crack growth rate (FCGR) experiments. Each graded specimen was represented by two halves with an interface plane perpendicular to the crack. The half-span of the specimen was modelled under 2D plane strain condition. The crack was modelled at the symmetry plane of the specimen, as seen in Figure 2.12 (a). The crack length was varied from notch length to the final length of interest to study the change of the stress intensity factor during the crack growth. At the symmetry plane, displacement along the X-axis was constrained at the non-cracked edge, while a free boundary condition was applied to the crack. The interface region was divided into multiple layers with a linearly changing Young's modulus assigned to each layer. This was done to obtain K solutions without any abrupt changes. Small mesh elements were used near the crack tip, while larger elements were used outside the crack-influenced area, which reduced the computation time. J integral was calculated at the fifth contour from the crack tip, as seen in Figure 2.12 (b). K solution (K^*) was then obtained from the J integral according to,

$$K^* = \sqrt{J \times \frac{E}{1 - \nu^2}} \tag{2.1}$$

where E is Young's modulus at the crack tip, J is the integral value and ν is Poisson's ratio.

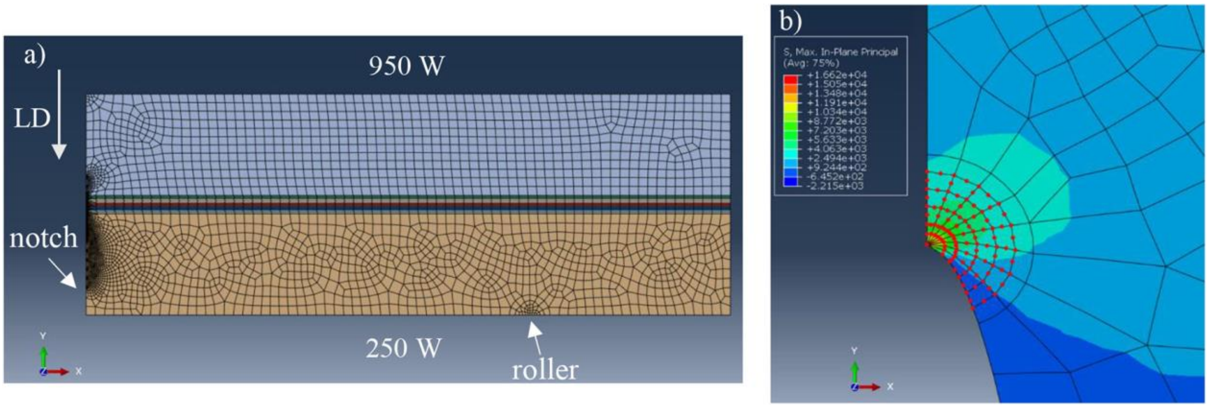

Figure 2.12 (a) Model used by Ghorbanpour et al. [75] for FEM analysis of graded samples. (b) Nodes involved in the fifth contour to calculate the J integral.

In the present study, a similar approach can be followed for obtaining a customized K solution. A solution to the stress intensity factor for FGM is necessary for studying crack propagation at the interface. The methods to study crack propagation will be discussed in the next section.

Fatigue Crack Growth Rate

FCGR experiments yield results in the form of a relation between change in stress intensity (ΔK) and crack propagation per cycle (da/dN). FCGR curve is typically in the form of a sigmoidal shape as shown in Figure 2.13. The curve has three regions. In region I, there is a threshold stress intensity (ΔK_{th}) range, below which the crack propagates at an extremely slow rate or does not propagate at all. By knowing the ΔK_{th}, the permissible crack lengths and applied stresses can be calculated. The crack growth rate increases rapidly above the ΔK_{th} value with increasing ΔK. In region II, da/dN is often a power function of ΔK. This leads to a linear relation between log(da/dN) and log(ΔK). In region III, da/dN rises to an asymptote where the maximum stress intensity factor K_{max} becomes equal to the critical stress intensity factor, K_c [76].

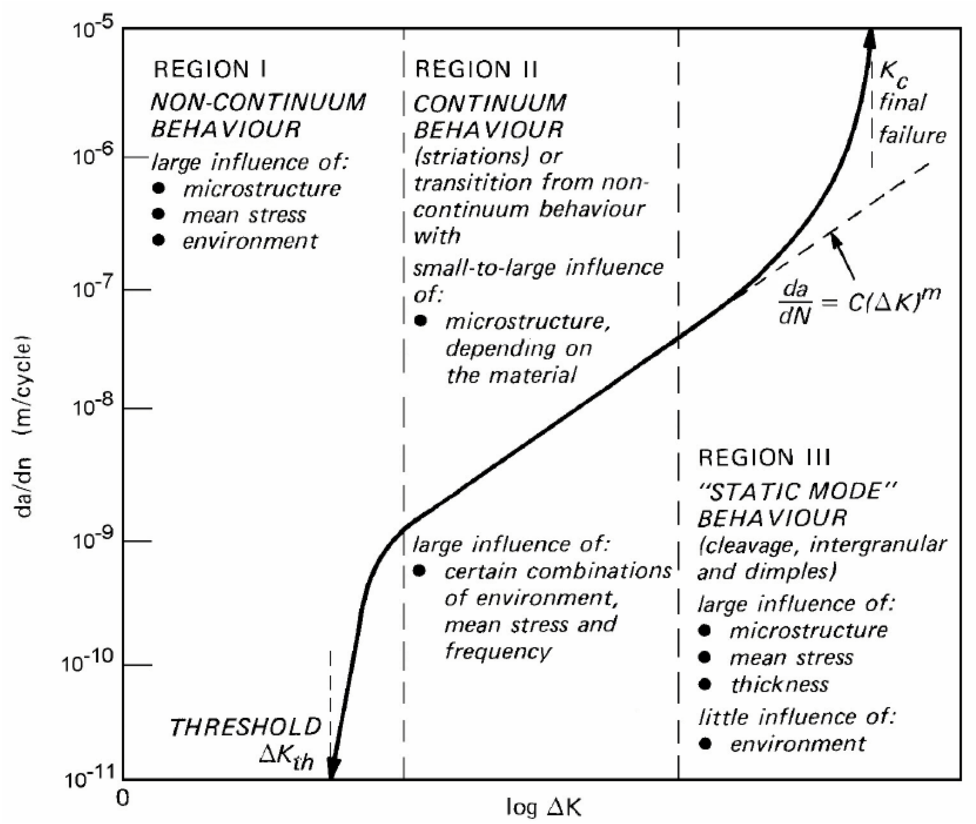

Figure 2.13 Characteristics of the fatigue crack growth rate curve da/dN – ΔK [76].

There are several semi-empirical formulae that are fitted to a set of FCGR data. The most widely known crack growth equation is the Paris equation [76], given by,

$$\frac{da}{dN} = C(\Delta K)^m \tag{2.2}$$

where m and C are empirically adjusted constants. Another equation was proposed by Forman [76] to also include the K_c,

$$\frac{da}{dN} = \frac{C(\Delta K)^m}{(1-R)K_c - \Delta K} \tag{2.3}$$

where R is the ratio of minimum stress to maximum stress, $\sigma_{min}/\sigma_{max}$. McEvily [76] developed another equation,

$$\frac{da}{dN} = C(\Delta K - \Delta K_{th})^2 \left(1 + \frac{\Delta K}{K_c - K_{max}}\right) \tag{2.4}$$

McEvily's equation applies for all three regions of the FCGR curve. Such equations are of limited significance as they are empirical in nature. However, they provide a first estimate of crack growth behaviour, especially if the material exhibits a larger stable region II.

In addition to these, experiments under constant ΔK can also be performed. In a homogeneous material, such an experiment would yield constant da/dN across the whole specimen. However, for FGMs with changing properties across the specimen, a change in da/dN can be expected. Additionally, constant ΔK tests can also be useful for studying the morphology of the fatigue fracture surface [67]. Ghorbanpour et al. [75] conducted constant ΔK experiments and correlated the microstructure with the recorded FCGR. In their study, the microstructure analysis explained the difference due to anisotropy in FCGR. Now that the basis of FCGR experiments has been elaborated, the FCGR of mono-materials and FGMs will be discussed in the next sections.

FCGR of Mono-materials

Table 2.2 shows the overview of the Paris curve parameters of single material samples. All data is for R ratio of 0.1. The available data on ER316L is limited compared to ER70S-6. Only one study on WAAMed ER316L was found, while several were found for ER70S-6. Ermakova et al. [77] investigated the crack growth behaviour of WAAMed ER70S-6 under different orientations. However, only crack propagation along the build direction was considered for this literature survey. This case is the most relevant for FGM of interest, as cladding will be deposited at the outer layer. Shamir et al. [78] investigated the FCGR at the top and bottom part of the print. Huang et al. [79] investigated the effect of the thickness of print on the FCGR. Although all the results varied a little, the C parameter was always around the magnitude 10^{-9} or 10^{-8} and the m parameter was around 3.0. Figure 2.14 (a) and (b) show the comparison of m parameter with respect to hardness and yield strength respectively, for ER70S-6. No trend is clear for yield strength. However, an increase of m may be correlated with a decrease in hardness. This means that for the same ΔK, a lower hardness may be expected to result in higher FCGR.

Table 2.2 Paris curve parameters of mono-materials, all with R=0.1 and crack propagation in the direction of build direction.

Material	Process	C (mm/cycle)	m	Comments	Reference
Steel	Welded	1.65×10^{-11}	3.00	Recommended parameters by IIW for welded steels.	A.F. Hobbacher [80]
ER70S-6	WAAM	8.34×10^{-9}	2.39	Max load 10 kN. Larger scatter reported. Standard deviation of m = 0.28. C(T) samples.	Ermakova et al. [77]
		6.64×10^{-9}	3.08	Max load 11 kN. Smaller scatter reported. Standard deviation of m = 0.09. C(T) samples.	
ER70S-6	WAAM	1.13×10^{-8}	2.88	Top part. C(T) samples.	Shamir et al. [78]
		7.01×10^{-9}	3.01	Bottom part. C(T) samples.	
ER70S-6	WAAM	3.87×10^{-11}	3.25	Nominal thickness of 3 mm. C(T) samples.	Huang et al. [79]
		1.33×10^{-11}	3.38	Nominal thickness of 8 mm. C(T) samples.	
ER316L	WAAM	1×10^{-11}	6.58	Results abnormally high compared to materials of similar composition. C(T) samples.	Ajay et al. [81]
		1×10^{-12}	6.78		
ER304L	WAAM	3.01×10^{-10}	3.79	Similar composition to ER316L. SEN(B) samples.	Gordon et al. [82]
SS316L	SLM	2.12×10^{-9}	3.37	Different production process. C(T) samples.	Riemer et al. [83]
SS316LN	Wrought	1.97×10^{-9}	3.47	Different production process. C(T) samples.	Nani Babu et al. [84]

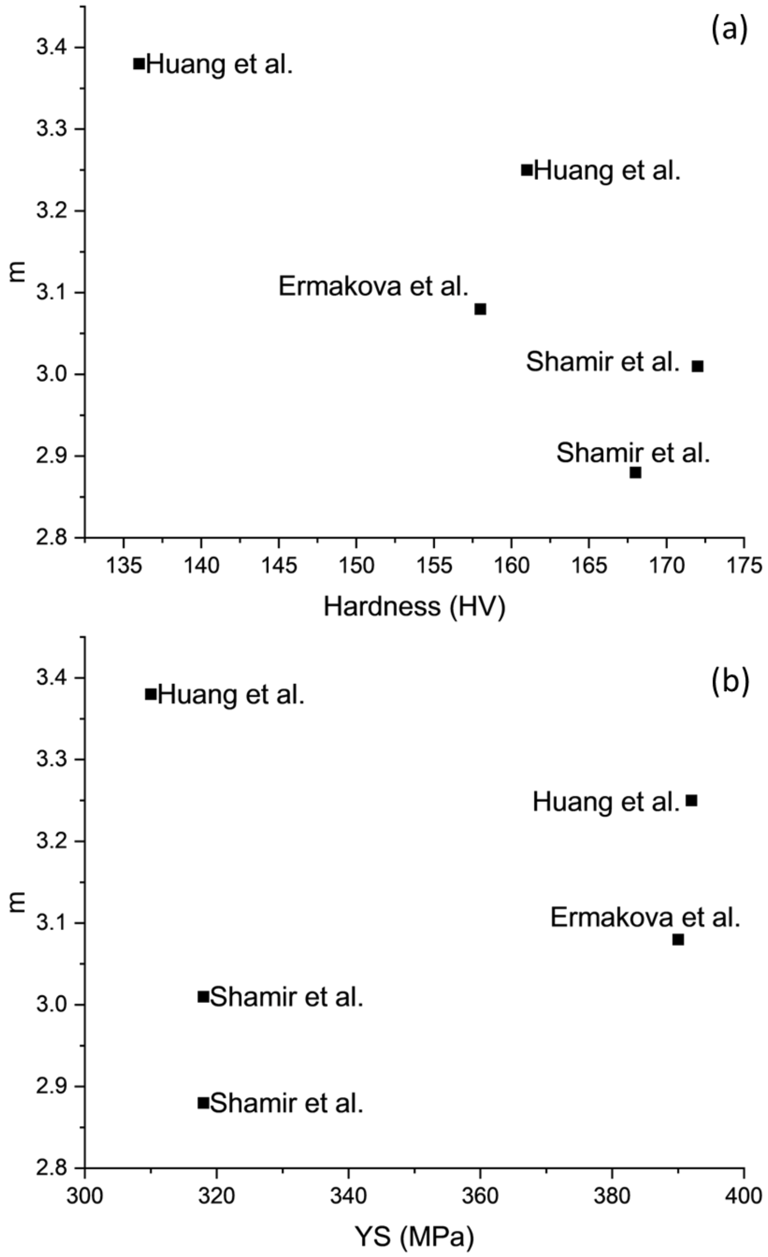

Figure 2.14 Comparison of m parameter with (a) hardness and (b) yield strength, for ER70S-6. The references from the literature used in this figure are Huang et al. [79], Ermakova et al. [77], and Shamir et al. [78].

The results of ER316L have a relatively higher variance. Ajay et al. [81] reported an m parameter of around 6.6, which is almost twice the ones reported by Gordon et al. [82] on ER304L. Although these are different materials, the difference in composition is not drastic. Hence, the explanation of the differences is uncertain. It could be possible due to the small thickness of the sample which may have resulted in plain-stress conditions. Another explanation could be that the part printed for making the sample was a single wall. Different properties could be expected when a block of material is printed where the heat of one bead affects the microstructure of the adjacent bead. SLM-printed SS316L by Riemer et al. [83] and wrought-processed SS316LN by Nani Babu et al. [84] showed similar results. In summary, all results on the m parameter of ER316L and similar materials are higher than the ones reported on ER70S-6. However, the available data has significant scatter. It is thus necessary to investigate these parameters for better reliability, especially for ER316L. No comparison to hardness or yield strength was made for ER316L due to insufficient data.

The ΔK_{th} values of mono-materials are shown in Table 2.3. In the study by Ermakova et al. [77], the ΔK_{th} values were not reported. However, an estimation based on the graph provided gives 18.0 MPa$\sqrt{\text{m}}$. However, this is much higher compared to ΔK_{th} of 10.0 MPa$\sqrt{\text{m}}$ reported by Shamir et al. [78]. Walters et al. [16] identified the ΔK_{th} value for thermomechanically rolled S460 which has a similar composition as ER70S-6, and the value of ΔK_{th} was even lower at 4.7 MPa$\sqrt{\text{m}}$. The value of ΔK_{th} of WAAMed ER70S-6 can thus be expected to be less than 10.0 MPa$\sqrt{\text{m}}$ at R ratio of 0.1. The ΔK_{th} values for WAAMed ER316L were not reported in any study. Riemer et al. [83] reported ΔK_{th} of 3.0 MPa$\sqrt{\text{m}}$ for SLM-based SS316L. Further studies on welded ER316L and ER316LN were reported by Samuel et al. [85] and Poonguzhali et al. [86]. Both their studies did confirm the decreasing ΔK_{th} value with R ratio, with 11.12 MPa$\sqrt{\text{m}}$ for R-0.1 and 8.5 MPa$\sqrt{\text{m}}$ for R=0.5. Both ER70S-6 and ER316L based on WAAM need to be studied for ΔK_{th} for better reliable data.

Table 2.3 ΔK_{th} values of mono-materials.

Material	Process	ΔK_{th} (MPa$\sqrt{\text{m}}$)	Comments	Reference
ER70S-6	WAAM	10.0	R = 0.1	Shamir et al. [78]
ER70S-6	WAAM	18.0^*	*Not reported. Estimated based on Fig 5 of the reference. R = 0.1	Ermakova et al. [77]
S460	Thermomechanical rolling	4.7	This value is for room temperature. Several temperature conditions reported. R = 0.1	Walters et al. [16]
SS316L	SLM	3.0	R = 0.1	Riemer et al. [83]
ER316LN	Welded	11.12	R = 0.1	Samuel et al. [85]
		9.13	R = 0.4	
SS316	-	6.5	Base metal, process not reported. R = 0.1	
		5.9	Base metal, process not reported. R = 0.4	
ER316LN	Welded	8.5	R = 0.5	Poonguzhali et al. [86]

Crack Closure

It was seen that there is a correlation between the R ratio and ΔK_{th}. The dependence of the R ratio on crack propagation rates has also been studied in the past [76, p. 213]. In general, a more positive R ratio will result in higher FCGR. This dependence of FCGR on the R ratio is often explained by the crack closure phenomenon. Elber [87] in the 1970s discovered the phenomenon of crack closure. He found that fatigue cracks are closed for a significant portion of a tensile load cycle, owing to residual plastic deformation left in the wake of a growing crack. This phenomenon is called plasticity-induced crack closure. Another form of crack closure is roughness-induced crack closure. The contact of the fracture surfaces caused by the misfit of the microscopically rough fracture surfaces is denoted as roughness-induced crack closure. Upon extension of a crack, the newly exposed surface can react with the environment to form an oxide layer.

The build-up of the oxide layer can cause oxide-induced crack closure [88]. In a metastable austenitic stainless steel, deformation can cause the transformation of austenite into martensite at the crack tip. The FCC to BCC transformation results in a volume increase of 2.57%. The volume increase around the crack flanks can result in increased crack closure effects [89].

Due to crack closure, the crack surfaces exert forces on each other before fully unloading. The load drops before reaching the minimum displacement. The stress intensity factor corresponding the actual lower limit of the load is called effective minimum stress intensity factor $K_{min,eff}$, also denoted as K_{op}. For accurate measurement of FCGR, the effective stress intensity factor, ΔK_{eff} should be considered, which is given by,

$$\Delta K_{eff} = K_{max} - K_{min,eff} \tag{2.5}$$

ΔK_{eff} is lesser than ΔK. Table 2.4 shows the K_{op} values for HSLA steel and AUS steel reported in the literature. The effects of crack closure and plastic zone size can be understood through fatigue tests under various R ratios. This may provide a better understanding of the behaviour of FGMs, which will be discussed in the next section.

Table 2.4 K_{op} values reported in literature.

Material	K_{op} (MPa√m)	Reference
HSLA steel	4.2 at K_{max}=22.22 MPa√m and R=0.1, SANH-55 steel	Dhar [90]
AUS steel	7.8 at K_{max}=22.22 MPa√m and R=0.1, SS304L	Vor et al. [91]

FCGR of FGMs

The available studies on FCGR study of FGM are limited. No studies on the ER70S-6/ER316L combination were found in the literature, as concluded in the previous chapter. However, for conducting experiments on this material pair, it can be helpful to look into studies of other material pairs.

Jiang et al. [92] conducted a study on fatigue crack propagation normal to a plasticity mismatched bi-material interface formed by 20G and 1Cr18Ni9Ti. Under the condition where the crack propagates from lower-strength ferrite material to higher-strength austenite material, the crack growth is shown in Figure 2.15. A decrease in crack growth rate was observed by Jiang et al. for a crack growing from the low to high-strength material.

Cortes et al. [93] studied the fatigue behaviour of monolithic IN718 and AL6XN base materials and IN718-AL6XN dissimilar welds. The weld metal of the IN718-AL6XN dissimilar weld was reported to have a higher FCGR as compared to the IN718 and AL6XN parent materials. It was unexpected as the plastic zone was similar between AL6XN and the weld metal of the IN718-AL6XN dissimilar weld. The high crack growth was associated with secondary phases present in the weld. This indicates that phases present in the interfaces may also impact the FCGR.

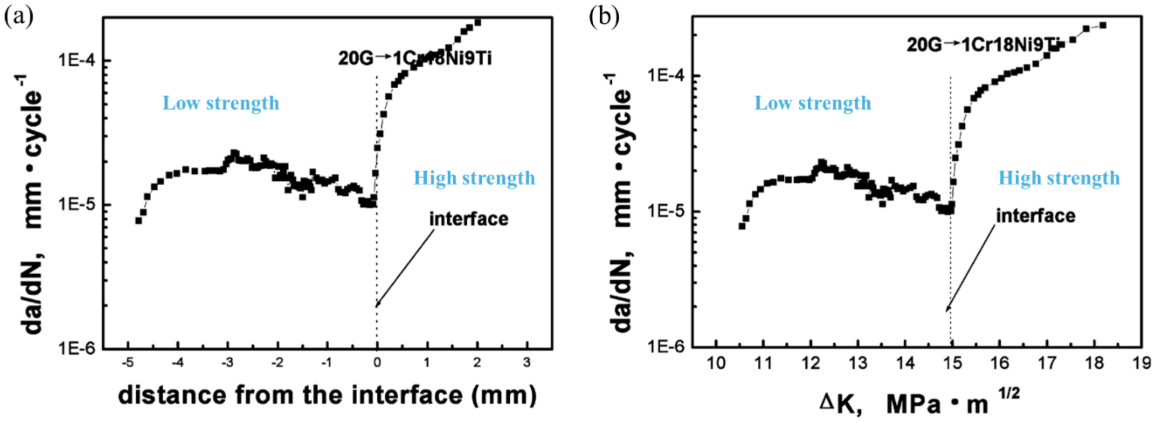

Figure 2.15 The crack growth rate under increasing ΔK conditions for a BM of 20G and 1Cr18Ni9Ti [92]. A decrease in crack growth rate can be noted at the interface.

Duval-Chaneac et al. [94] studied layered specimens of IN718 and SS316L produced by LPBF. Though the material and process are not of primary interest, their study might be helpful in understanding the techniques implemented to study FGM. They studied the crack propagation of bi-material, initiated from both the IN718 side as well from the SS316L side. They obtained region 2 of the FCGR curve. Additionally, they conducted constant ΔK experiments throughout the bi-material from soft to hard material. The crack propagation speed changed across the interface. They also conducted SEM-based fractography and identified transgranular and inter-granular crack growth modes. It was concluded that the grain structure and orientation greatly affected the crack propagation rates, especially at lower ΔK levels.

A similar set of experiments was conducted by Ghorbanpour et al. [75]. They investigated the effect of microstructural anisotropy on the fatigue behaviour of functionally graded IN718 produced by laser powder bed fusion (LPBF). Different laser parameters were used to achieve functional grading. They conducted fatigue experiments to obtain regions 1 & 2 of the FCGR curve of mono-materials. They conducted constant ΔK experiments for graded material. A variation of crack propagation rates with the orientation of the samples was observed. Additionally, a correlation with hardness was found for crack propagation rate. Lower hardness resulted in higher crack propagation. Further, the influence of thermal cycles on the formation of detrimental Laves phases as well as on fatigue was also investigated. The path followed by the crack was also carefully studied. The influence of meltpool boundaries, interface, grain boundaries, and grain orientations on the deflection of the crack was analysed using optical microscopy, scanning electron microscopy (SEM) and electron backscatter diffraction (EBSD). The EBSD analysis helped them in understanding the crack path. The grain orientations that influenced crack deflections were identified. The grain boundary misorientation was correlated with crack branching. Both intergranular and transgranular crack growths were observed. It may be noted that constant ΔK experiments might be a useful experiment. These tests could provide an understanding of the influence of different load ratios, microstructures, and crystal orientations.

The constant ΔK experiments may also provide insights into changing plastic zones along the interface. During crack propagation, the stresses at the crack tip need to overcome the local potential energy ahead of the crack tip. This region of a certain radius is representative of the plastic zone size ahead of the crack tip. The applied load will determine the radius of the pseudo-plastic zone ahead of the crack tip, for a given geometry and yield strength. However, during the crack propagation through dissimilar material, the yield stress follows a gradient that will cause changes in the local stress field. The change in the local stress field changes the necessary potential energy to overcome crack propagation. When the yield stress increases in a transition gradient from soft to hard, the crack tip driving force is decreased. This causes a crack propagation deceleration, also known as a shielding effect [94].

The effects of crack closure can also be understood through constant ΔK experiments. The analytical study by Pippan et al. [95] on cracks perpendicular to the interface of a plastically mismatched composite material revealed a change in crack closure effects. Upon studying the crack tip opening displacement (CTOD) of a crack passing from lower to higher strength material under cyclic loading, they predicted a decrease in CTOD near the boundary. Their conclusions suggest that the crack closure effects may increase as the crack approaches the interface. This results in the ΔK_{eff} to be progressively lower as the crack approaches the interface, thereby reducing the crack growth rate. In experimental work, Pippan et al. [96] verified this phenomenon as seen in Figure 2.16. These conclusions are also in coherence with the observations by Jiang et al. [92] as seen in Figure 2.15.

In addition to crack closure effects, Pippan et al. [96] also noted the crack branching at the interface. They attributed this feature to the change in the shear band angle. In a homogeneous material, the shear bands are inclined 45-80° to the propagation direction. However, at the vicinity of the interface, this value approaches values larger than 90°, resulting in crack branching.

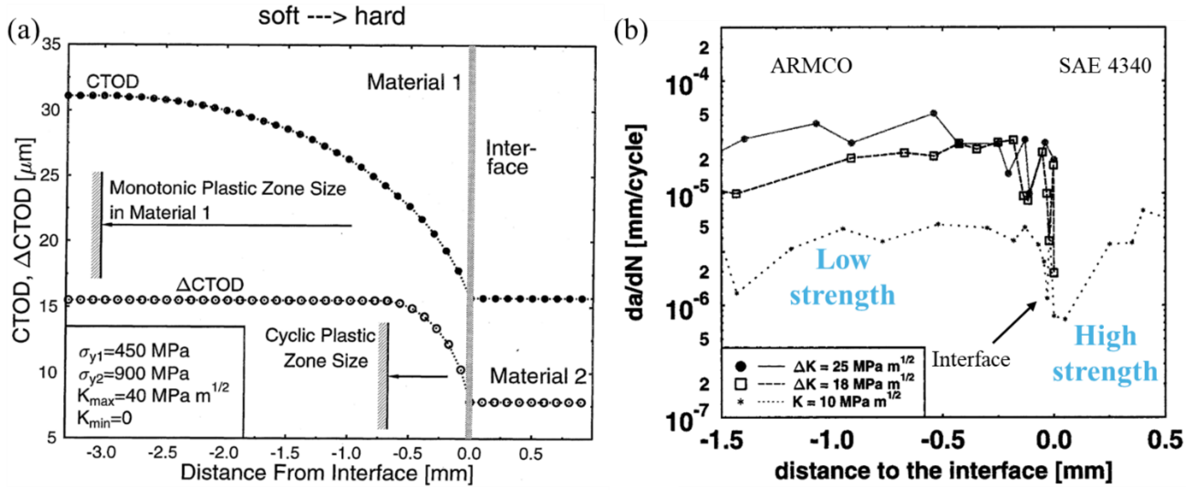

Figure 2.16 (a) The analytical study showing decreasing CTOD of a monotonic plastic zone and cyclic plastic zone when the crack passes from a material of lower strength to higher strength (Pippan et al. [95]). (b) Constant ΔK experiment for crack passing from lower strength ARMCO to higher strength SAE 4340. A decrease in the crack growth rate at the interface can be noted (Pippan et al. [96]).

The studies mentioned so far indicate the methodology that could be followed to understand the interface of FGMs. Increasing ΔK experiments can be done to understand region 2 at the interface region. Decreasing ΔK could be done to understand the threshold regime of the interface. However, for FGMs, constant ΔK experiments appear to be the popular method. Constant ΔK allows the isolation of one parameter and makes the study of other parameters easier. This experiment would also enable an understanding of the effects of plastic zone size at the interface as well as the effects of the R ratio. Additionally, optical microscopy, SEM, and EBSD may be useful for correlating the effects of microstructures and crystal orientations on the crack growth behaviour.

2.5. Summary

FGMs are an innovative approach to have tailored properties within different parts of a structure. AM is a suitable method for producing FGMs. WAAM is capable of creating larger parts due to its superior deposition rate. This is suitable for marine, aerospace, and energy industries. WAAM of HSLA steels provides an opportunity to produce structures with a better strength-to-weight ratio. However, HSLA steels face severe disadvantages due to stress corrosion cracking and ductile to brittle transition. A technique to overcome this problem is to clad the HSLA steel part with a corrosion-resistant material, such as AUS steel. WAAM can be implemented to produce an FGM of HSLA steel and AUS steel.

FGMs of ferritic-austenitic steels have been studied in the literature. The properties at the interface of FGMs are different from the mono-materials due to the different composition and microstructure. The different microstructural development results from the unique chemistry at the interface resulting in differences of properties. For HSLA-AUS steel FGMs, some studies have been conducted to understand the mechanical properties at the interface. However, most of the attention has been given to hardness and tensile properties. Little to no attention has been given to fatigue properties. This literature survey focused on the material pair ER70S-6/ER316L and their fatigue behaviour. For the interface formed by this material pair, no benchmark for fatigue behaviour was found.

It is important to understand the fatigue behaviour for reliable application in the industry. One way of obtaining this is through FCGR experiments. The required parameters for understanding FCGR at the interface are the Paris curve parameters and threshold stress intensity factor. The influence of the load ratio on the crack propagation can provide an understanding of the effects of crack closure. Studies on the mono-materials ER70S-6 (HSLA steel) and ER316L (AUS steel), as well as some related materials, were found for benchmarking. To understand the various techniques used to study fatigue on FGMs, other material pairs were also reviewed. To understand the effects of microstructure on fatigue behaviour microscopy, fractography and electron backscatter diffraction can be used. The features that can be analysed are the fracture surface, striations, defects, grain size and phases present.

2.6. Research Objectives

After conducting a literature review on functionally graded HSLA steel (ER70S-6) and AUS steel (ER316L) fabricated through wire arc additive manufacturing, the following research objectives are formulated to address the research gaps:

- **Study and benchmark of fatigue properties of HSLA and AUS steel.**

  Approach: Constant force amplitude test and threshold stress intensity range experiments are conducted to obtain the Paris curve parameters and threshold stress intensity factor respectively. Constant ΔK experiments are conducted to understand the variation of crack propagation rates at different R ratios. Anisotropy in fatigue crack growth rate is quantified by testing samples in two orthogonal directions. A comparison with the literature is done.

- **Study and benchmark of fatigue properties at the interface of functionally graded HSLA and AUS steel.**

  Approach: Constant force amplitude test and threshold stress intensity range experiments are conducted to obtain the Paris curve parameters and threshold stress intensity factor respectively. Constant ΔK experiments are conducted to understand the variation of crack propagation rates at different R ratios. Anisotropy in fatigue crack growth rate is quantified by testing samples in two orthogonal directions. A comparison with the mono-materials is done.

- **Investigate the influence of the microstructure on crack propagation at the interface.**

  Approach: Constant ΔK experiments aided by microscopy, fractography, and electron backscatter diffraction analysis will help understand the effects of different microstructural features. The features to be studied include fracture surface, striations, defects, grain size and phases present.

3. Materials and Methods

3.1. Materials

The functionally graded material was deposited in the form of a rectangular block. The block of material used in this study is the same as the one used by Galán Argumedo et al. [20]. "For deposition, the proprietary welding consumables of the Voestalpine Boehler 3Dprint brand were selected." The names of the consumables are 3Dprint AM 46 and 3Dprint AM 316L for HSLA steel and AUS steel respectively. The compositions of these materials are shown in Table 3.1. The properties of these materials comply with the commercial specifications AWS A5.9 [97] ER316L and AWS A5.18 [98] ER70S-6. The tensile properties of the deposited materials were benchmarked by Galán Argumedo et al. [20] and are shown in Table 3.2.

Table 3.1 Chemical composition of wire materials in wt%. [20]

Material	C	Si	Mn	Cr	Ni	Mo	N	Fe
3Dprint AM 46 (HSLA steel)	0.1	1	2	-	-	-	-	Bal.
3Dprint AM 316 L (AUS steel)	0.02	0.5	2	19	12	2.6	0	Bal.

Table 3.2 Yield strength, tensile strength, and elongation after fracture for bi-metal tensile specimens, and AUS steel and HSLA steel benchmark values. (*) Necking occurs outside of gauge length. [20]

Material	Yield strength σ_y [MPa]	Tensile strength σ_u [MPa]	Elongation at fracture Δ/L_0 [%]
Bi-metal interface (AUS steel layer 1)	411 ± 11.9	592 ± 10.7	19.8 ± 4.9 (*)
AUS steel WAAM benchmark	392 ± 6.27	592 ± 23.8	29.7 ± 1.3
HSLA steel WAAM benchmark	576 ± 19.5	667 ± 19.5	24.5 ± 2.1

The WAAM process was carried out with a Fanuc M710iC/12 L series robot shown in Figure 3.1.

> "The CMT-capable power source, wire feeder, controller and cooling unit area are proprietary Fronius systems. The first 54 mm height consists of 16 layers of 3D print AM 46. Each layer consisted of 33 beads 205 mm in length and approximately 3.5 mm in height. For each layer, all beads were deposited in the same direction with a 25% bead width overlap, and in the opposite orientation for the subsequent layer." [20]

This is schematically represented in Figure 3.2.

> "After the HSLA steel layers were deposited, the top beads were machined flat to begin welding the subsequent 37 mm block height of 3D print AM316L material. The latter layers were completed with 26 beads per layer and 16 layers in total, averaging a total layer height of about 2 mm." [20]

Further details on deposition parameters are given in the materials and methods section of the study by Galán Argumedo et al. [20].

From the deposited block of material, SENB specimens were machined through milling. The three types of materials extracted were ER70S-6 specimens, ER316L specimens, and Bi-metallic/Bi-material (BM) specimens. Each of these is machined in two horizontal orientations, namely, longitudinal and transverse. The schematic of the BM specimens and their orientations are shown in Figure 3.3. The mono-materials of ER70S-6 and ER316L are similar in orientation except for the absence of an interface. The dimensions of the specimens and the loading rollers are in accordance with the standard ISO12108 [71].

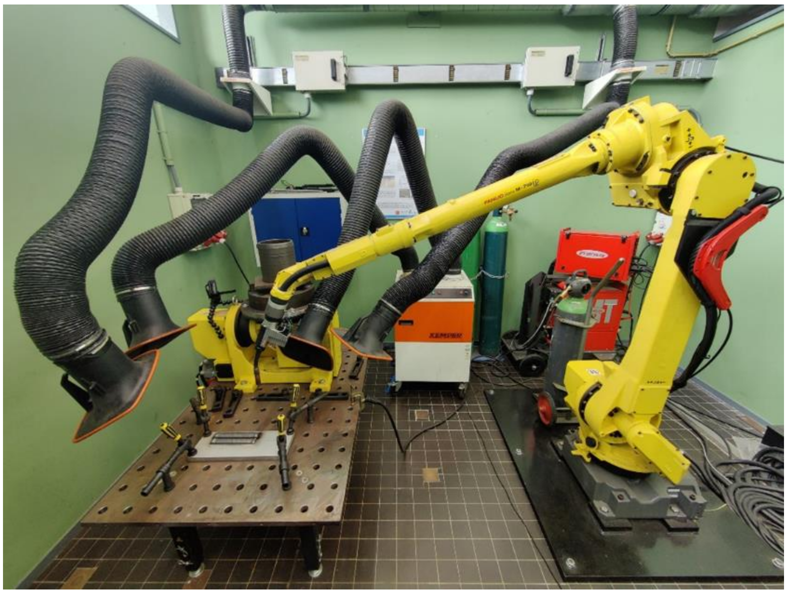

Figure 3.1 Fanuc M710iC/12 L WAAM robot.

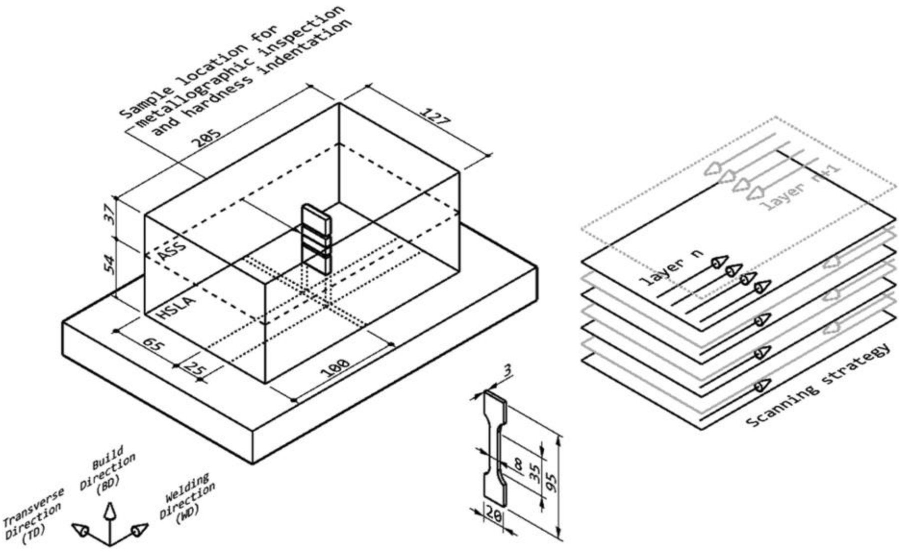

Figure 3.2 Deposition strategy and dimensions of bi-material block used by Galán Argumedo et al. [20] for studying tensile properties, microstructural characterization and microhardness. The same block of material was used in this study for fatigue tests.

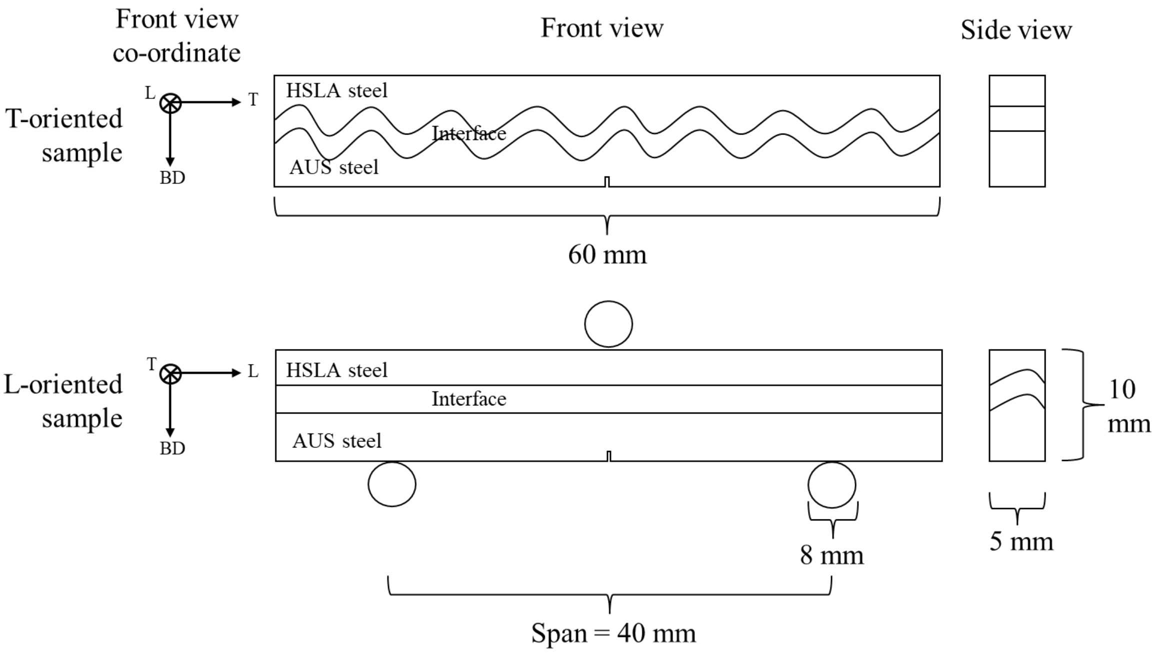

Figure 3.3 BM specimens with the convention of co-ordinates followed in this study: L-longitudinal or along the welding direction, T-transverse or perpendicular to welding direction on the same plane, BD-build direction or the direction along the height of the build. The L-oriented specimen has a straight interface at the front and a non-uniform interface along the thickness. Vice versa for the T-oriented specimen.

All additive manufacturing techniques produce residual stresses to some degree as explained in section 2.2. The distortion pattern reported in the literature is that the far ends of the part bend along the build direction [99]. This was also observed in the current study. In the present work, pre-heating of the base plate was done, and constant inter-pass temperature was maintained during WAAM deposition, to minimize the effects of residual stresses. Moreover, the volume of the test specimen is 0.12% smaller than the deposited block. This may lead to a lesser effect of residual stresses during fatigue tests. However, the residual stresses were not measured in the current study to limit the scope. For the construction of large parts, the study of residual stresses is important and should be conducted in a future study. Additionally, post-weld heat treatment can also be done for residual stress relief. X-ray diffraction can be incorporated to study residual stresses in combination with several heat treatments.

3.2. Fatigue Crack Propagation

3.2.1. Experimental Setup

Three-point bending fatigue tests were performed on single-edge notched bending (SENB) specimens. Cyclic loads were applied using a servo-hydraulic MTS machine with a loading capacity of 25 kN equipped with the MTS MultiPurpose TestWare and Flextest electronic control unit. The fatigue setup is shown in Figure 3.4. At the bottom of the specimen, a steel platform with two rollers provides two loading points. These rollers were held together with a spring to maintain equal distance. This platform was mounted to the lower grip of the MTS machine. The third loading point was provided by a roller attached to the upper grip of the machine.

Three-point bending tests were conducted employing fatigue test configurations and stress intensity solutions as described in ASTM E399 [100]. The equation for stress intensity solution is given by,

$$K = \frac{P.S}{B.W^{\frac{3}{2}}} f\left(\frac{a}{W}\right) \qquad 3.1$$

where K is the stress intensity factor, P is the load, S is the span, B is the thickness, W is the width, and a is the crack length. The f(a/W) is given by,

$$f\left(\frac{a}{W}\right) = 3\sqrt{\frac{a}{W}}.\frac{1.99 - \left(\frac{a}{W}\right)\left(1 - \frac{a}{W}\right)\left[2.15 - 3.93\frac{a}{W} + 2.7\left(\frac{a}{W}\right)^2\right]}{2\left(1 + 2\frac{a}{W}\right)\left(1 - \frac{a}{W}\right)^{\frac{3}{2}}} \qquad 3.2$$

Reference marks, with 0.5 mm intervals, were fabricated on the surface of the specimens from the edge of the notch up to 7.5 mm. For visual crack calibration, a stereo microscope was used.

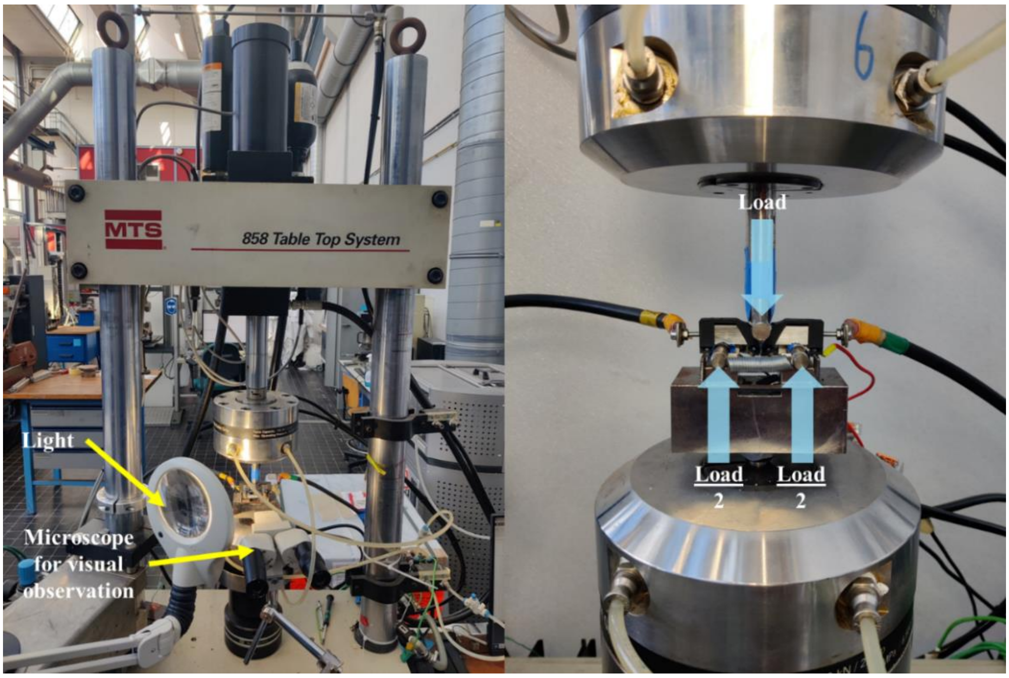

Figure 3.4 The MTS machine used for fatigue tests and the 3-point bending setup.

Direct current potential drop (DCPD) equipment from the Howden brand was used for crack measurement. A typical crack length measurement resolution of about 0.05 mm is obtained from this machine. A polymer clamp system was designed to facilitate stable connections of the DCPD probes as well as to ensure the proper symmetry of the attached probes with respect to the notch. The clamp system shown in Figure 3.5 was made using FormLabs 3B stereolithography (SLA) 3D printer using the proprietary Black Resin. A spacer was also 3D printed to maintain the same distance of the voltage probes for all specimens. The nose and the rollers were electrically insulated to prevalent parallel paths for the current. Most procedures followed for the DCPD method were in accordance with ISO12108 [71, p. 12108]. However, the temperature fluctuations were not measured for this system. The temperature fluctuations can arise due to a high frequency of testing, due to applied current, and variation in air temperature over-night. A sensitivity analysis of the DCPD technique accounting for these variables should be done in a future study.

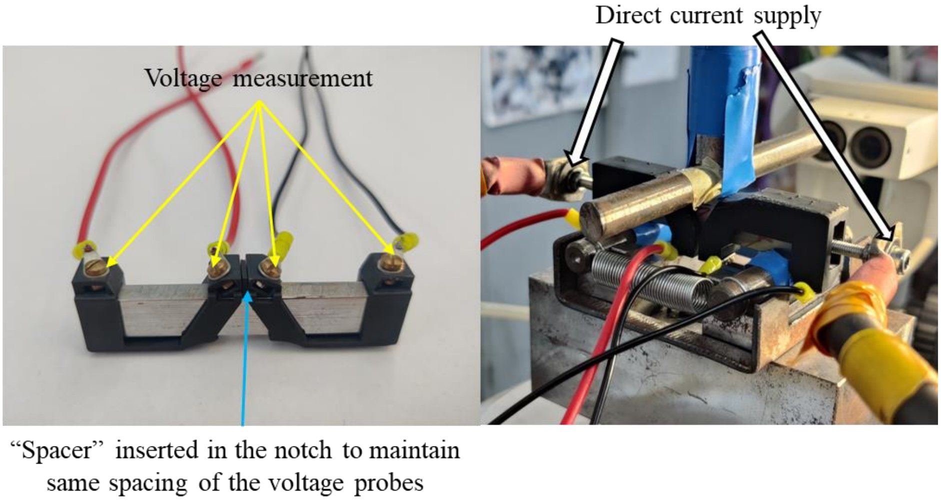

Figure 3.5 The DCPD setup made with 3D printed polymer clamps. The voltage probes are attached with tightened screws on the specimen. The spacer makes sure equal spacing of the voltage probes. The current supply is applied through bolts inserted into a 5 mm threaded hole on the sides of the specimens.

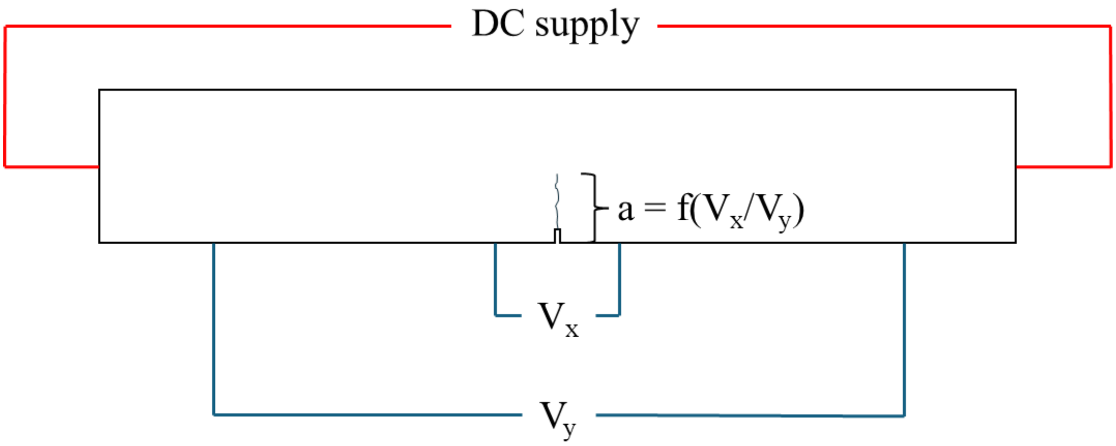

Figure 3.6 Schematic of potential drop technique for crack measurement.

The DCPD probes take voltage signals from four points as shown in Figure 3.6. The inner and outer probe voltage signals are called V_x and V_y respectively. The V_x is divided by V_y to obtain a signal V that is independent of the applied current. The current is set such that the V_x and V_y do not go beyond the maximum range of the DCPD equipment. For each reference mark, the signal was noted. A polynomial fit of the second degree was used to fit the correlation. Table 3.3 shows the DCPD parameters and the equation to correlate the voltage signal and crack length for each material. The equation for BM can vary slightly with respect to the position of the interface. This could result in errors in the crack measurement. A future study for the normalisation of this variation is required for improving and standardisation of methodology.

Table 3.3 The polynomial equations relating crack length (a) with the measured signal from DCPD (V) for each type of material.

Material	**Current (A)**	**Crack length equations a = f(V) (mm)**
HSLA steel	8.5	$a = -0.0806V^2+2.0401V-3.7407$
AUS steel	4.5	$a = -0.0894V^2+2.1197V-3.9770$
BM-L	7.5	$a = -0.0683V^2+2.1714V-4.1766$
BM-T	7.5	$a = -0.0898V^2+2.4182V-4.5891$

3.2.2. Fatigue Tests and Parameter Selection

Pre-fatigue

Pre-fatigue of all specimens was done under reducing ΔK condition. The equation used for this operation is,

$$\Delta K = \Delta K_0 \exp[C(a - a_0)] \tag{3.3}$$

where ΔK_0 is the initial ΔK, C is the gradient chosen to be -0.02, a_0 is the notch length and a is the instantaneous crack length. The K_{max} at the end of the pre-fatigue was kept lower than the K_{max} at the start of the fatigue test. This is in accordance with the standard ASTM-E647 [70].

In constant ΔF tests, all specimens were pre-fatigued to a 2 mm crack length. In threshold stress intensity range tests, the specimens were also pre-fatigued to 2 mm for mono-materials. The exception for this case was HSLA steel where due to a defect near the notch the specimens were pre-fatigued beyond 2 mm. For BM specimens, the pre-fatigue was done up to 1.5 mm away from the fusion boundary of HSLA steel. In constant ΔK tests, almost all specimens were pre-fatigued to 2 mm. The exceptions in this case were a few HSLA steel specimens where due to a shortage of specimens, threshold specimens needed to be re-used. This essentially resulted in pre-fatigue larger than 2 mm.

Constant Force Amplitude Tests

Constant force amplitude tests or constant ΔF tests were performed to formulate the crack growth rate as a function of stress intensity range (ΔK). The Paris regime can be obtained in this manner. The crack growth rate tests were done at a frequency of 15 Hz and based on the standard ASTM-E647 [70]. All tests were done at an R ratio of 0.1. The selection of force amplitudes for mono-materials was made by referring to the literature. Ermakova et al. [77] studied the FCGR of ER70S-6 and Gordon et al. [82] studied the FCGR of ER304L. Based on the ΔK range in the Paris regime in these studies, the force amplitudes were chosen for this study and are shown in Table 3.4. The choice for BM was made after preliminary ΔK_{th} tests of mono-materials. It was found that region I of the FCGR curve is much lower than expected. Hence for BM, the test was done at a lower force amplitude. Moreover, this makes sure that the interface region is tested under a similar stress intensity condition as mono-materials.

Table 3.4 The force amplitudes selected for each material.

Material	Force Amplitude (N)
HSLA steel	1620
AUS steel	1575
BM	1260

Threshold Stress Intensity Range Tests

Constant K_{max} tests were done to determine the threshold stress intensity range (ΔK_{th}). Initial preliminary tests under a constant R ratio with decreasing ΔK were done. However, under long cracks, small ligaments and low ΔK, the force amplitude required was too low. The control system was incapable of applying very low force amplitudes under high frequencies. Hence, the constant K_{max} test was adopted.

The ΔK_{th} tests were conducted with a K_{max} of 14 MPa√m at a frequency of 60 Hz and an initial load ratio of R = 0.5 (where R = K_{min}/K_{max}), which then was increased to R = 0.8 and R = 0.9. The value of K_{min} was adjusted using the equation,

$$K_{min} = K_{min0} \exp[C(a - a_0)] \tag{3.4}$$

where K_{min0} is the value of the initial K_{min}, C is the stress intensity gradient, a0 is the initial crack length, and a is the instantaneous crack length. C is given by the equation,

$$C = \left(\frac{1}{K}\right).\left(\frac{dK}{da}\right) \tag{3.5}$$

Where K is the stress intensity and dK/da is the gradient of stress intensity with respect to the crack length. For this study, the value of C was chosen to be −0.4 mm^{-1}. The recommended gradient according to ASTM-E647 is -0.08mm^{-1} or algebraically lesser values. The low gradient suggested by the standard is to avoid crack deceleration. However, a larger gradient was chosen to obtain as many data points as possible in the interface region, which is approximately 2 mm in width. As the test is conducted under constant K_{max} conditions, the effect of deceleration is negligible. This technique has been applied in literature as well [75], [101]. Additionally, a K_{max} test will provide a conservative threshold value as the crack closure effects will subside at higher R ratios.

K_{min} was calculated and adjusted at intervals of 0.1 mm. The adjustment process was carried out until the crack did not grow by 0.1 mm in 1,000,000 cycles, which indicates a crack growth rate of 10^{-7} mm/cycle or less. For measuring the threshold value the standard procedure in ASTM E647 [70] was followed. The linear interpolation of log(da/dN) vs log(ΔK) with at least 5 points between 10^{-6} mm/cycle and 10^{-7} mm/cycle was done. The intercept of the interpolated line at 10^{-7} mm/cycle was taken and the corresponding ΔK value was taken as the threshold.

For BM, pre-fatigue was done up to 1.5 mm away from the visible fusion boundary of HSLA steel. The initial K_{max} was chosen to be the same as the mono-material. However, the initial ΔK was slightly larger than for mono-materials to test under slightly larger force amplitudes. This was also to overcome the limitations of the machine.

Constant Stress Intensity Range Tests

To evaluate the effect of the changing microstructure on the crack growth rate behaviour, the BM specimens were examined under constant stress intensity range (constant ΔK) condition. At a given ΔK level the FCGR is a constant value for a particular microstructure. Thus, maintaining a constant ΔK should reveal the effect of the functionally graded structure and the interface on the FCGR. Constant ΔK tests on mono-materials were also conducted as a benchmark. The tests were conducted at 15 Hz under ΔK of 20 MPa√m at R=0.1 and R=0.5. The different R ratios would result in different plastic zone sizes and different crack closure effects.

For the constant K_{max} and constant ΔK tests, the loads were adjusted automatically during crack growth. The program takes the DCPD signal, calculates the crack length and adjusts the force level to obtain the desired K value. For constant K_{max} tests, the load adjustment was done after every increment of 0.1 mm. For constant ΔK tests, the load adjustment was done continually.

However, the standard K solutions for determining the load levels for homogenous materials do not apply to the functionally graded structures. The adaptation in the K solution is explained in the next section.

3.3. FEM-based K-solution for FGM

The FEM analysis was done in a similar approach as Ghorbanpour et al. [75], which was explained in section 2.4. The J-integral was calculated at a fixed contour ahead of the crack tip. The difference in approach is in the interlayers. In the present study, the straightness and position of the interface are consistent in all directions. Assuming straight interlayers for the interface may not be accurate for the analysis. Moreover, considering curved interlayers may add to the complexity of the problem. Hence, in the current approach, the interface is considered as a single line instead of multiple interlayers.

The results of the FEM analysis are shown in Figure 3.7. The x-axis refers to the position of the interface relative to the width of the specimen. The y-axis refers to the ratio of crack length to the width of the specimen. The graphs provide the ratio of the J integral of the BM with respect to the J-integral of the mono-material. Additionally, the ratios of crack mouth opening displacement and compliance can also be seen. The correction factor for the K-solution is then based on the equation,

$$K_{BM} = K_{MM}\sqrt{\frac{J_{BM}}{J_{MM}}} \tag{3.6}$$

where BM is bi-material, MM is mono-material, K is the stress intensity factor, J is the J-integral, and the square root of the J-integral of BM to MM is the correction factor. J-integral of linear elastic mono-material is the same as G [76]. Based on this correction factor, a polynomial fit can be made which is then utilised for K-solution of the BM fatigue specimens. Figure 3.8 shows an example graph of an equation of correction factor for an interface at Z(BM)/W=0.5, or halfway through the specimen. For constant ΔK tests, a simplified version of this correction factor was used which is explained in Appendix 7.1.

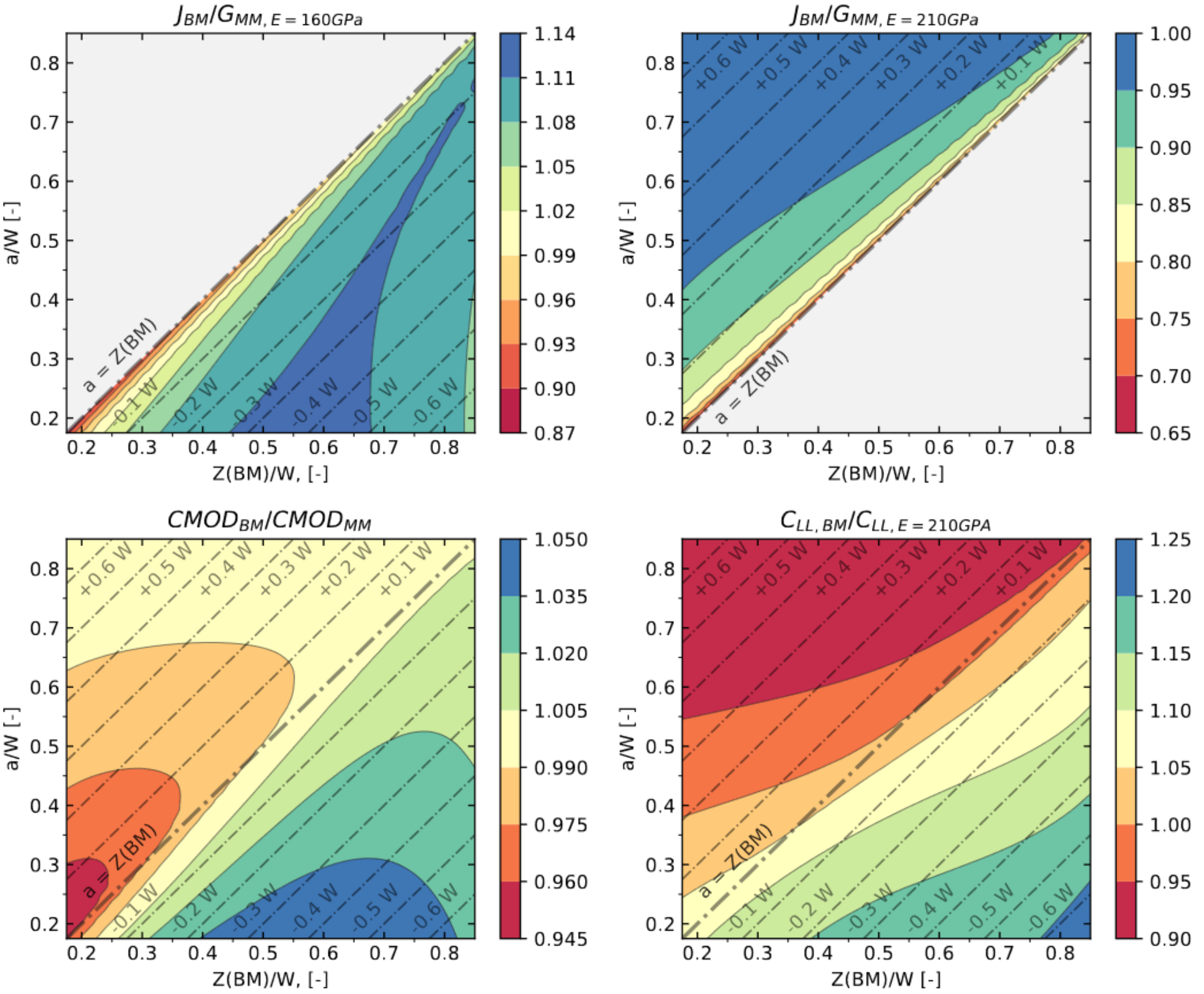

Figure 3.7 The results of FEM analysis. The X-axis shows the ratio of the distance of the interface to the width of the specimen and the Y-axis shows the ratio of instantaneous crack length to the width of the specimen. The top left and right images show the ratio of J-integral of bi-material (BM) to mono-material (MM) of ER316L and ER70S-6 respectively. The bottom left image shows the Crack mouth opening displacement (CMOD). The bottom right image shows the ratio of compliance of BM to MM of ER70S-6.

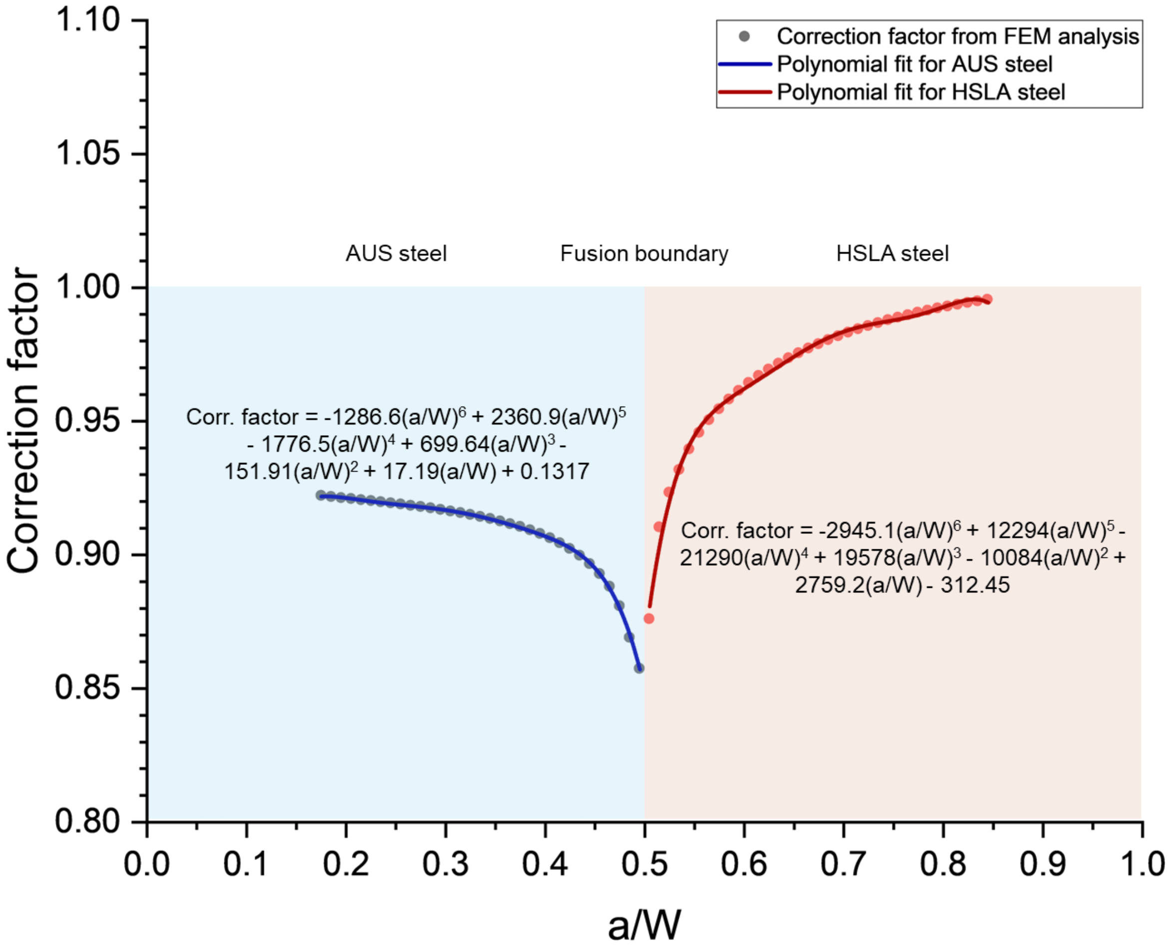

Figure 3.8 An example of the correction factor with respect to the instantaneous crack length for an interface halfway through the material.

3.4. Microstructure and Fractography

For microstructure characterization, the specimens were cut and mounted on a resin with hot moulding. The specimens were ground with SiC paper grits #320 through #4000 and were polished with 3µm and 1µm diamond suspensions. For EBSD analysis, the specimens were further polished with colloidal silica suspension (OP-S) for a minimum of 30 min. For optical microscopy, the specimens were etched after polishing. The etchant used for HSLA steel was 5% Nital solution and for AUS steel was Kallings No. 2. For BM specimens, etching with Nital does not affect AUS steel and etching with Kallings No. 2 would preferentially etch HSLA steel due to galvanic effects [20]. Hence, the HSLA steel part was initially covered during Kallings No. 2 etching and then Nital was used to etch the whole specimen. This procedure may often result in over-etching of the HSLA steel at the fusion boundary as shown in Appendix 7.3 However, on rare occasions, this procedure can reveal microstructural features at the fusion boundary of HSLA steel.

For fracture surface analysis, the specimens were fractured using different approaches for different materials. For AUS steel, the specimens were first tempered at 350°C for 15 mins. This created an oxide layer of yellow colour. The specimens were then fractured under tension. For HSLA steel specimens and BM specimens, liquid nitrogen was used to cool the specimens below the DBTT of HSLA steel. The specimens were then fractured under bending.

Several instruments were used to characterize the microstructural properties of the interface region for correlation with fatigue behaviour. Optical microscopy was carried out using an OLYMPUS BX60M Digital Microscope and Keyence VHX 5000 Digital Microscope under epi-illumination. Hardness was measured with Zwick DuraScan 20. Fractography was carried out using Keyence VHX 7000N Digital Microscope. Scanning Electron Microscopy was also used for fractography with a JEOL JSM-IT100 InTouchScope™ Scanning Electron Microscope at an accelerating voltage of 20 kV. For EBSD mapping, JEOL JSM-6500 F Field-Emission Gun Scanning Electron Microscope was used at 15 kV and 13nA. The specimens were tilted 58° away from the horizontal. EBSD mapping was made by a FEI® SEM-Quanta FEG 450 SEM with an integrated EDAX detector. All inverse pole figure (IPF) maps show colour mapping with <001> direction along the perpendicular direction to the mapped plane. The step size used for the mapping is indicated in the captions of each EBSD map.

4. Results and Discussion

4.1. Microstructure Characterization

The macrostructure of graded material is shown in Figure 4.1. This figure highlights the three layers of the FGM. The microstructure of each part of this structure is shown in Figure 4.2. HSLA steel is composed of ferrite contained in packets bound by prior austenite grain (PAG) boundaries. The PAGs are oriented towards the weld pool centre which is consistent with the observations in the literature [20]. The grains formed at the boundary of these PAGs are grain boundary ferrites. The needle-like features within these are the acicular ferrite. The presence of acicular ferrite and absence of polygonal or pearlite in HSLA steel is consistent with the literature as discussed in Section 2.3. On the other hand, for AUS steel, the microstructure mostly consists of large columnar austenite grains mostly oriented in the build direction. The dark etched regions in the AUS steel are δ-ferrite. Hence the grains for AUS steel are almost fully FCC structure.

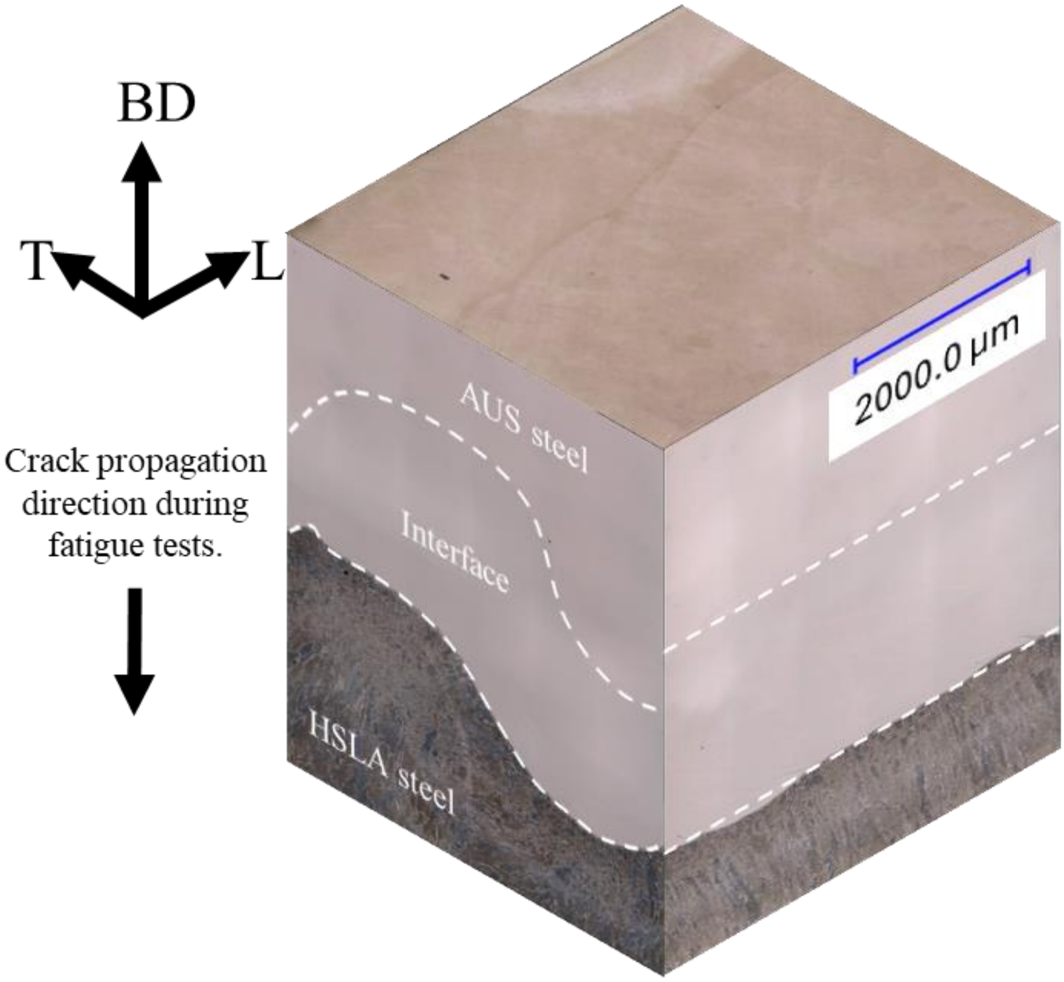

Figure 4.1 Three-dimensional macroscopic characteristics of the WAAMed FGM. The three regions with the fusion line are highlighted. T – transverse, L – longitudinal, BD – build direction. The etchant for interface and AUS steel would preferentially etch ferrite. Hence, interface and AUS steel were not etched.

Figure 4.2 (c) shows the fusion boundary between the interface and HSLA steel. In the FB some needle-like features can be observed. Such features were also observed within the interface region as shown in Figure 4.2 (d). These features are most likely to be martensite, which is also reported in the literature [20].

Some porous defects were noted for T-oriented specimens in HSLA steels as shown in Figure 4.3. No such defects were observed in AUS steel micrographs. Porous defects can be formed due to contaminations in the weld metal or due to poor path planning as explained in section 2.2. However, the defects were absent for L-oriented specimens. This could suggest that the defects are non-spherical and were process-induced. The most likely reason would be the improper hatch spacing of the weld beads. If the fatigue crack passes through the pore, an increase in the crack growth rate can be expected due to a lack of material ahead of the crack tip. In such a case, the pores should also be further investigated during fractography.

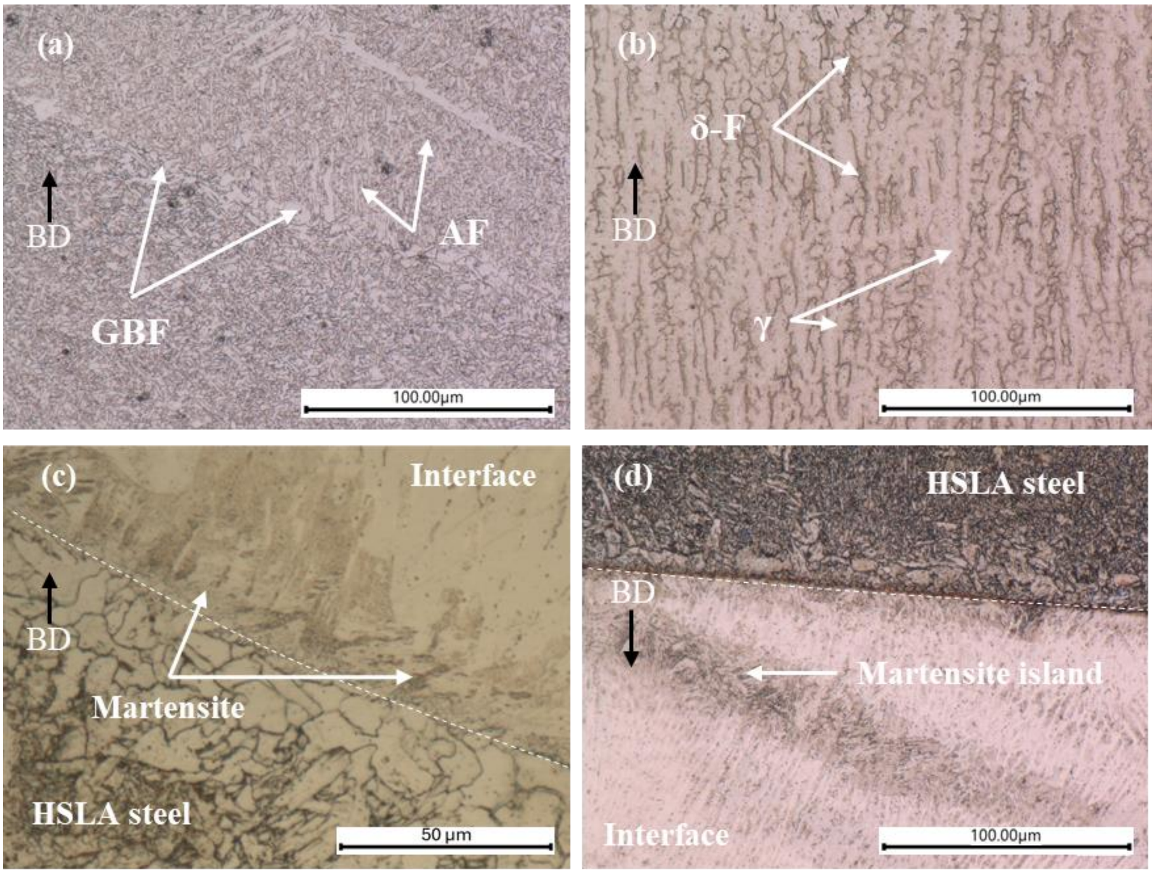

Figure 4.2 The microstructure of (a) HSLA steel, (b) AUS steel, and (c) and (d) fusion boundary between interface and HSLA steel. GBF – grain boundary ferrite, AF – acicular ferrite, γ – austenite, δ-F – delta ferrite, and BD – build direction. Martensite at the fusion boundary and in the interface can be noted.

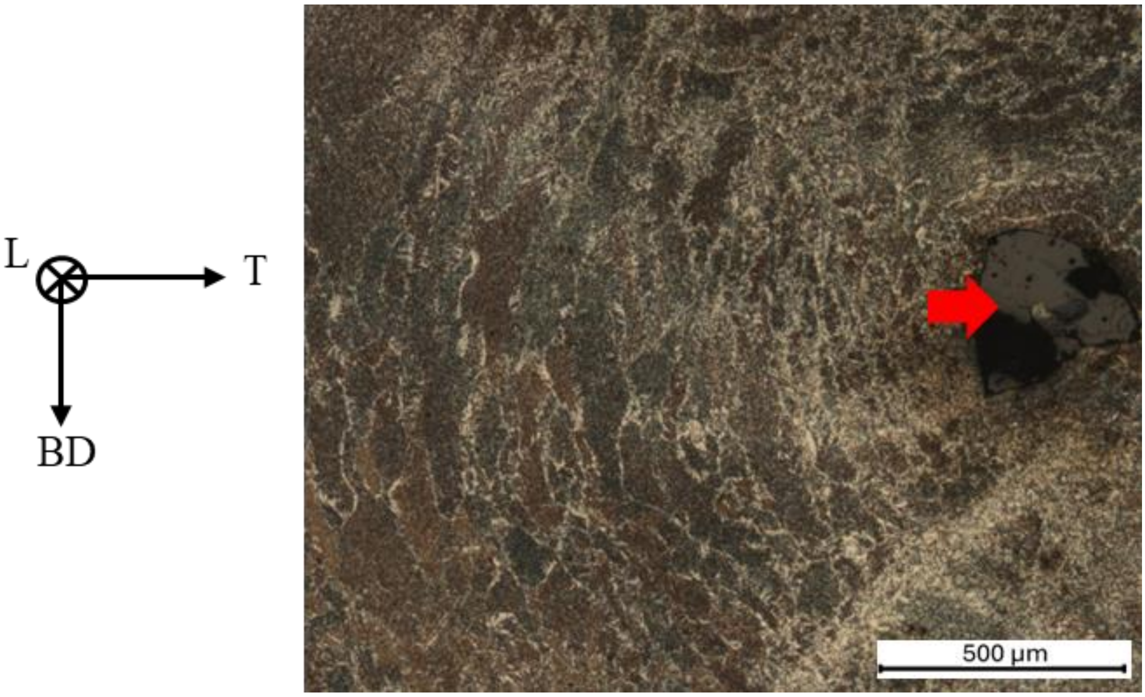

Figure 4.3 Porous defect seen in a T-oriented HSLA steel specimen. T – transverse, L – longitudinal, and BD – build direction.

4.2. Fatigue Behaviour

The fatigue behaviour of the FGM was studied in two parts: mono-material specimens and bi-material (BM) specimens. The mono-material specimens were studied to obtain a benchmark of the WAAMed material and to compare it with the literature. This benchmark data was also used for comparison with the observations in the study of BM specimens. Each material was studied under two orientations and three types of tests as explained in materials and methods. In this section, the results of these tests and their correlations with the microstructure and literature will be done. The order of experiments shown are constant ΔF tests, ΔK_{th} tests, and constant ΔK tests.

4.2.1. Fatigue Behaviour of Mono-materials

Constant Force Amplitude Tests

The Paris regime for mono-material specimens was obtained through constant ΔF tests. Figure 4.4 shows the Paris regime of the mono-material specimens in L and T directions. Table 4.1 shows the Paris curve parameters obtained by curve fitting using the Paris equation 2.2. The curve fitting was done between 20 and 40 MPa√m, to maintain consistency among all specimens. For HSLA steel, the intercept and slope are 8% and 16% less than the reported values by Ermakova et al. [77]. However, these differences are within the measurement error in the present work. For AUS steel, these values are more comparable to ER304L reported by Gordon et al. [82], than ER316L reported by Ajay et al. [81]. The L-orientation had 9% more intercept and 20% more slope, while the T-orientation had 7% lesser intercept and 5% lesser slope, when compared to values reported by Gordon et al. [82]. The L-orientation has a greater difference than the error margins of the experiment. However, consistency in the trend is maintained between

HSLA steel and AUS steel. HSLA steel has 77% and 43% lower slope parameters in L and T orientations respectively. This trend is as expected from the literature. The lower slope parameter can be interpreted as a greater crack growth resistance for HSLA steel in comparison to AUS steel.

Table 4.1 The Paris parameters of mono-materials in both orientations obtained in this work and their comparison with the values reported in the literature. The tests were conducted at R = 0.1 and a frequency of 15 Hz.

Material	Log(C)	m	Literature	Comments
ER70S-6 (HSLA) - L	-7.52 ± 0.55	2.58 ± 0.31	Log(C) = -8.18, m = 3.08 Ermakova et al. [77] (ER70S-6)	The value from the experiment is lower than the literature. No anisotropy was observed.
ER70S-6 (HSLA) - T	-7.37 ± 0.38	2.51 ± 0.23		
ER316L (AUS) - L	-10.40 ± 0.85	4.57 ± 0.59	Log(C) = -14, m = 6.58 Ajay et al. [81] (ER316L) Log(C) = -9.52, m = 3.79 Gordon et al. [82] (ER304L)	The value from the experiment is more comparable to ER304L than ER316L. Anisotropy observed. Larger scatter compared to HSLA steel.
ER316L (AUS) - T	-8.85 ± 1.08	3.61 ± 0.68		

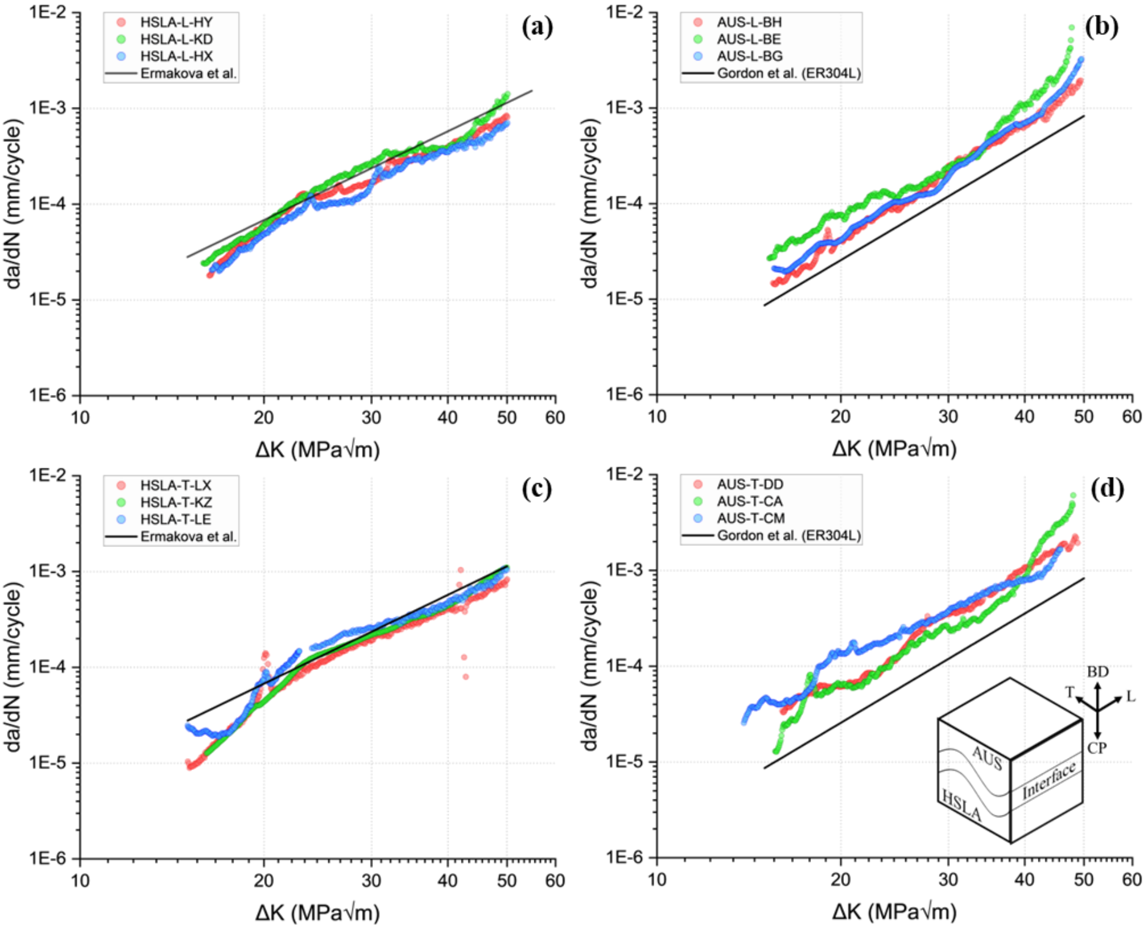

Figure 4.4 The Paris regime of (a) HSLA-L, (b) AUS-L, (c) HSLA-T, and (d) AUS-T specimens. Each colour within the graph denotes a different specimen. The tests were conducted at R = 0.1 and a frequency of 15 Hz. The figures show three repetitions per condition. The reference lines used are Ermakova et al. [77] for HSLA steel and Gordon et al. [82] for AUS steel.

A couple of factors that could affect crack growth are grain size and slip systems. Finer grains or more grain boundaries are known to resist crack growth [75], [76]. Larger grains are capable of accommodating more slip due to fewer constraints to slip in comparison to small grains. The number of slip systems can also play a role. Hence, there are competing factors affecting crack growth. HSLA steel has smaller grains and a smaller amount of slip systems. AUS steel has larger grains and more slip systems. However, a better crack growth resistance of HSLA steel compared to AUS steel is seen in the present study and the literature. This may suggest that grain size plays a dominant role compared to slip systems in the crack growth resistance for the loads in constant ΔF tests.

The grain size also played a role in the larger scatter and anisotropy in the parameters for AUS steel in comparison to HSLA steel. Due to the larger grain size, the effects of the orientation of the crystal and the bead structure play a role in the deformation ahead of the crack tip for AUS steel. This may result in lesser homogeneous behaviour of the AUS steel. In a T-oriented AUS steel specimen, the thickness of the specimen is oriented along the direction of the weld bead. Hence, the crack is passing through a single bead at a time. However, in an L-oriented AUS steel specimen, the crack passes through at least two beads at a time. The different beads will have slightly different orientations of grain growth during solidification. This may be the reason for the observed anisotropy and scatter in the AUS steel. The Paris slope parameter of L-orientation for AUS steel is 26.5% higher than T-orientation. For HSLA steel this difference is 2.78%. HSLA steel with a small grain size may behave more homogeneously and thus shows no anisotropy. Comparison of anisotropy for L and T directions with the literature is difficult as most studies do a comparison of horizontal (L and T direction) with the vertical direction (build direction). However, in such a comparison, anisotropy is reported by both Gordon et al. [82] and Ajay et al. [81].

Another factor that is influenced by grain size is the hardness. In section 2.4, the hardness of the HSLA steels was compared with the slope of the Paris regime from the literature. Table 4.2 shows the hardness values of HSLA steel and AUS steel in the present study. For HSLA steel, upon integrating the hardness and parameter ‘m’ with the reported values in the literature, the slope follows a trend with respect to the hardness as shown in Figure 4.5. A power law equation was used to fit this trend as shown in equation 4.1. The parameter ‘m’ of HSLA steel from the present study is also shown in the graph. A difference of 3.6% was noted between predicted and observed values.

$$m = 52.98 \times HV^{-0.56} \qquad 4.1$$

Table 4.2 Measured hardness of mono-materials.

Material	Hardness (HV5)
HSLA steel	247.0 ± 6.1
AUS steel	227.7 ± 5.5

A comparison for the AUS steel with hardness was not done. The available data from the literature on WAAMed ER316L is limited as seen in Table 2.2. The hardness values were also not reported in all available studies. Moreover, the anisotropy displayed by AUS steel in the present study adds to the complexity of such an analysis. However, HSLA steel shows 8.5% more hardness than AUS steel, which may also explain the better fatigue resistance.

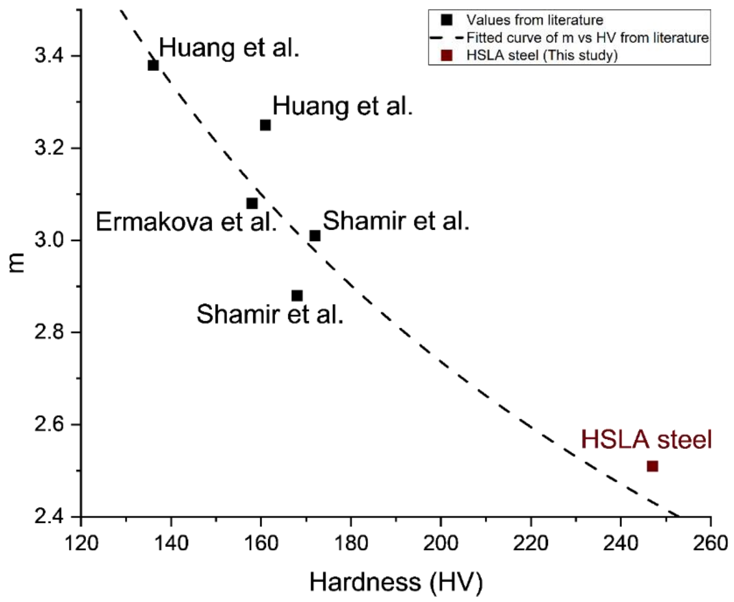

Figure 4.5 The m vs HV of reported values in literature. The dotted line is the fitted power law curve based on the literature values. The value corresponding to the HSLA steel in the present study is shown as well. The references from the literature used in this figure are Huang et al. [79], Ermakova et al. [77], and Shamir et al. [78].

To understand the correlation between the grain size and the Paris slope parameter, the microstructure reported in the literature was used. The grain sizes were approximated using the Heyn linear intercept method from ASTM E112-13 [102]. The results of these approximations are shown in Table 4.3. It can be seen that in the current study, the grain size is smaller than seen in the literature. This explains the difference in hardness. Smaller grains have a large number of grain boundaries and grain boundaries restrict the movement of dislocations. Grain boundaries also resist crack propagation. Therefore, hardness can be used to indirectly predict the Paris slope parameter and the fatigue resistance for HSLA steels.

Table 4.3 The comparison of approximate grain sizes (in diameter) of literature and the present study.

Study	**Hardness (HV)**	**m**	**Approximate grain size (diameter) (μm)**
Ermakova et al. [77]	158	3.08	14.4
Shamir et al. [78]	172	3.01	5.1
HSLA steel (This study)	247.0 ± 6.1	2.51 ± 0.23	2.7

Threshold Stress Intensity Range Tests

Another aspect that is a measure of crack growth resistance at lower load amplitudes is the threshold stress intensity range. The FCGR graphs from ΔK_{th} tests are shown in Figure 4.6. Table 4.4 shows the ΔK_{th} values of both materials under both orientations. Threshold values are obtained at an R ratio of 0.8 to 0.9. The effects of crack closure subside above R=0.7 [75], [101]. Hence, the threshold values obtained are closer to effective ΔK_{th} or $\Delta K_{th,eff}$. Comparison of the threshold values with literature is difficult as most studies in literature conduct threshold experiments at R=0.1. With lower load ratios, the effects of crack closure are likely to have been introduced, resulting in increased ΔK_{th} reported in the literature [78], [85]. Additionally, as explained in section 3.2.2, it was not possible to conduct experiments under this condition due to the limitations of the machine. Furthermore, there is only one threshold study available for WAAMed ER70S-6 and none for ER316L.

The threshold values of the HSLA steel compared to AUS steel are 7% higher for L-orientation and 15% higher for T-orientation. As HSLA steel has more grain boundaries, there are higher crack-resisting features compared to AUS steel. This could result in a higher threshold value. However, the differences between HSLA and AUS steel are within the error margins of the experiment.

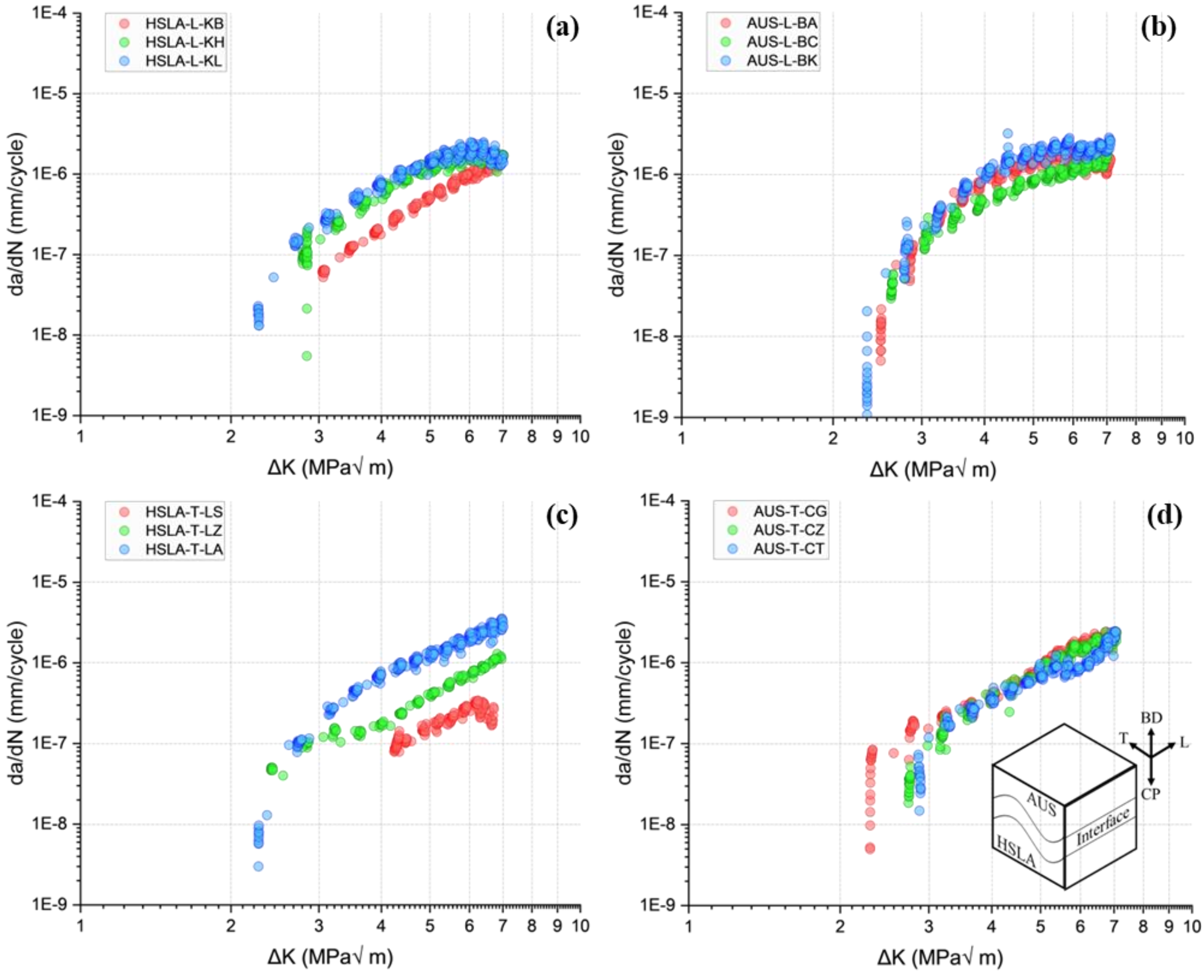

Figure 4.6 The threshold region mono-materials of (a) HSLA-L, (b) AUS-L, (c) HSLA-T, and (d) AUS-T specimens. The tests were conducted at K_{max} = 14 MPa√m, R = 0.5 to 0.9, and a frequency of 60 Hz. The figures show three repetitions per condition.

There is a larger scatter observed for HSLA steel compared to AUS steel. This is in contrast to the observations in constant ΔF tests, where AUS steel displayed more scattering. A possibility is an error in the measurement of DCPD. The error associated with the DCPD system increases with the crack length. This is explained in appendix 7.4. Another possibility is that at lower ΔK levels, the slip systems may also be playing a role along with the grain boundaries. AUS steel has more slip systems than HSLA steel and can deform easily. However, in the present study, it was not possible to verify this and should be investigated in a future study. Testing ΔK_{th} under different K_{max} conditions can be a good approach. Lower K_{max} will have plastic zone size of the order of the grains. This may result in a larger influence of the grain orientations. A larger plastic zone with higher K_{max} can have a lesser influence of a single grain ahead of the crack tip. Coupled with texture analysis, the effect of grain size and the slip systems can be further studied.

Table 4.4 The threshold values measured from the ΔK_{th} experiments for mono-materials. The tests were conducted at K_{max} = 14 MPa√m, R = 0.5 to 0.9, and a frequency of 60 Hz.

Material	ΔK_{th}	Literature
ER70S-6 (HSLA) - L	2.85 ± 0.44	ΔKth = 10.0 Shamir et al. [78] ER70S-6, WAAM, R=0.1
ER70S-6 (HSLA) - T	3.04 ± 0.38	
ER316L (AUS) - L	2.67 ± 0.19	ΔKth = 11.12 Samuel et al. [85] ER316LN, Welded, R=0.1
ER316L (AUS) - T	2.63 ± 0.26	

AUS steel did not display anisotropy for ΔK_{th} tests. This could be due to the low K_{max} value resulting in a small stress field ahead of the crack tip. Smaller stress fields may hinder the effect of the bead structure of the weld deposit. For further verification of anisotropy, an average value across the specimen with controlled parameters is required. This can be done with constant ΔK tests at a fixed R ratio.

Constant Stress Intensity Range Tests

A constant ΔK test would provide an average crack propagation throughout the specimen. The average da/dN is shown in Figure 4.7. The FCGR graphs of mono-materials and the data associated with them are shown in Appendix 7.5. The average da/dN at R=0.5 was observed to be higher than at R=0.1. This is due to the reduced effect of crack closure at a higher R ratio, resulting in the ΔK to be closer to ΔK_{eff} [76]. The difference in the average crack growth rate between the two R ratios is 50% higher for HSLA steel in comparison with AUS steel. The numerical values of these differences are shown in Table 4.5.

From the values reported in the literature, AUS steel has a higher K_{op} than HSLA steel due to higher ductility. These values are shown in Table 2.4, although the material and process are different from the present study. This may mean that as the R ratio is increased, ΔK approaches ΔK_{eff} with a lower R ratio for HSLA steel than AUS steel. For further verification, it is necessary to measure the crack tip opening displacement (CTOD) of the fatigue specimens at different R ratios. Such an experiment would provide an accurate measurement of K_{op}. This was not done in the current study as the specimens are too small to attach a clip-on gauge.

AUS steel displayed variation in crack growth rate with respect to the orientation. The L-orientation showed an increase of 61.7% for an R ratio of 0.1 and 37.9% for an R ratio of 0.5, in comparison to the T-orientation. These differences are more than the errors associated with the measurements. This is similar to the results in constant ΔF test results. Hence, the anisotropy in AUS steel can be confirmed, possibly due to the reasons mentioned previously. HSLA steel on the other hand does not show anisotropy.

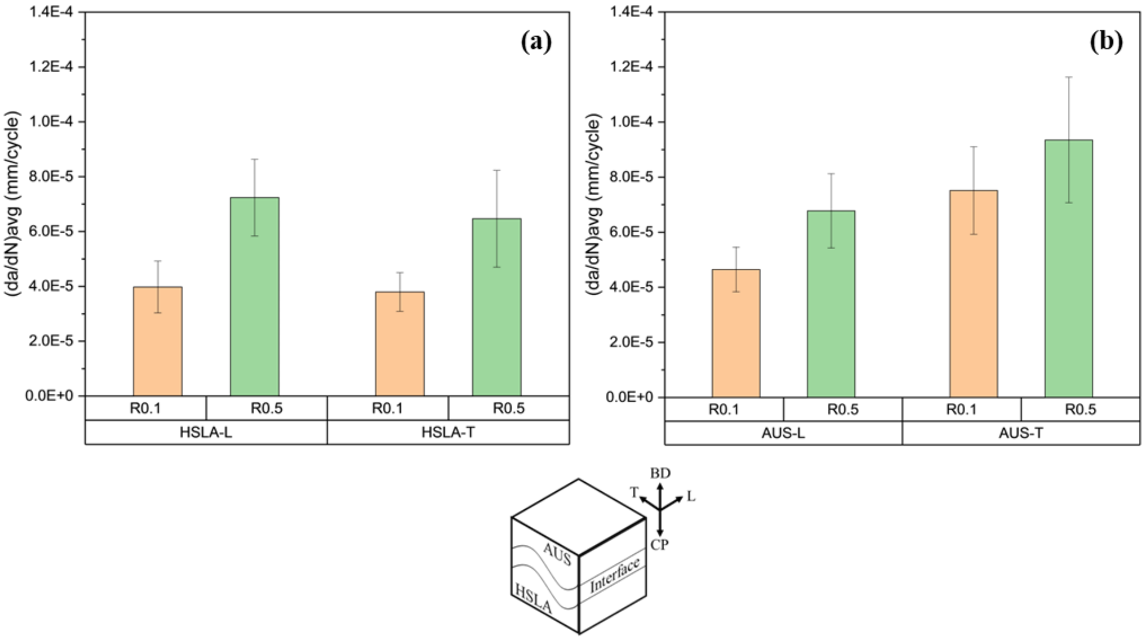

Figure 4.7 The average crack growth rate of mono-materials under constant ΔK conditions at different R ratios, where (a) is HSLA steel and (b) is AUS steel. The tests were conducted at ΔK = 20 MPa√m and a frequency of 15 Hz. Two repetitions per condition were conducted.

Table 4.5 Difference of $(da/dN)_{avg}$ in R=0.1 and R=0.5 condition for mono-materials

Materials	**Difference of (da/dN)avg in R=0.1 and R=0.5 condition (mm/cycle)**
HSLA-L	3.26E-05
HSLA-T	2.67E-05
AUS-L	2.13E-05
AUS-T	1.83E-05

The fatigue crack growth experiments on mono-material specimens provided a benchmark of the printed materials. The observations were correlated with the microstructure of the respective materials. In comparison with the literature, there were slight variations in the fatigue properties, which are most likely due to differences in the printing process. However, the benchmarked data can be utilised for comparison with the fatigue behaviour interface region. In the following sub-section, the functionally graded fatigue specimens tested under similar conditions as mono-materials will be discussed.

4.2.2. Fatigue Behaviour of Bi-materials

Constant Force Amplitude Tests

Figure 4.8 shows the Paris regime of the BM in L and T directions along with reference lines based on Paris parameters of mono-materials HSLA steel and AUS steel. The plots show a high degree of scatter, making it difficult to isolate the effects of the interface. For better clarity, the crack growth rate with respect to normalised crack length is made. The equation for normalisation is given by,

$$aNorm = a - Z(FB) \qquad 4.2$$

where aNorm is the normalised crack length, a is the instantaneous crack length, and Z(FB) is the distance of the interface. The behaviour seen at the interface region is a deceleration of crack growth rate as indicated by the yellow arrows. The deceleration effect is similar to the observations by Jiang et al. [92] as shown in Figure 2.15. The red arrows indicate sudden acceleration that could be due to defects which were observed in micrographs. This can be further verified with fractography.

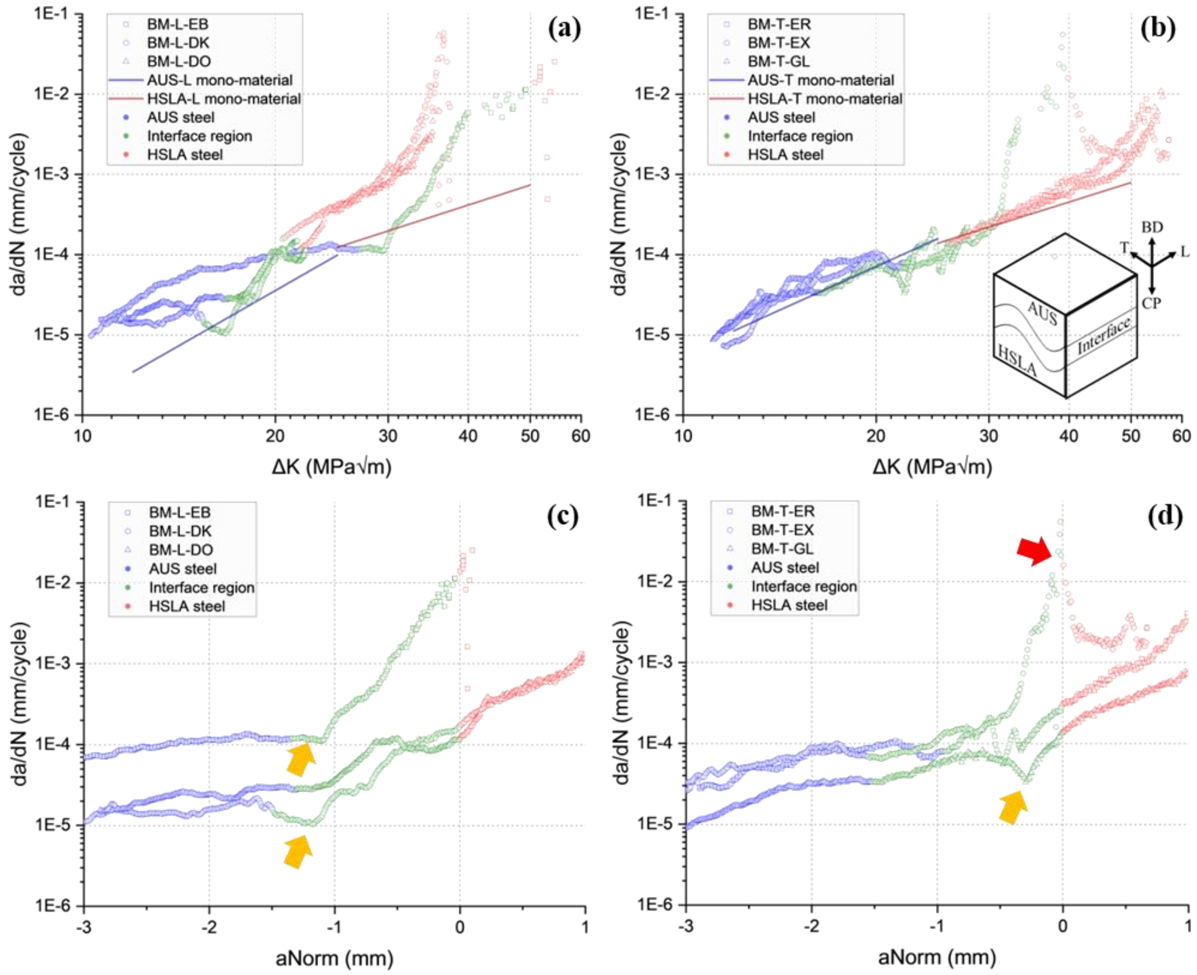

Figure 4.8 (a) and (b) The Paris regime of BM with reference lines corresponding to the mono-materials. (c) and (d) The crack growth rate normalised to the interface. The yellow arrow shows the decreasing crack growth rate despite the increasing ΔK. The red arrows show a sudden increase in crack growth rate. The tests were conducted at R = 0.1 and a frequency of 15 Hz. Three repetitions per condition are shown in this figure.

Threshold Stress Intensity Range Tests

Some changes at the interface region were also observed for constant K_{max} or decreasing ΔK tests. The FCGR graphs from ΔK_{th} tests are shown in Figure 4.9. As the location of the interface changes with each specimen, it was difficult to restrict the interface within the same ΔK levels. For better clarity, the normalised ΔK_{th} tests shown in Figure 4.10 and the changes in crack propagation rate are highlighted. The normalisation was done using equation 4.2. The purple arrow points to an accelerated crack growth. This observation is in sharp contrast to the observations in constant ΔF tests.

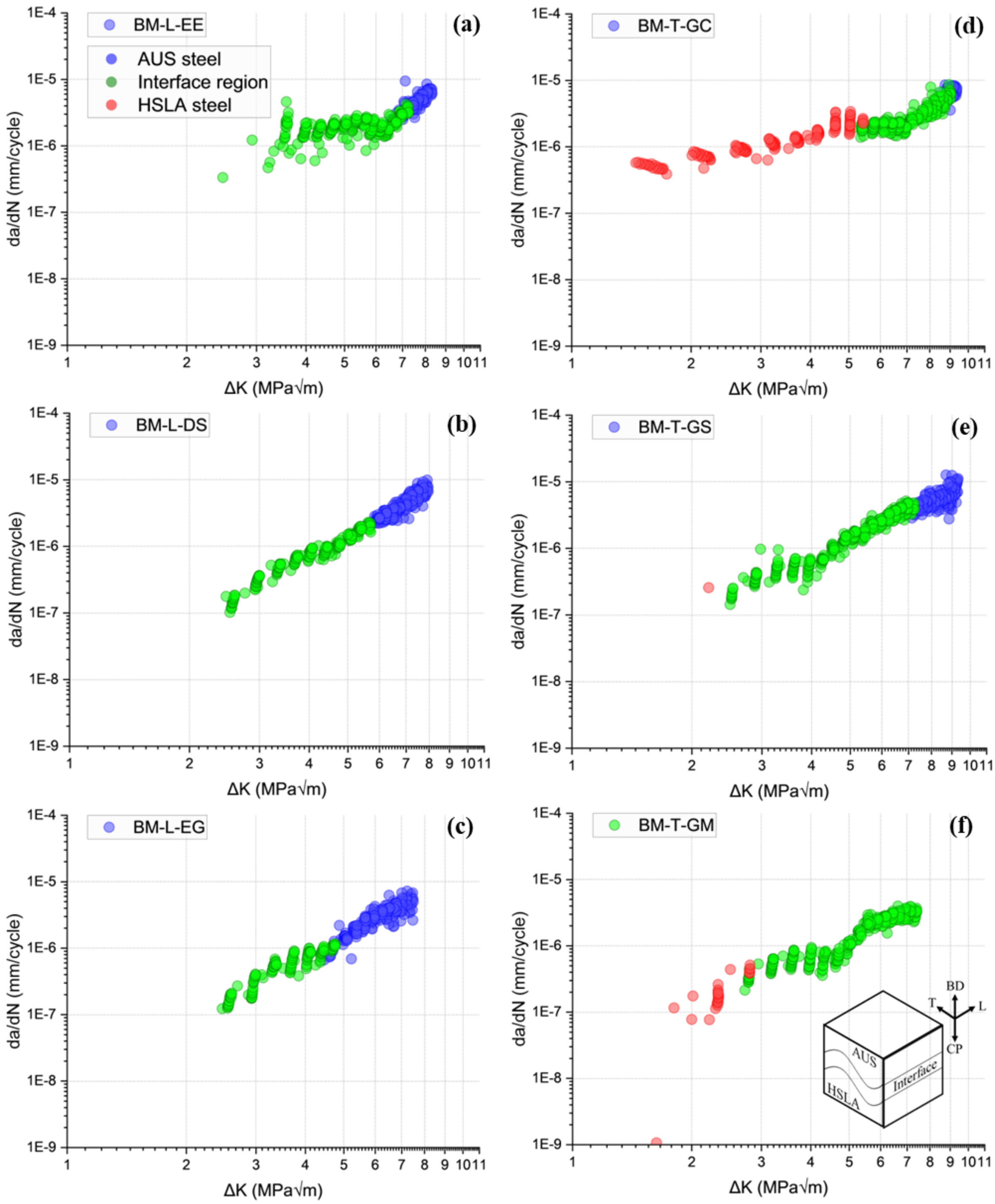

Figure 4.9 The threshold regime of BM where (a), (b) and (c) are L-oriented specimens and (d), (e) and (f) are T-oriented specimens. The graphs are shown separately for better clarity. As the position of the interface can change with the specimen, the range of ΔK and da/dN are slightly different for each test. The tests were conducted at K_{max} = 14 MPa√m, R = 0.4 to 0.9, and a frequency of 60 Hz. Individual specimens for each condition are shown in this figure.

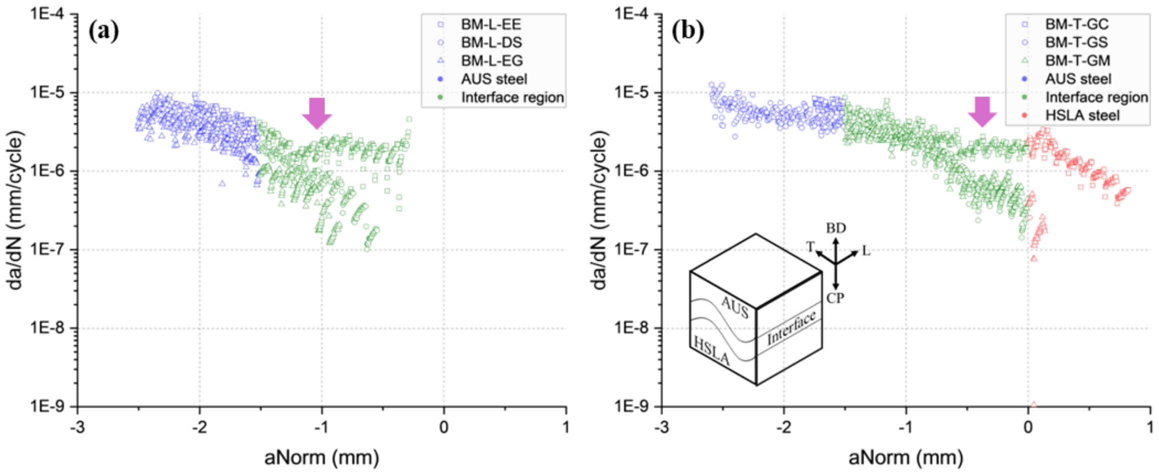

Figure 4.10 The ΔK_{th} tests normalised to crack length for (a) L-oriented and (b) T-oriented specimens. The purple arrow shows stable crack growth despite decreasing ΔK along the crack length. Three repetitions per condition are shown in this figure. The tests were conducted at Kmax = 14 MPa√m, R = 0.4 to 0.9, and a frequency of 60 Hz.

In the constant ΔF test and constant K_{max} test, the ΔK is changing with respect to the crack length. This makes it difficult to isolate all changes seen at the interface. In constant ΔF, an increasing crack growth is expected making it difficult to detect any acceleration of the crack growth rate. In contrast, in a constant K_{max} test, a decreasing crack growth is expected. Detecting any deceleration of crack growth is thus difficult. Moreover, in the ΔK_{th} tests, the R ratio is constantly increasing, which can also influence the crack growth rate. For better clarity, both ΔK and R ratios need to be constrained. This can be done with constant ΔK tests.

Constant Stress Intensity Range Tests

Figure 4.11 shows the constant ΔK tests at 20 MPa√m at R=0.1 and R=0.5. The crack length is normalized with equation 4.2. The benchmarked constant ΔK values from mono-materials are also shown. For the AUS steel part, the crack growth rate is approximately the same as in mono-materials. However, for HSLA steel, there is 3 times more scattering in the crack growth rate in comparison to the mono-material specimens. This is associated with the errors in the DCPD calibration. As the position of the interface changes with each specimen, the calibration of DCPD may be slightly different. Underestimating the crack length would result in a reduced crack growth rate. Overestimating the crack length would result in an increased crack growth rate.

Despite the scatter in the measurements, the changes observed during crack growth can still be observed. The key feature near the interface that can be noted is the deceleration of the crack growth rate in the AUS steel before the interface region. This is highlighted by the yellow arrow. Another feature that can be seen is the gradual acceleration of the crack growth throughout the interface, highlighted by the purple arrows. Additionally, the sudden acceleration of the crack growth rate is highlighted by the red arrows. For better visibility of the sudden acceleration, the low-scale graphs of the constant ΔK tests are shown in Appendix 7.5. The values of the changes in crack growth rate are noted in Table 4.6. The change during deceleration under all conditions is similar. However, for gradual acceleration, the value for L-orientation is 2 times higher than that in T-orientation. The sudden acceleration, which is only observed for T-orientation, is 2 times higher for R=0.1 and 5 times higher for R=0.5. The accelerations can be detrimental during application. To verify if the FEM-based K-solution had any effects on the behaviour seen at the interface, a constant ΔK test was done without the use of the correction factor. This is shown in Appendix 7.5.

As discussed in section 4.2.1, a microstructural feature that may be resisting crack propagation is the grain boundaries. AUS steels have large austenite grains. These grains are mostly oriented along the build direction, which is parallel to the crack propagation direction. This results in lesser grain boundaries to resist crack growth. However, within the interface, there are both FCC and BCC grains. This results in more grain boundaries as shown by Galán Argumedo et al. [20]. Hence, there are more crack-resisting features in the interface. Additionally, an increased crack closure effect could also play a role in the deceleration as seen in the study by Pippan et al. [95], [96] discussed in section 2.4.

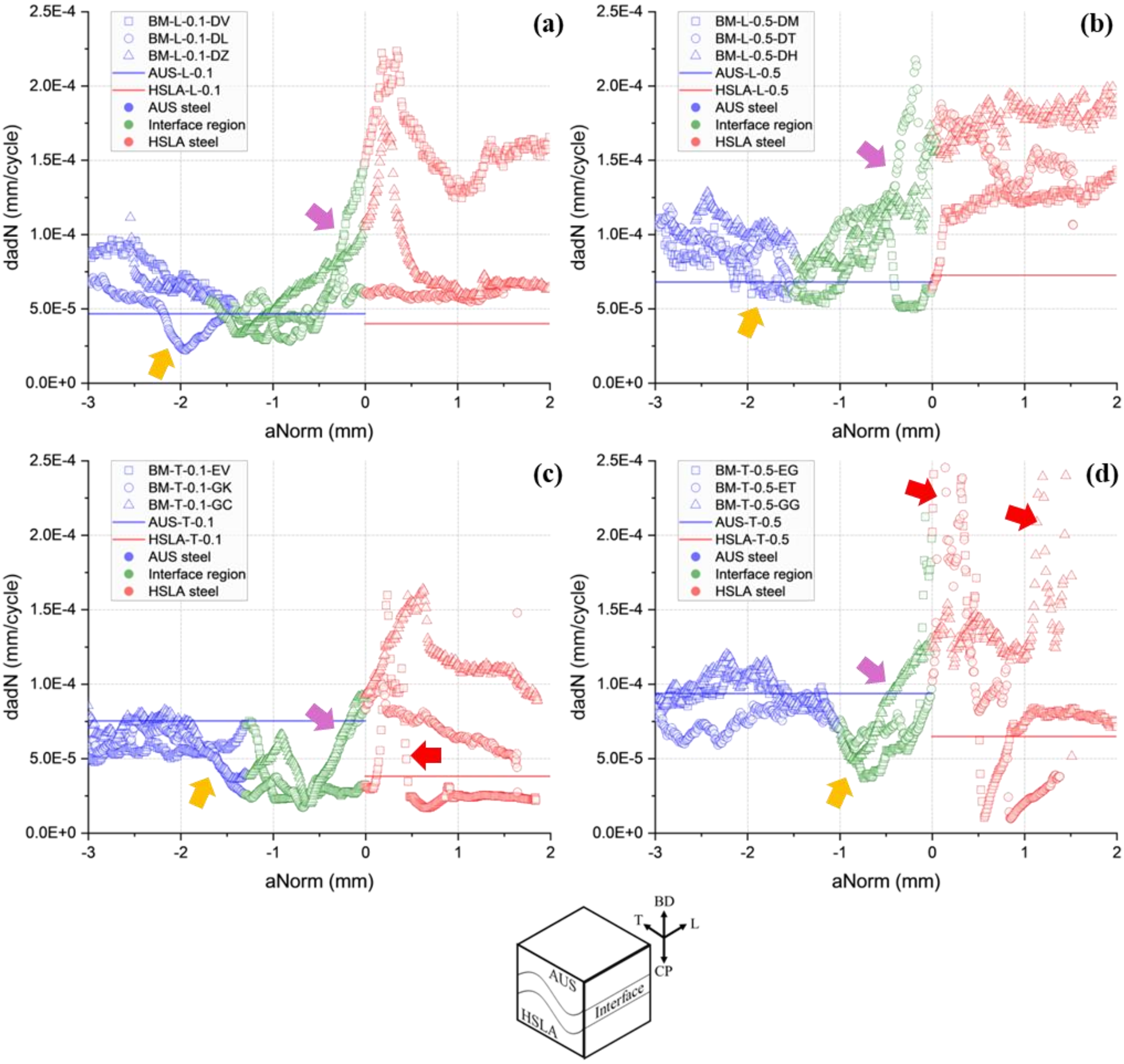

Figure 4.11 The constant ΔK tests with normalised crack length. (a) and (b) are L-oriented specimens, and (c) and (d) are T-oriented specimens. (a) and (c) are under R=0.1, and (b) and (d) and under R=0.5. The reference lines of constant ΔK tests of mono-materials are shown as

well. The tests were conducted at ΔK = 20 MPa√m and a frequency of 15 Hz. Three repetitions per condition are shown in this figure.

Table 4.6 The average values of the change in crack growth rate observed for each condition in constant ΔK experiment in BM.

Material	**Change during deceleration (mm/cycle)**	**Change during gradual acceleration (mm/cycle)**	**Change during sudden acceleration (mm/cycle)**
BM-L-0.1	6.10E-05	1.32E-04	-
BM-L-0.5	5.77E-05	1.05E-04	-
BM-T-0.1	5.73E-05	5.50E-05	1.21E-04
BM-T-0.5	5.13E-05	6.10E-05	3.20E-04

In the FEM analysis of the present study, the CMOD (or CTOD) results show a similar pattern. In Figure 4.12 the results of FEM analysis on the CMOD ratio of the BM to mono-material is shown. Upon calculating the CMOD as a function of the position of the BM interface, it can be seen that the CMOD ratio tends to decrease while approaching the interface. This trend of decreasing CMOD is similar to the study by Pippan et al. [95], [96]. However, for conclusive evidence, an experimental study on the change in CTOD or CMOD values during fatigue crack growth must be done in a future study.

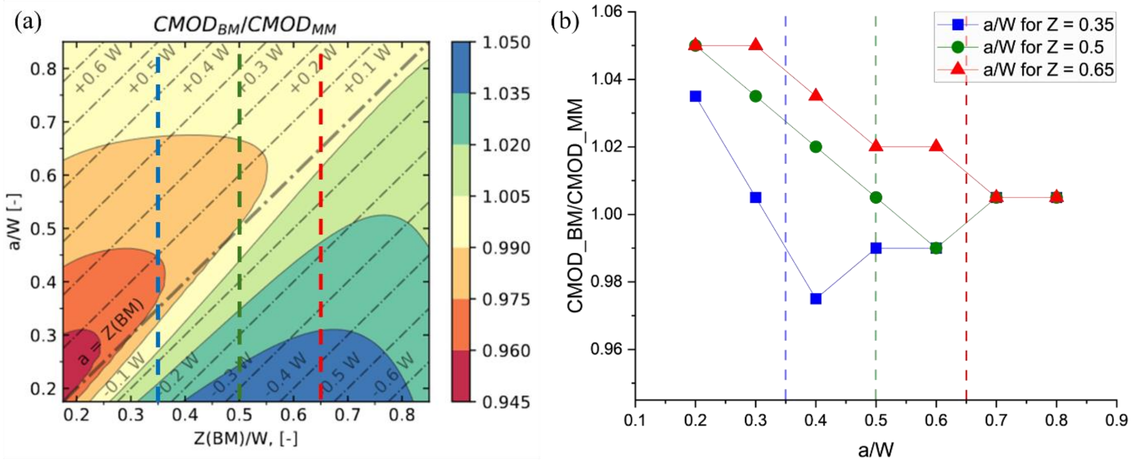

Figure 4.12 (a) The ratio of CMOD of BM to MM. Three interface distances are considered for calculation. (b) The change in CMOD ratio with respect to the instantaneous crack. The dotted line in both figures shows the interface distances.

The explanations for the deceleration of the crack growth rate are not coherent with the gradual acceleration of the crack growth rate seen in the interface. If the logic of increasing grain boundaries is to be followed, then the transition from a combination of FCC and BCC grains to fully BCC grains should have resulted in further deceleration. Additionally, if the reasoning for the increase in crack closure effects is followed, then also the crack should have decelerated at the FB. In contrast, the observed effect is a gradual acceleration of the crack propagation. Apart from the gradual acceleration, there is also some sudden acceleration present in the HSLA steel. This can be observed in both constant amplitude as well as constant ΔK tests. It can also be noted that the sudden acceleration is present only for T-oriented specimens. These are likely due to pores present in HSLA steel which was observed in the micrographs. These observations can be validated with fractographs.

4.3. Crack Path Behaviour

4.3.1. Fractographic Analysis

Fractography of mono-material specimens and BM specimens were done to confirm the presence and nature of the defects and to identify differences in fracture surface between the different materials. Figure 4.13 shows the typical fracture surfaces of constant ΔF tests of mono-materials and BM specimens in both orientations. The remaining fractographs are shown in Appendix 7.6. The AUS steel displays a rougher surface compared to HSLA steel. This could be due to the larger grain size and ductility of AUS steels. At lower load ratios, coarse grains are increasingly influenced by roughness-induced crack closure in comparison to fine grains. The finer-grained microstructure is known to have lower crack tortuosity and roughness-induced crack closure which can lead to straighter crack flanks [34]. This is reflected in the fractographs as well as the surface crack path during experiments, as shown in Figure 4.14.

For HSLA steel specimens, the porous defects are pointed out by red arrows in Figure 4.13. The defects are aligned in the L direction. For AUS steel, no such porous defects were found. The L-oriented pores are also observed in BM specimens. The influence of these defects during the experiment is seen in the form of a sudden acceleration of the crack growth rate. Figure 4.15 highlights this for a constant ΔK experiment. The location of the defect in the fractograph matches the distance at which the spike is observed. Only T-oriented specimens are affected by these pores. For L-oriented specimens, the effects of pores are not significant as the pore runs along into the plane of the cross-section.

Figure 4.16 shows the fractographs of ΔK_{th} tests of FGM in both orientations. The distinction of fracture surface between AUS steel and interface was more difficult in this experiment. Hence, for threshold analysis, an average length of 1.5mm was considered for the length of the interface. The difficulty in distinction may be due to higher stress ratios of 0.5 to 0.8-0.9 during the ΔK_{th} experiments. At these stress ratios, the crack closure effects of the AUS steel are lesser which results in smaller topographic features on the fracture surface of AUS steel. In other tests, due to lower stress ratios, the surfaces of AUS steel have larger topographic features making it easier to distinguish from the interface.

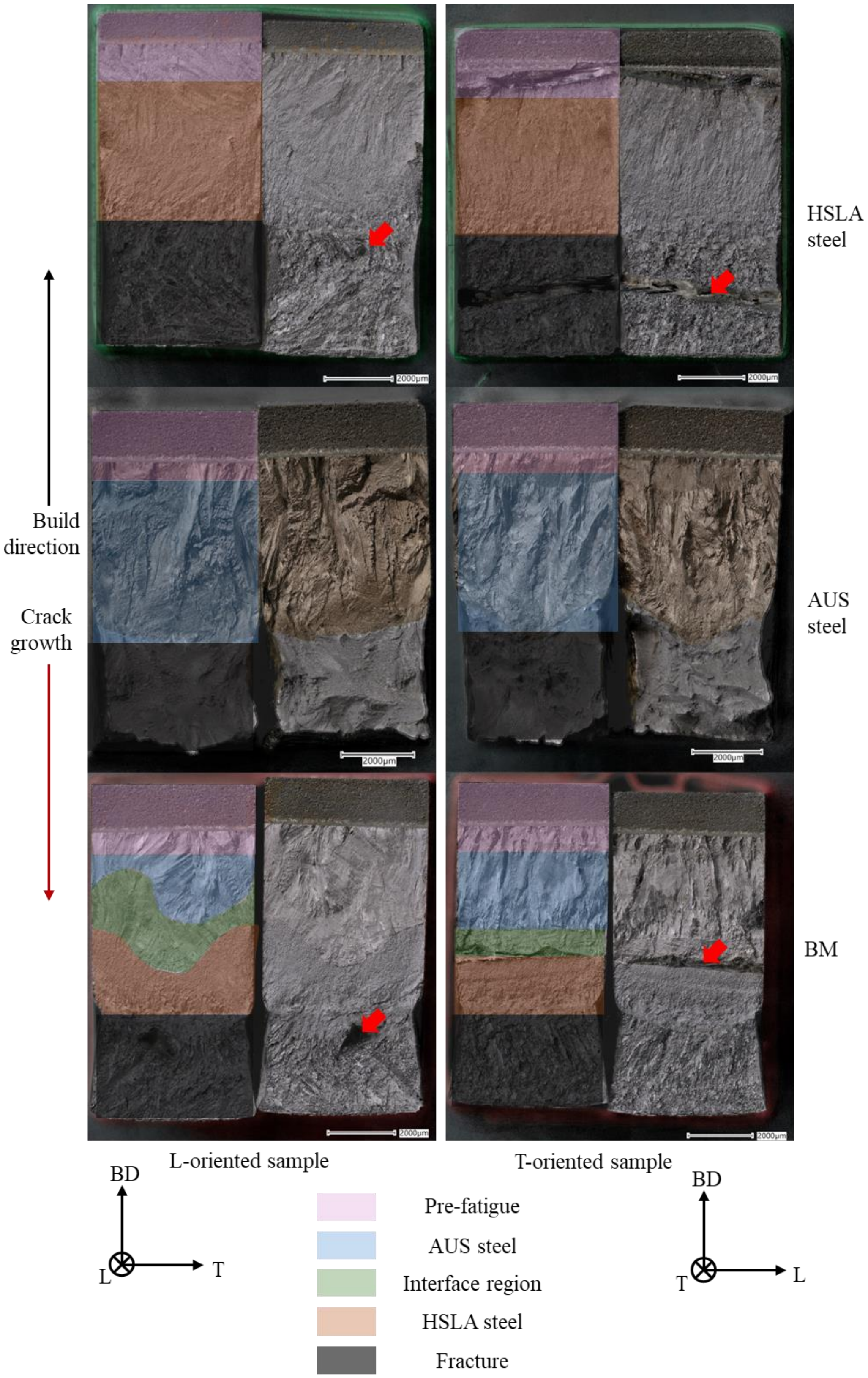

Figure 4.13 The typical fractographs of constant ΔF tests of mono-materials HSLA steel and AUS steel, and the FGM or BM, under two orientations. The regions of pre-fatigue and fracture are highlighted, as well as each material through which the crack passed. The coordinates and directions are also shown. The red arrows show the tracks created by lack of fusion. The scales shown in all images are 2000 μm.

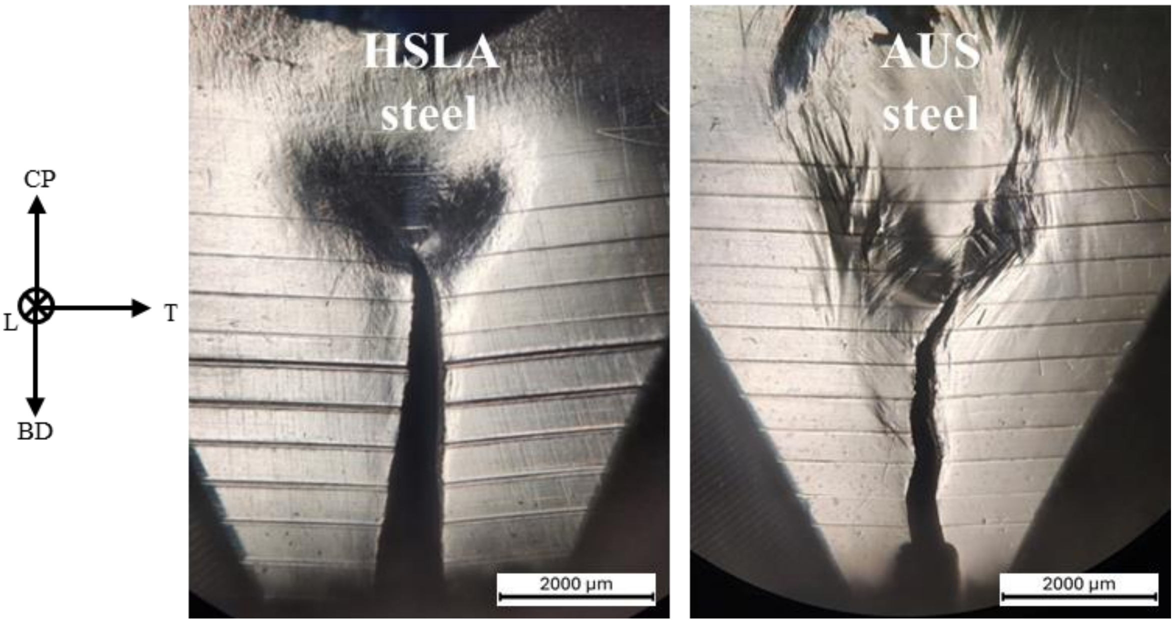

Figure 4.14 The typical crack path during constant ΔF tests of mono-materials. HSLA steel has straighter crack path compared to AUS steel. The coordinates and directions are also shown.

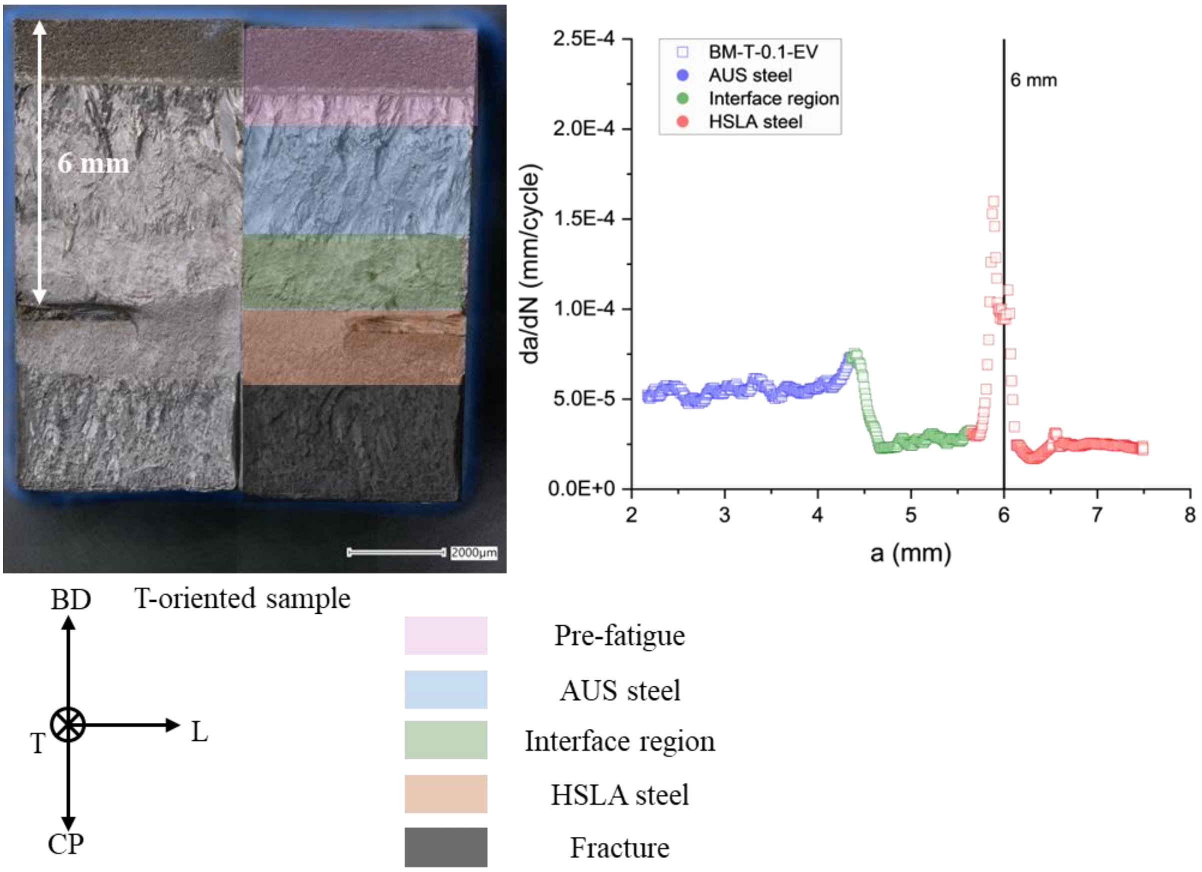

Figure 4.15 The location of the pore in the fractographs and the corresponding FCGR curve for the specimen. The regions of pre-fatigue and fracture are highlighted, as well as each material through which the crack passed. The coordinates and directions are also shown.

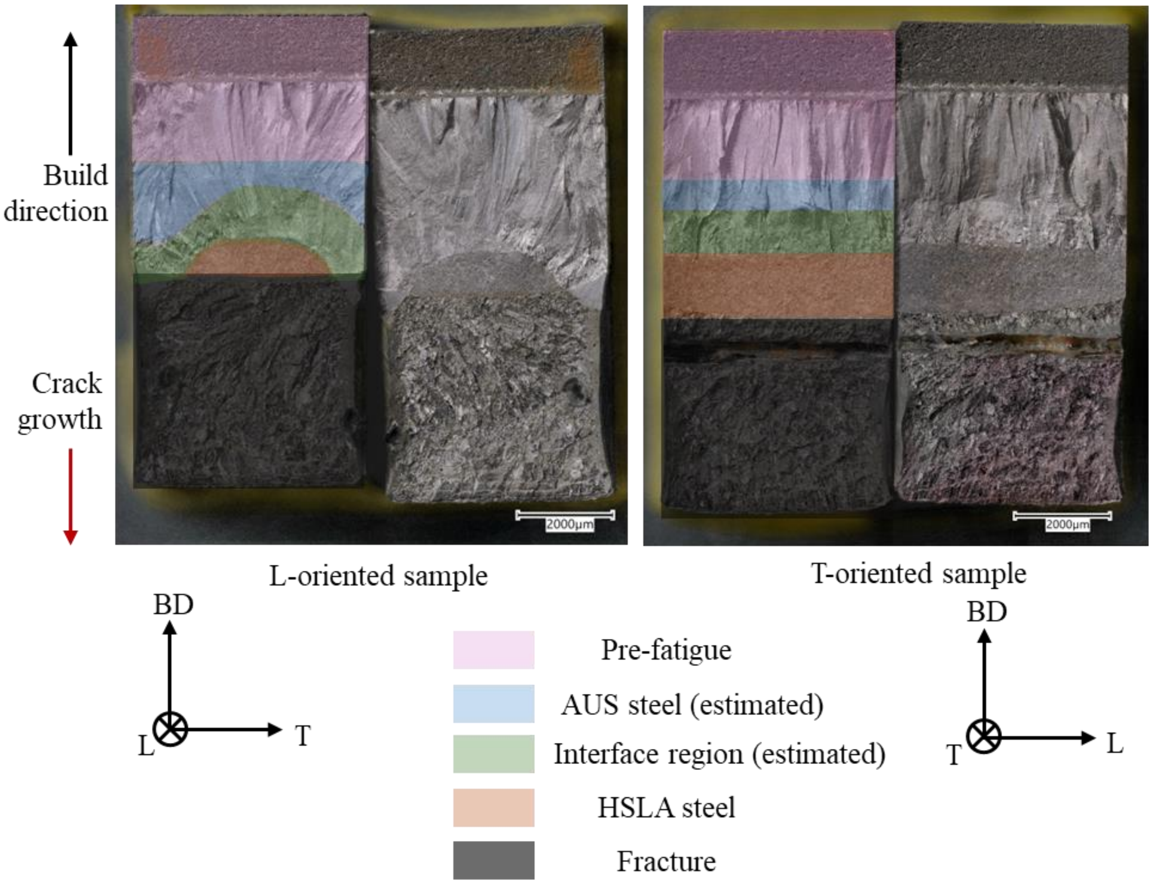

Figure 4.16 The typical fractography of ΔK_{th} tests of the BM, under two orientations. The regions of pre-fatigue and fracture are highlighted, as well as each material through which the crack passed. The coordinates and directions are also shown.

Due to controlled parameters in testing, fractographs from constant ΔK may be better for comparing the fracture surface topography of AUS steel and HSLA steel with the interface region. Figure 4.17 shows the fractographs for a typical constant ΔK experiment under each R ratio. The remaining fractographs are shown in Appendix 7.6. The roughness of the interface appears to be closer to HSLA steel except for the colour. The fracture surface of the interface is smoother than AUS steel. This could be due to the differences in the grain sizes. As explained earlier, larger grains can result in larger topographic features. As the interface is a mix of both FCC and BCC grains, it might explain the less roughness. This further supports the possibility of reduced crack closure effects at the interface which could have led to crack growth acceleration. For further investigations, the fatigue specimens were studied under SEM.

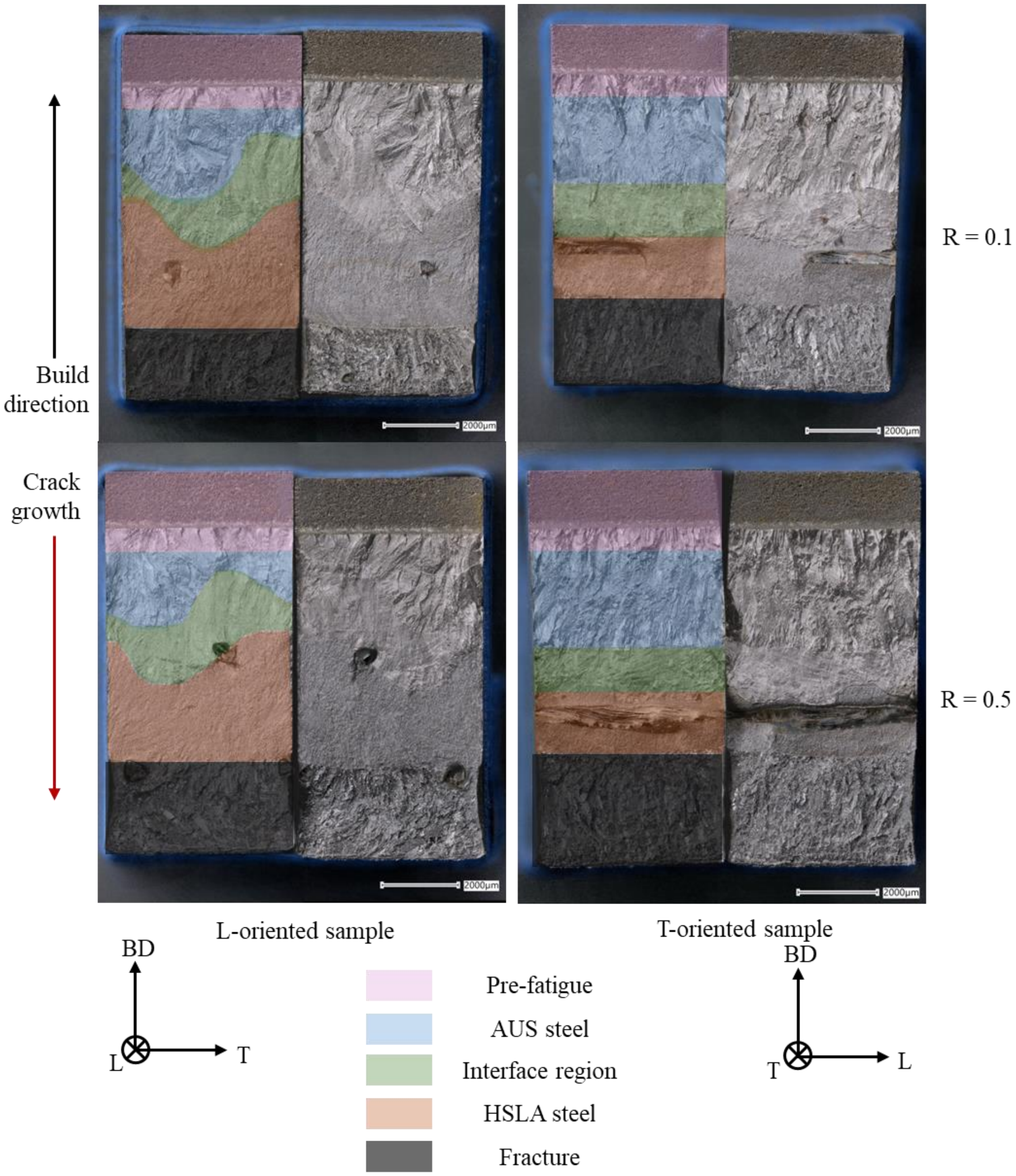

Figure 4.17 The typical fractographs of constant ΔK tests of the BM, under two orientations and two R ratios. The regions of pre-fatigue and fracture are highlighted, as well as each material through which the crack passed. The coordinates and directions are also shown.

The SEM analysis showed striations, ridges, and secondary cracks. Striations were visible for higher stress intensity ranges in constant ΔF tests. Figure 4.18 shows the striations observed in the fractographs and the comparison with the data from the FCGR tests. A difference of 6.32E-04 mm/cycle can noted. The difference in the measurements is due to the errors associated with the DCPD calibration. For AUS steels, ridges are visible as shown in Figure 4.19. Secondary cracking can also be observed in AUS steel near the interface region. Huang et al. [79] reasoned a dissipation of energy by secondary cracks in their study of fatigue crack growth behaviour of WAAMed ER70S-6. Hence, secondary cracks could also be the cause for the reduction of the crack growth rate before the interface region.

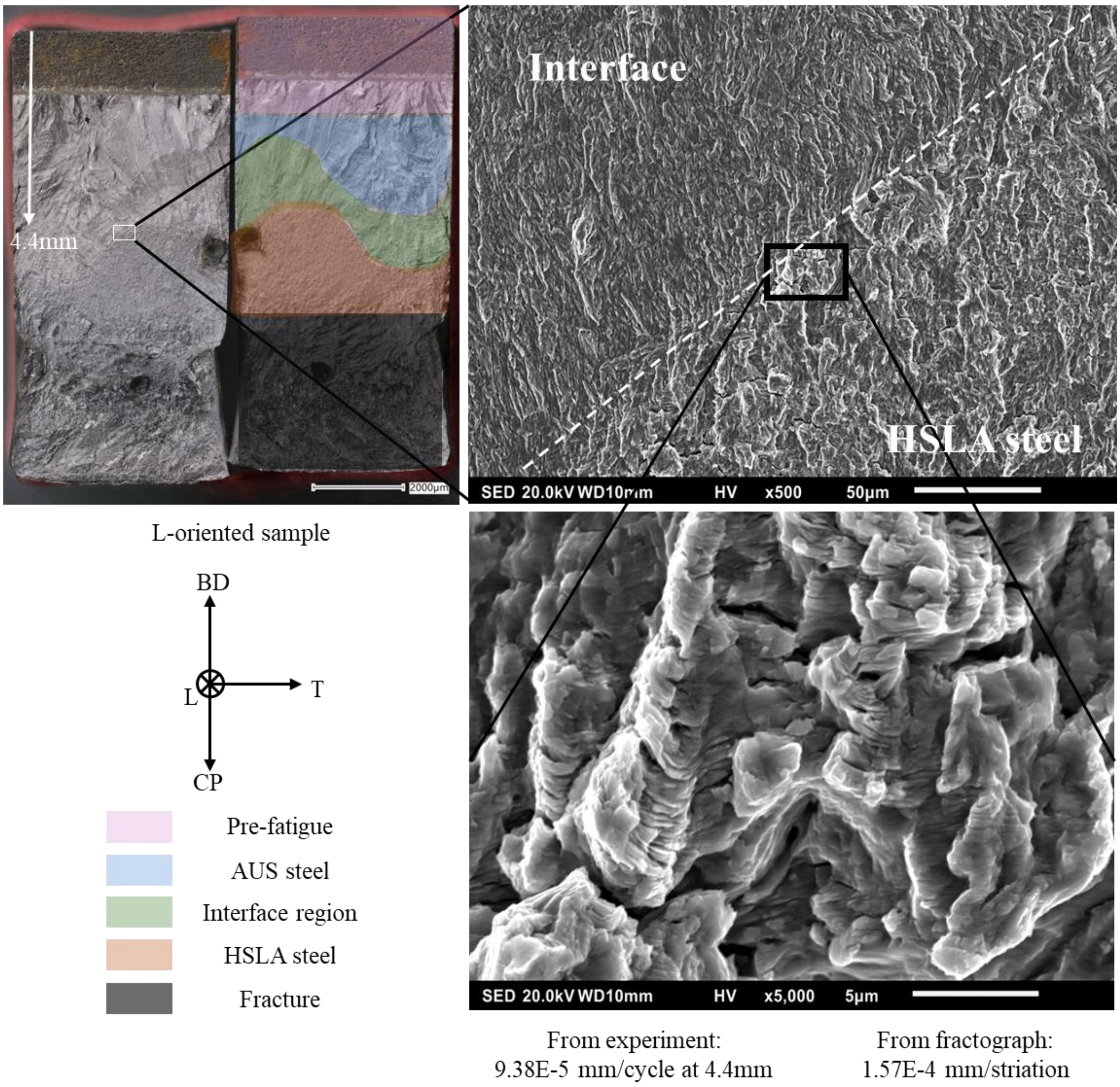

From experiment:
9.38E-5 mm/cycle at 4.4mm

From fractograph:
1.57E-4 mm/striation

Figure 4.18 The striations observed for a BM under constant ΔF condition. The average striation spacing is shown for the highlighted region. The experimental result for the same region is shown. The coordinates and directions are also shown.

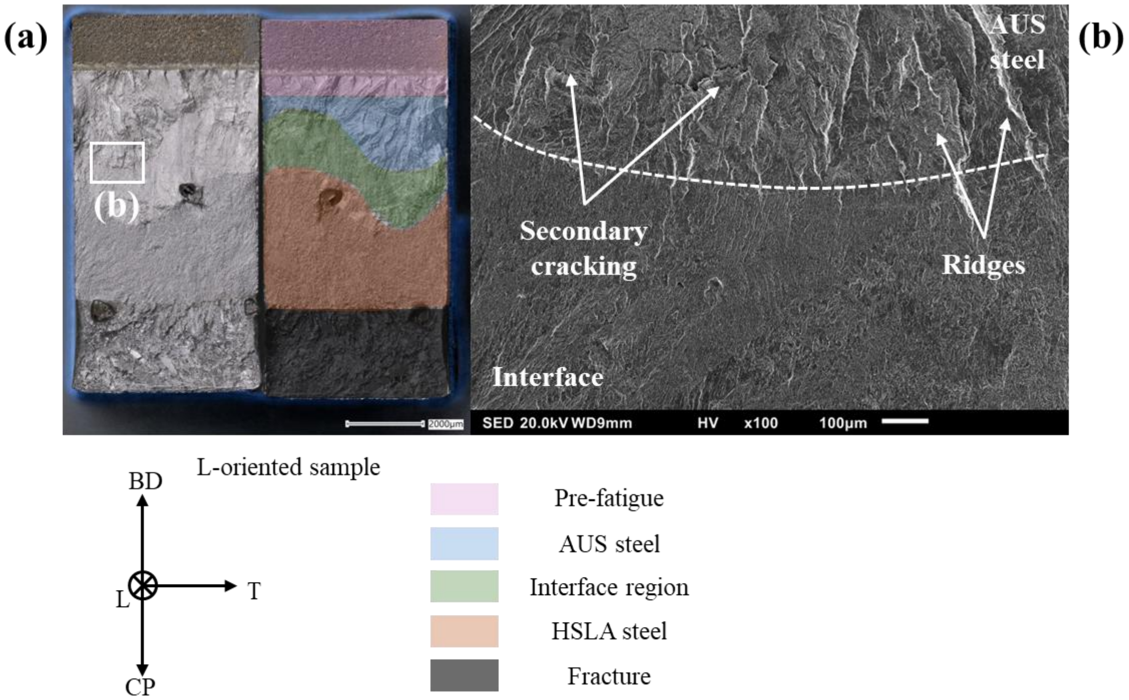

Figure 4.19 The fractography of BM near the AUS steel and interface boundary. Ridges and secondary cracking can be seen in the AUS steel. The regions of pre-fatigue and fracture are highlighted, as well as each material through which the crack passed. The coordinates and directions are also shown.

The cause for the acceleration of the crack propagation rate is understood to lie within the interface region. A brittle region near the FB can be observed as shown in Figure 4.20(a). These could be related to the martensite observed in micrographs (Figure 4.2) and also reported by [20]. Figure 4.20(a) shows the ductile and brittle region near the FB next to a pore. The formation of undeformed dimples may have been a consequence of the pore ahead of the crack tip. This phenomenon is shown in Figure 4.20(b). When the crack approaches the pore, the crack growth rate accelerates resulting in dimples in the ductile region and cleavage fracture in the brittle region. Due to the pore, crack closure may have also been prevented which explains the undeformed dimples. Some brittle regions were also observed within the interface, as shown in Figure 4.21(b). These brittle regions may be related to the martensite islands seen in micrographs (Figure 4.2) and also reported in the literature [20]. A larger area of interface results in increased presence of martensite and could lead to more crack growth rate. To verify this, the area of the interface for each orientation is noted in Table 4.7. A 33% larger area of L-orientation compared to T-orientation resulted in 2 times higher acceleration as shown in Table 4.6.

Table 4.7 The are of the interface for each orientation.

Orientation	Area of interface (mm^2)
Longitudinal	7.6±0.4
Transverse	5.7±0.6

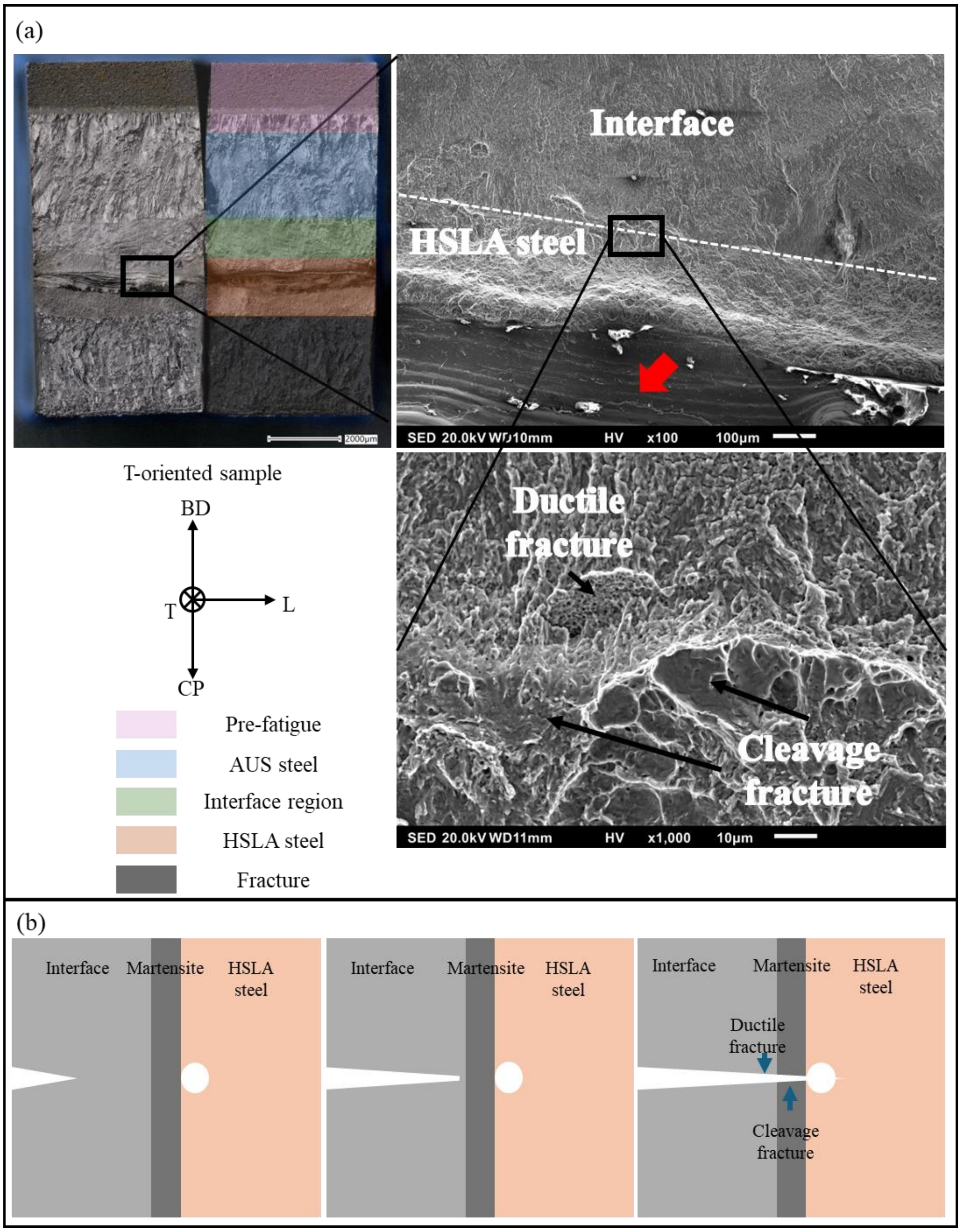

Figure 4.20 (a) The ductile and brittle failures near the fusion boundary of HSLA steel. The red arrow shows the pore in the HSLA steel. (b) The formation of the ductile and brittle fracture in the presence of a pore. Due to the pore, undeformed dimples and cleavage fractures are formed.

Under SEM it can also be seen that interface has lower topographic features than the HSLA steel, as highlighted in Figure 4.22. This may further suggest that the interface has lesser crack closure effects than either of the mono-materials. The brittle regions in the interface and the FB combined with the low crack closure effects of the interface region may explain the gradual acceleration of the crack propagation rate observed before the FB. The topography is related to the deformation of the crack flanks. To investigate the deformation mechanism around the crack flanks, EBSD analysis is required.

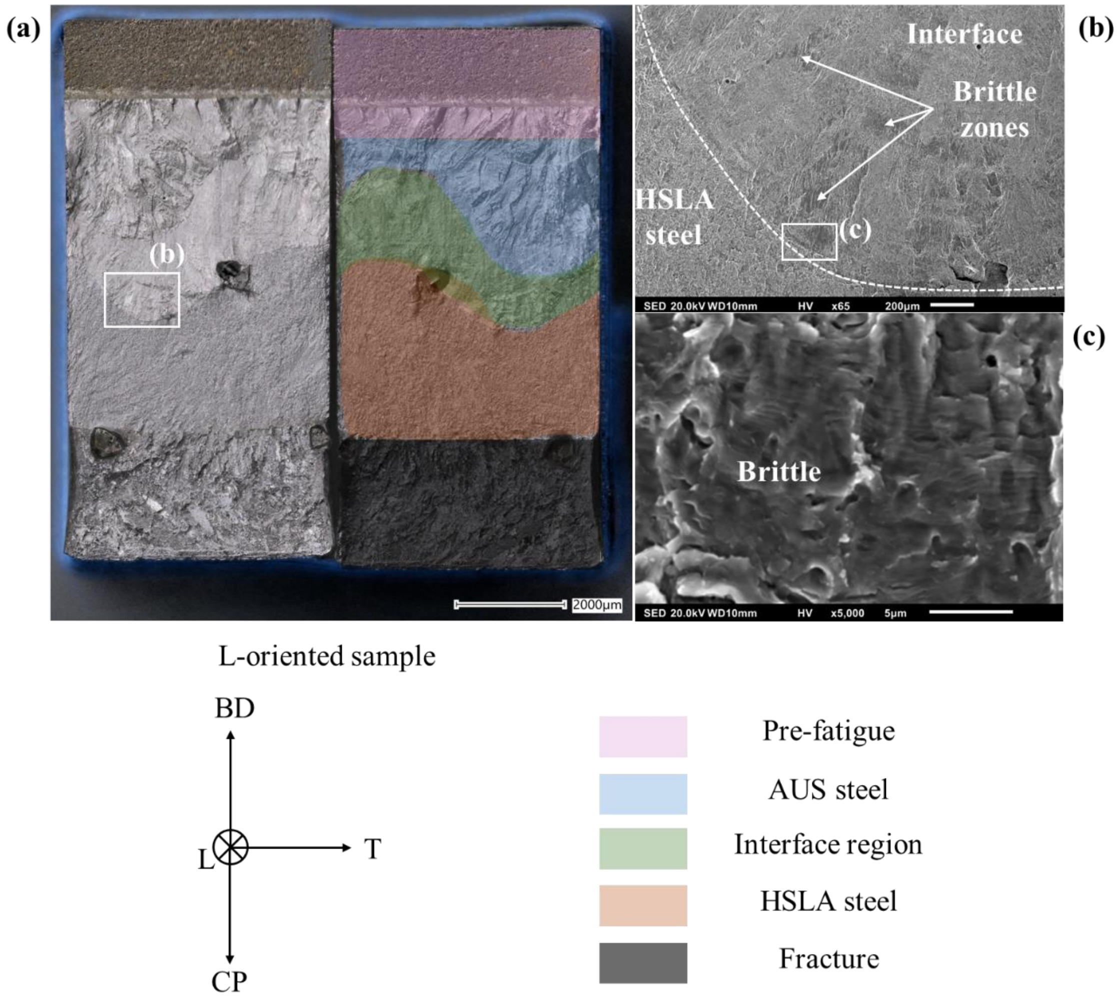

Figure 4.21 (a) Fractography of a constant ΔK test L-oriented specimen. (b) Interface region near to fusion boundary of HSLA steel. The brittle zones scattered in the interface are highlighted. The scale is 200 µm (c) A brittle region in the interface is highlighted. The scale is 5 µm. The regions of pre-fatigue and fracture are highlighted, as well as each material through which the crack passed. The coordinates and directions are also shown.

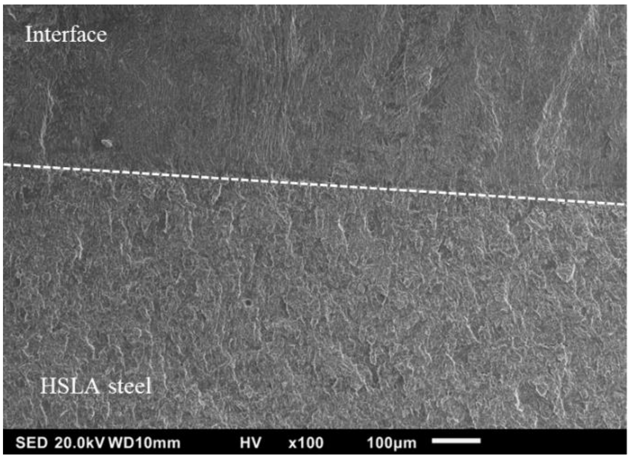

Figure 4.22 The comparison of interface and HSLA steel fracture surface. The interface appears to be less rough compared to HSLA steel.

4.3.2. EBSD Analysis

The EBSD analysis of the crack path was done on the specimens used for constant ΔK experiment specimens. Under a constant ΔK and R ratio, the plastic zone would depend on the local yield strength which is dependent on the local microstructure ahead of the crack tip. Additionally, the number of variables to be studied can also be controlled. The area close to the crack flanks was studied with a focus on three regions, 1) the FB of interface and HSLA steel, 2) the FB of AUS steel and interface, and 3) regions within the interface. These mapping were done for the surface of the specimens. For specimens with larger plasticity effects, which are tested under a higher R ratio, the middle sections of the specimens were also studied. The middle section of the specimens would undergo plane strain condition and the surface would undergo plane stress condition during deformation. Specimens of both orientations were included in the analysis. In this section, the EBSD maps of five specimens are shown: undeformed specimen, DL – L-oriented specimen tested under R=0.1, DT – L-oriented specimen tested under R=0.5, DT middle section – L-oriented specimen tested under R=0.5, GG middle section – T-oriented specimen tested under R=0.5.

Figure 4.23 shows the EBSD map of an undeformed area close to the FB of HSLA steel. The features to be noted are the low-quality regions highlighted by white arrow and blue arrow. Low image quality can be an indication of martensite phases [103]. However, it is not an absolute quantity and can change with respect to different maps. The region indicated by the white arrow may be similar to the martensite islands observed in Figure 4.2 (d). The blue arrow may indicate the martensite layer which may have also resulted in the brittle fracture seen in Figure 4.20. The BCC phases appear to follow Nishiyama-Wasserman (N-W) orientation relation with the surrounding FCC grains. These observations are consistent with the literature [20].

Figure 4.24 shows the EBSD map of the surface of the DT specimen, tested under a constant ΔK and R ratio of 0.1. The white and blue arrows show similar features to the undeformed specimen. A low-quality region surrounding the crack flanks can also be observed. The crack flanks also appear to be BCC phase. To investigate further, three close-up maps were taken from the regions marked as 1, 2 and 3. Figure 4.25 shows region 1, where the BCC phase is formed along the crack flanks even across a band of FCC phase. This may suggest that the FCC phase was transformed to BCC due to deformation. This phenomenon is likely to be transformation-induced plasticity (TRIP) effect reported in the literature for metastable austenitic stainless steels (MASS) [104]. TRIP effect can also result in the absorption of some of the deformation through a transformation from FCC to BCC before crack extension. However, it must be noted that TRIP can also be caused by the nature of polishing [105].

The crack flanks are surrounded by BCC throughout the interface as shown in Figure 4.26 for region 2 and Figure 4.27 and region 3. Region 3 in this case has a mix of martensite and ferrite. To distinguish these phases, the aspect ratio and grain average misorientation were plotted with respect to the image quality as shown in Figure 4.28 (a) and (b). No clear trend was observed in this case. A map of region 3 with low image quality of less than 60,000 was plotted. The value of image quality is not absolute and can vary between specimens and polishing conditions. However, estimation of 60,000 was chosen in this analysis based on the trends seen for low image quality of martensite. Further verification with hardness measurements in regions 1 and 3 were done as shown in Figure 4.29. The hardness of ferrite in HSLA steel is lower than the martensite present above the FB. In region 2, there is no significant change in hardness away from the flanks for AUS steel. However, within the interface, the hardness values closer to the crack flanks are 26% higher than away from the flanks. This further supports the possibility of TRIP within the interface.

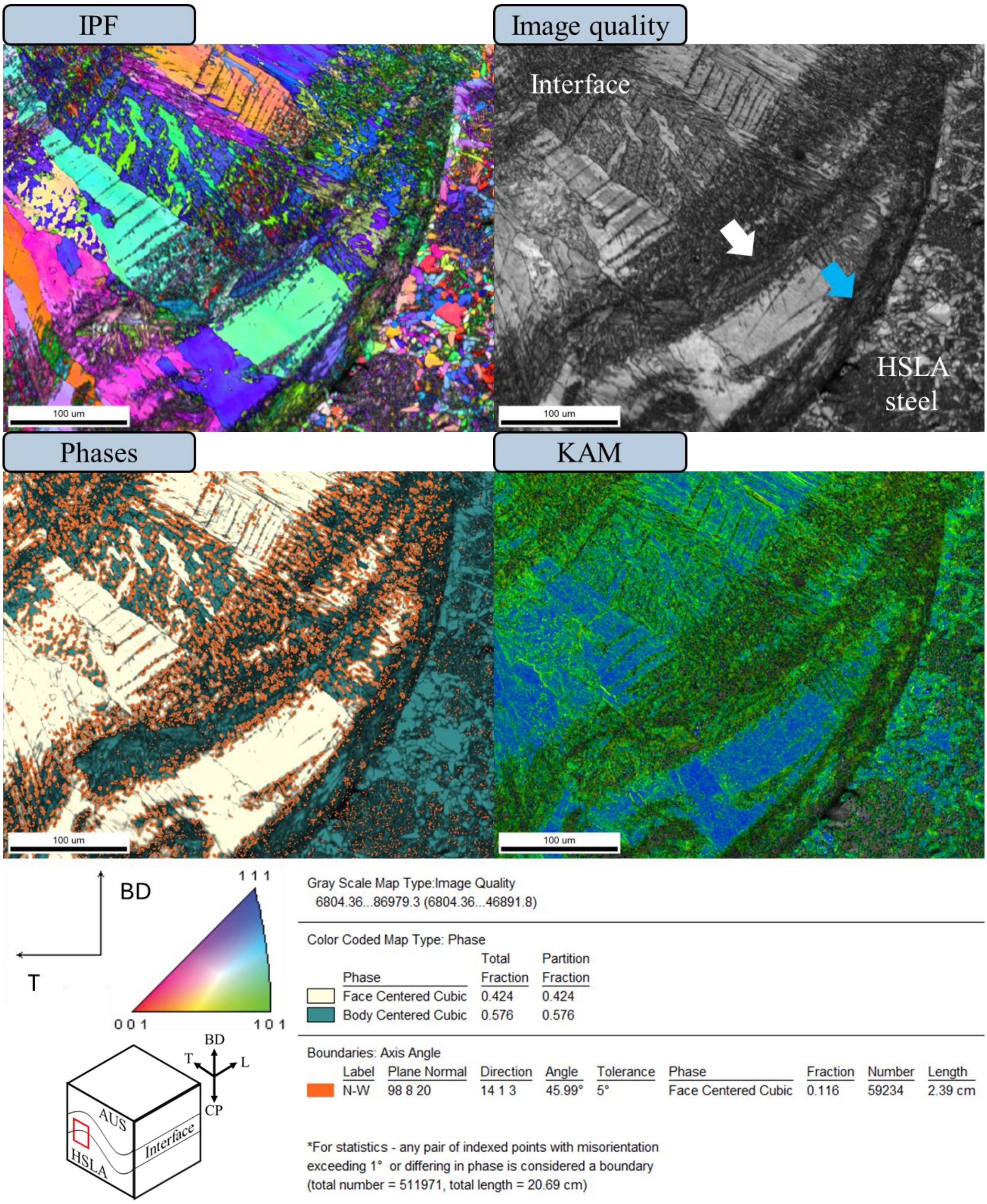

Gray Scale Map Type:Image Quality
6804.36...86979.3 (6804.36...46891.8)

Color Coded Map Type: Phase

	Phase	Total Fraction	Partition Fraction
☐	Face Centered Cubic	0.424	0.424
■	Body Centered Cubic	0.576	0.576

Boundaries: Axis Angle

	Label	Plane Normal	Direction	Angle	Tolerance	Phase	Fraction	Number	Length
■	N-W	98 8 20	14 1 3	45.99°	5°	Face Centered Cubic	0.116	59234	2.39 cm

*For statistics - any pair of indexed points with misorientation exceeding 1° or differing in phase is considered a boundary (total number = 511971, total length = 20.69 cm)

Figure 4.23 The EBSD map of undeformed region. The white arrow points to the low image quality region in the interface. The blue arrow points to the low image quality region at the fusion boundary. Step size of 0.1 µm was used for scanning.

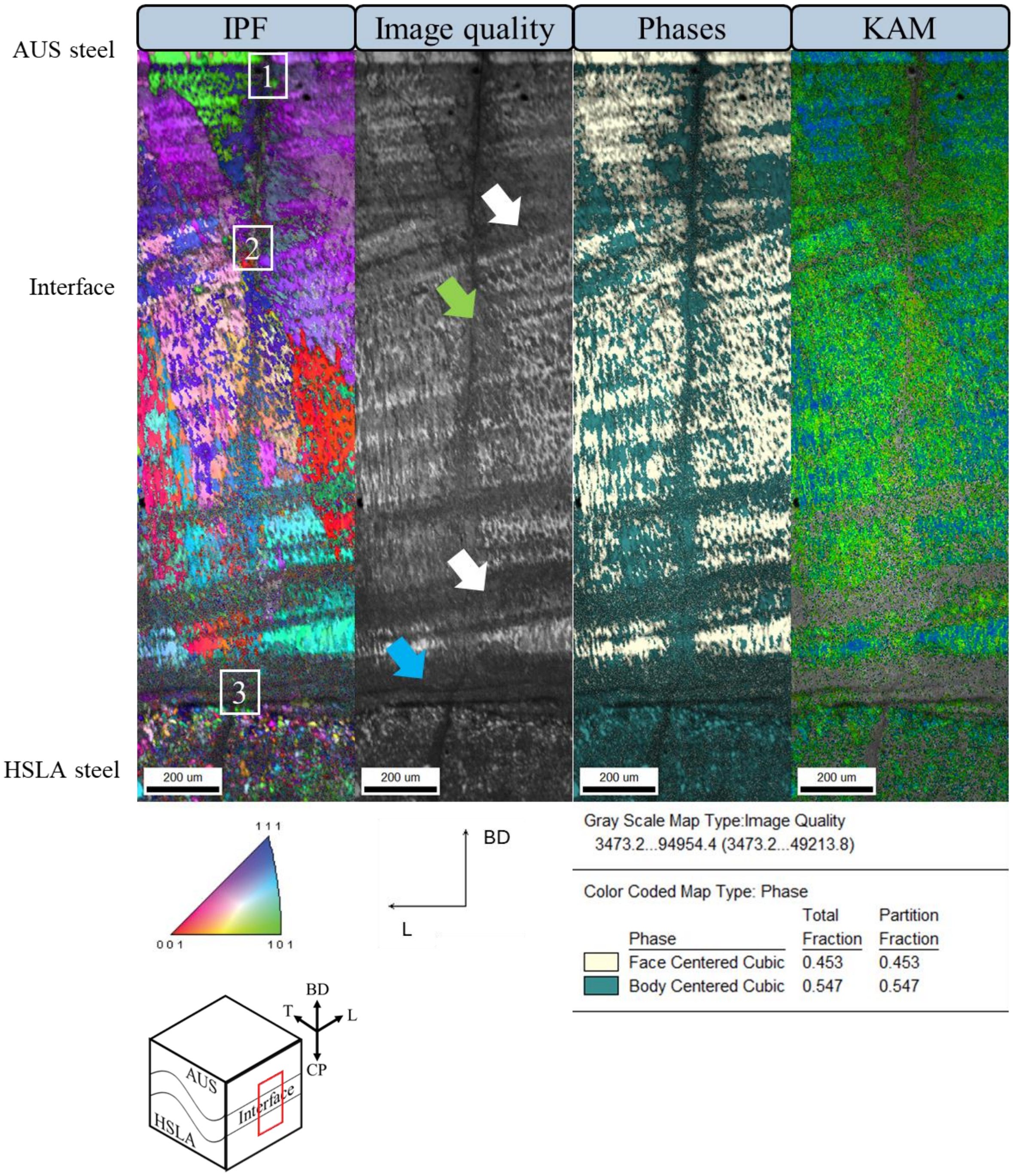

Figure 4.24 The surface EBSD map of an L-oriented specimen tested under constant ΔK at a load ratio of 0.1, labelled as DL. The white arrow points to the low image quality region in the interface. The blue arrow points to the low image quality region at the fusion boundary. The green arrow points to the low image quality region around the crack flanks. Regions 1, 2 and 3 are marked. Step size of 1.5 μm was used for scanning.

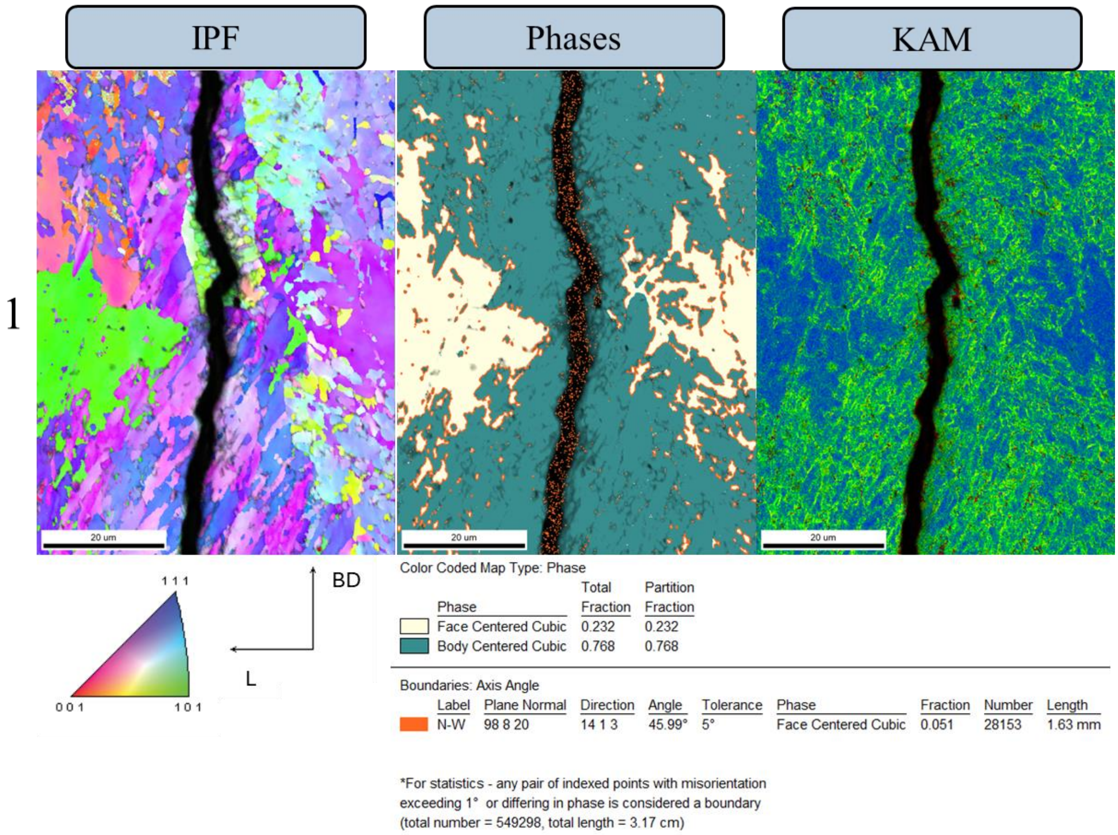

Color Coded Map Type: Phase

	Phase	Total Fraction	Partition Fraction
☐	Face Centered Cubic	0.232	0.232
■	Body Centered Cubic	0.768	0.768

Boundaries: Axis Angle

	Label	Plane Normal	Direction	Angle	Tolerance	Phase	Fraction	Number	Length
■	N-W	98 8 20	14 1 3	45.99°	5°	Face Centered Cubic	0.051	28153	1.63 mm

*For statistics - any pair of indexed points with misorientation exceeding 1° or differing in phase is considered a boundary (total number = 549298, total length = 3.17 cm)

Figure 4.25 The surface EBSD map of region 1 of specimen DL, as shown in Figure 4.24. Step size of 0.1 μm was used for scanning.

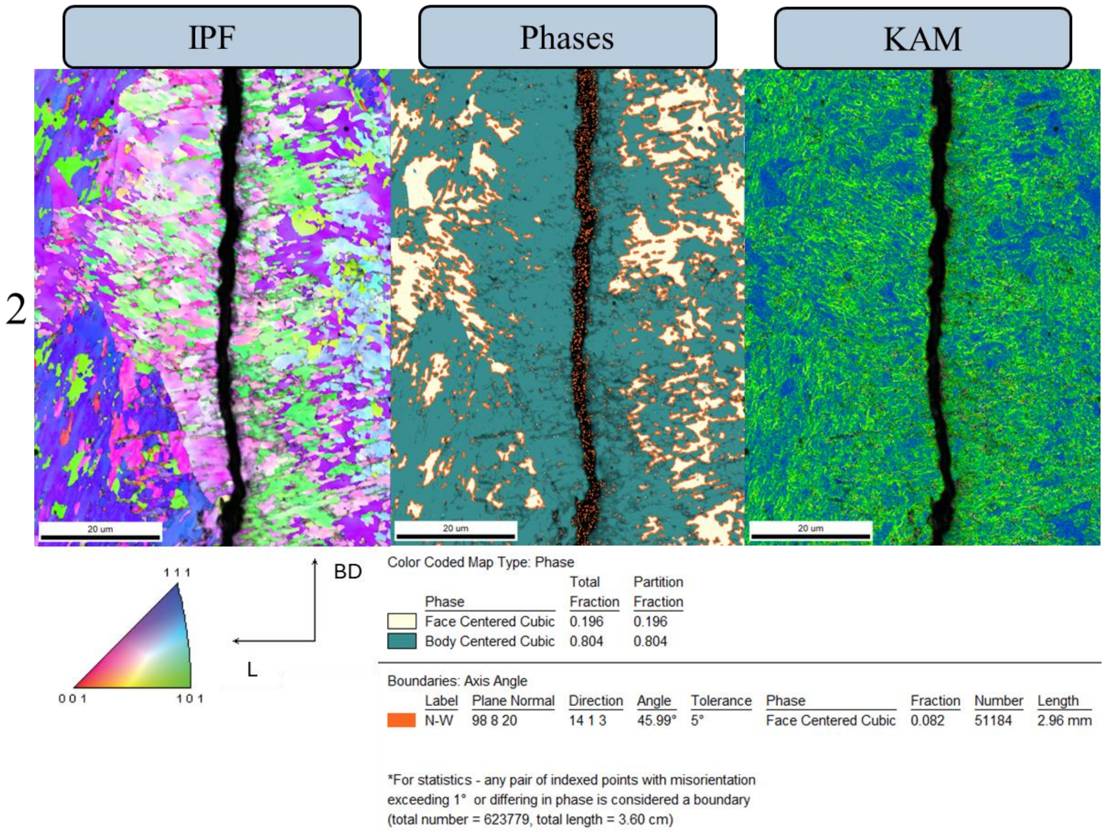

Color Coded Map Type: Phase

	Phase	Total Fraction	Partition Fraction
☐	Face Centered Cubic	0.196	0.196
■	Body Centered Cubic	0.804	0.804

Boundaries: Axis Angle

	Label	Plane Normal	Direction	Angle	Tolerance	Phase	Fraction	Number	Length
■	N-W	98 8 20	14 1 3	45.99°	5°	Face Centered Cubic	0.082	51184	2.96 mm

*For statistics - any pair of indexed points with misorientation exceeding 1° or differing in phase is considered a boundary (total number = 623779, total length = 3.60 cm)

Figure 4.26 The surface EBSD map of region 2 of specimen DL, as shown in Figure 4.24. Step size of 0.1 μm was used for scanning.

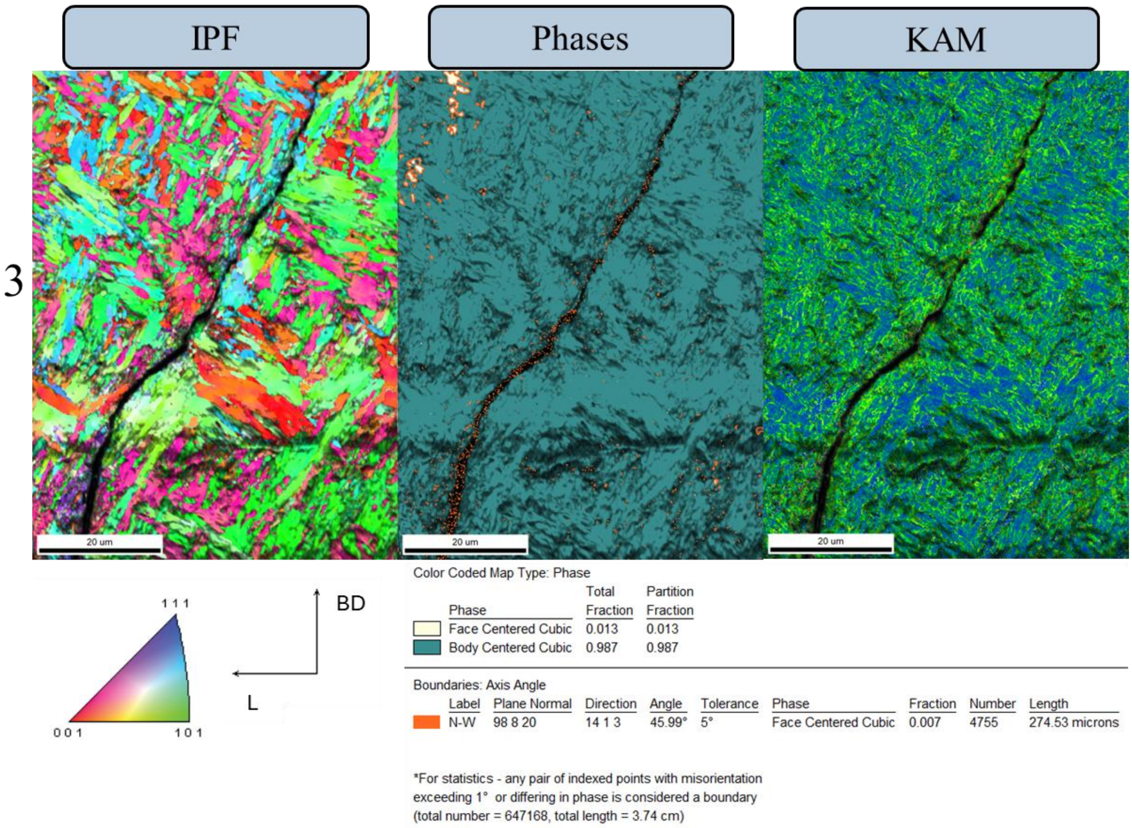

Color Coded Map Type: Phase

	Phase	Total Fraction	Partition Fraction
□	Face Centered Cubic	0.013	0.013
■	Body Centered Cubic	0.987	0.987

Boundaries: Axis Angle

	Label	Plane Normal	Direction	Angle	Tolerance	Phase	Fraction	Number	Length
🟧	N-W	98 8 20	14 1 3	45.99°	5°	Face Centered Cubic	0.007	4755	274.53 microns

*For statistics - any pair of indexed points with misorientation exceeding 1° or differing in phase is considered a boundary (total number = 647168, total length = 3.74 cm)

Figure 4.27 The surface EBSD map of region 3 of specimen DL, as shown in Figure 4.24. Step size of 0.1 μm was used for scanning.

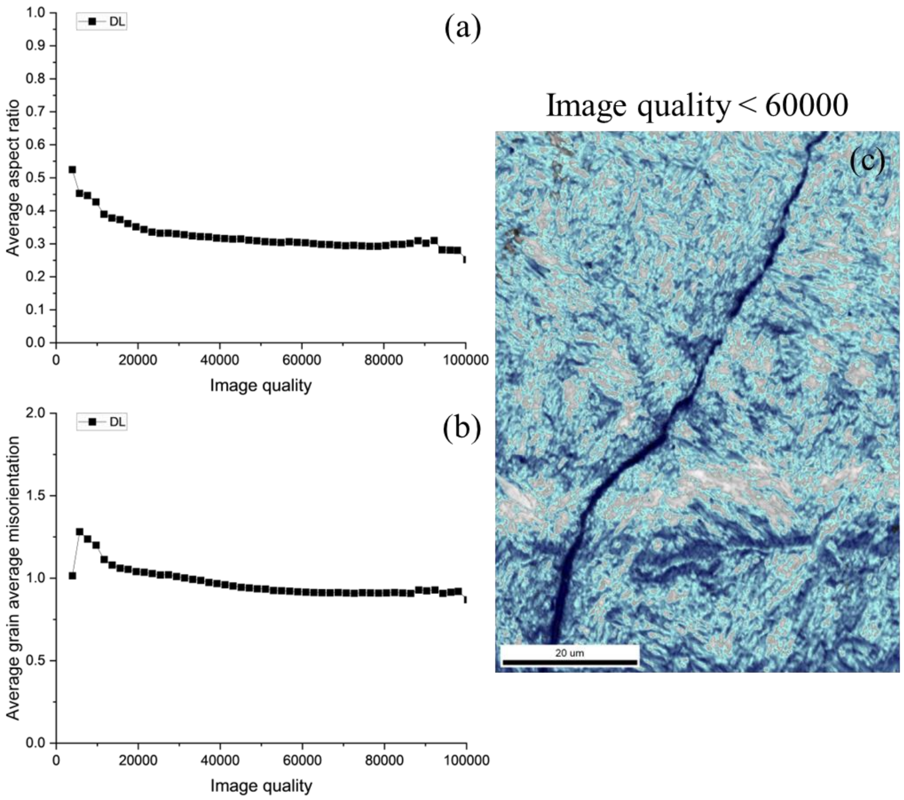

Figure 4.28 (a) Average aspect ratio and (b) average grain average misorientation with respect to the image quality. (c) Image quality of less than 60,000 for specimen DL region 3, as shown in Figure 4.27.

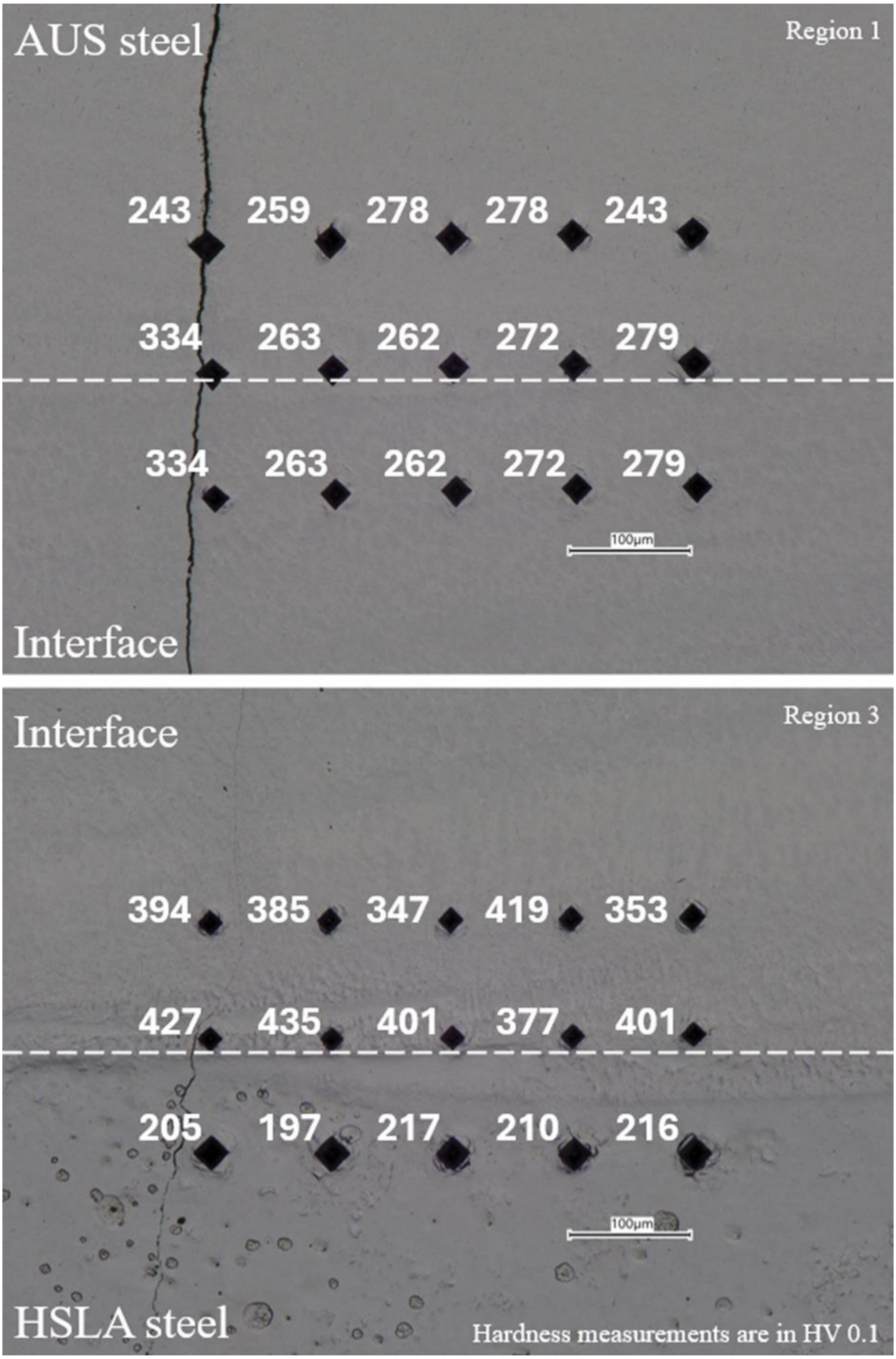

Figure 4.29 The hardness measurements of specimen DL in HV 0.1. The measurements are close to EBSD regions 1 and 3, as shown in Figure 4.24.

Figure 4.30 shows the EBSD map of the surface of the DT specimen, tested under a constant ΔK and R ratio of 0.5. The white, blue, and green arrows show similar features to specimen DL. The crack flanks also appear to be BCC phase. To investigate further, a close-up map was taken from the regions marked as 4. Figure 4.31 shows region 4, where the BCC phase is formed around the crack flanks within the interface. The AUS steel did not transform to BCC, showing that TRIP occurs only in the interface. The aspect ratio and grain average misorientation were plotted with respect to the image quality as shown in Figure 4.32 (a) and (b). The aspect ratio tends to increase with respect to lower image quality. This trend may have become more visible due to the absence of other ferritic phases. The low image quality shown in Figure 4.32 (c) appears to be concentrated around the crack flanks, which could be related to TRIP. To validate the presence of martensite around crack flanks, hardness measurements were taken as shown in Figure 4.33. It can be noted that within the interface hardness is higher closer to crack flanks by 27-53%. However, in AUS steel, the hardness was increased by only 7%. The larger difference in hardness in the interface could be attributed to a larger volume transformed to martensite due to a higher R ratio for DT in comparison to DL.

Figure 4.34 shows the EBSD map of the middle section of the DT specimen, tested under a constant ΔK and R ratio of 0.5. The white arrow shows similar features to the specimen DL. Region 5 is marked for a close-up map shown in Figure 4.35. A clear distinction from AUS steel to interface can be observed. AUS steel has larger FCC grains in the range of 100 μm with inter-dendritic ferrite. The interface is composed of elongated ferrite grains in the range of 10 μm. The grains in the interface could be a result of TRIP or pre-existing martensite. The aspect ratio and grain average misorientation were plotted with respect to the image quality as shown in Figure 4.36 (a) and (b). The aspect ratio and grain average misorientation tend to increase with respect to lower image quality. The low image quality shown in Figure 4.36 (c) appears to be concentrated around the crack flanks. This indicates that only the ferritic region close to the crack flanks shows a lower image quality. Thus, under plane strain conditions, the distinction between deformation-induced martensite and pre-existing martensite and ferrite could be done with respect to image quality, aspect ratio and grain average misorientation.

Figure 4.37 shows the EBSD map of the middle section of the GG specimen, tested under a constant ΔK and R ratio of 0.5. The white arrow shows similar features to previous specimens. Region 6 is marked for a close-up map shown in Figure 4.38. The aspect ratio and grain average misorientation were plotted with respect to the image quality as shown in Figure 4.39 (a) and (b). The aspect ratio and grain average misorientation tend to increase with respect to lower image quality. The low image quality shown in Figure 4.39 (c) appears to be concentrated around the crack flanks. This indicates that the observations are consistent for both L and T orientations. However, the distinction between martensite is not consistent for all specimens. This will require further investigation in a future study.

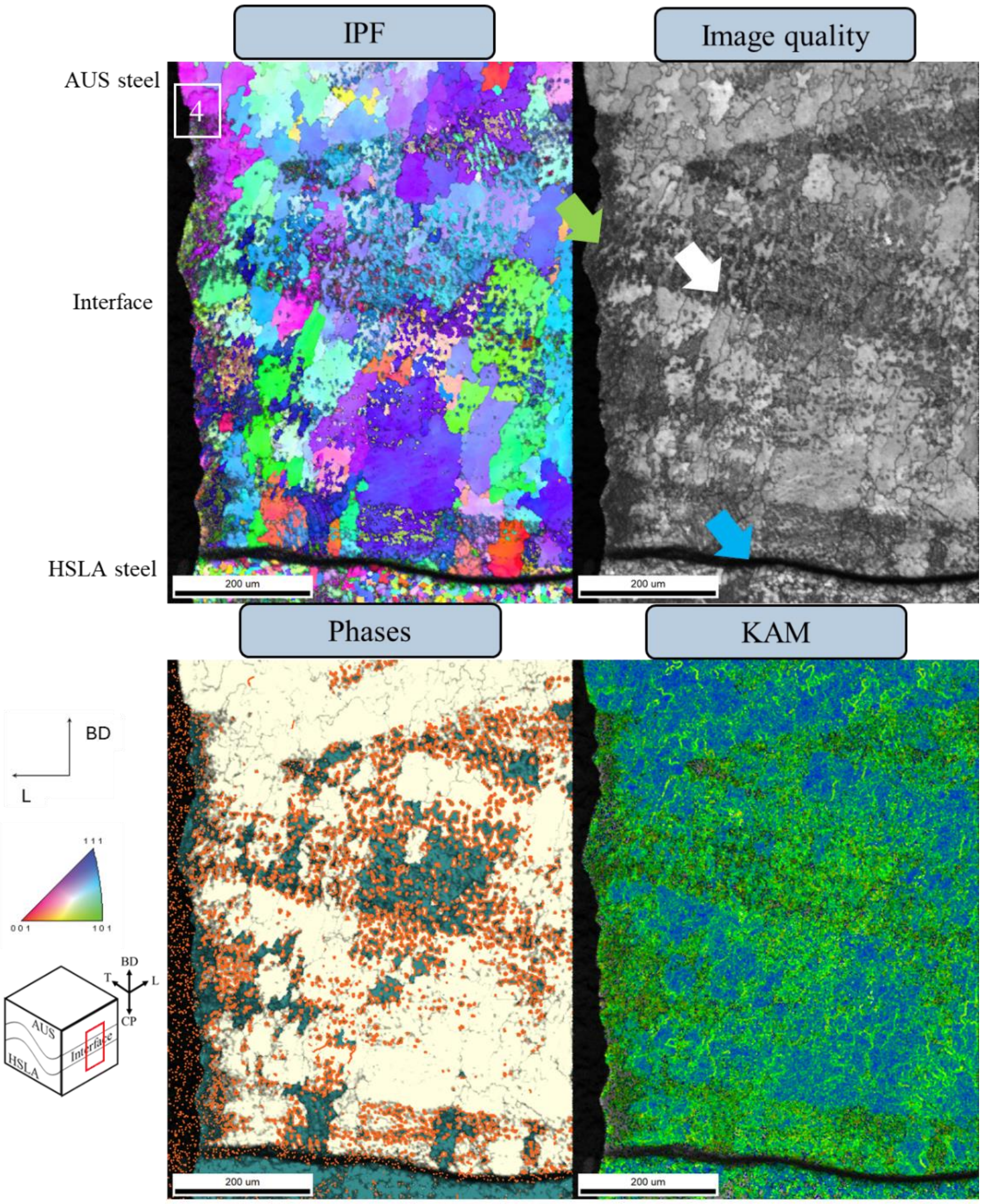

Gray Scale Map Type:Image Quality
2441.12...83922.1 (2441.12...43181.6)

Color Coded Map Type: Phase

	Phase	Total Fraction	Partition Fraction
🟨	Face Centered Cubic	0.676	0.676
🟦	Body Centered Cubic	0.324	0.324

Boundaries: Axis Angle

	Label	Plane Normal	Direction	Angle	Tolerance	Phase	Fraction	Number	Length
🟧	N-W	98 8 20	14 1 3	45.99°	5°	Face Centered Cubic	0.114	38851	3.36 cm

*For statistics - any pair of indexed points with misorientation exceeding 1° or differing in phase is considered a boundary (total number = 339648, total length = 29.41 cm)

Figure 4.30 The surface EBSD map of an L-oriented specimen tested under constant ΔK at load ratio of 0.5, labelled as DT. The white arrow points to the low image quality region in the interface. The blue arrow points to the low image quality region at the fusion boundary. The green arrow points to the low image quality region around the crack flanks. Region 4 is marked. Step size of 0.1 µm was used for scanning.

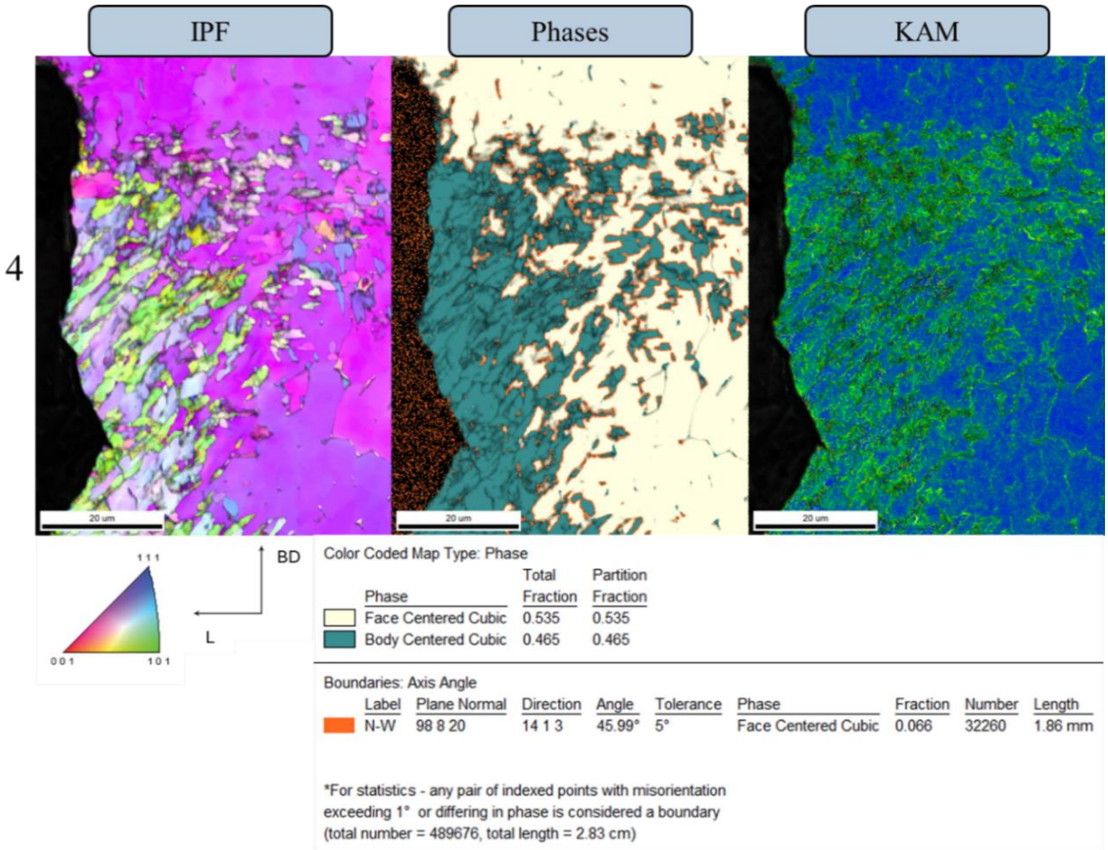

Figure 4.31 The surface EBSD map of region 4 of specimen DT, as shown in Figure 4.30. Step size of 0.1 μm was used for scanning.

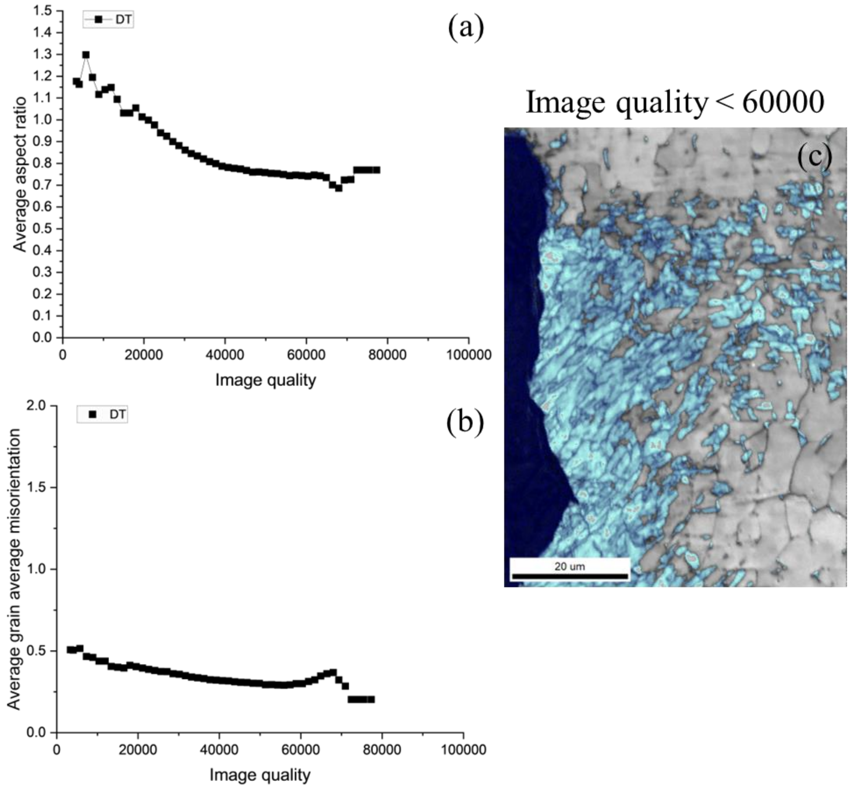

Figure 4.32 (a) Average aspect ratio and (b) average grain average misorientation with respect to the image quality. (c) Image quality of less than 60,000 for specimen DT region 4, as shown in Figure 4.31.

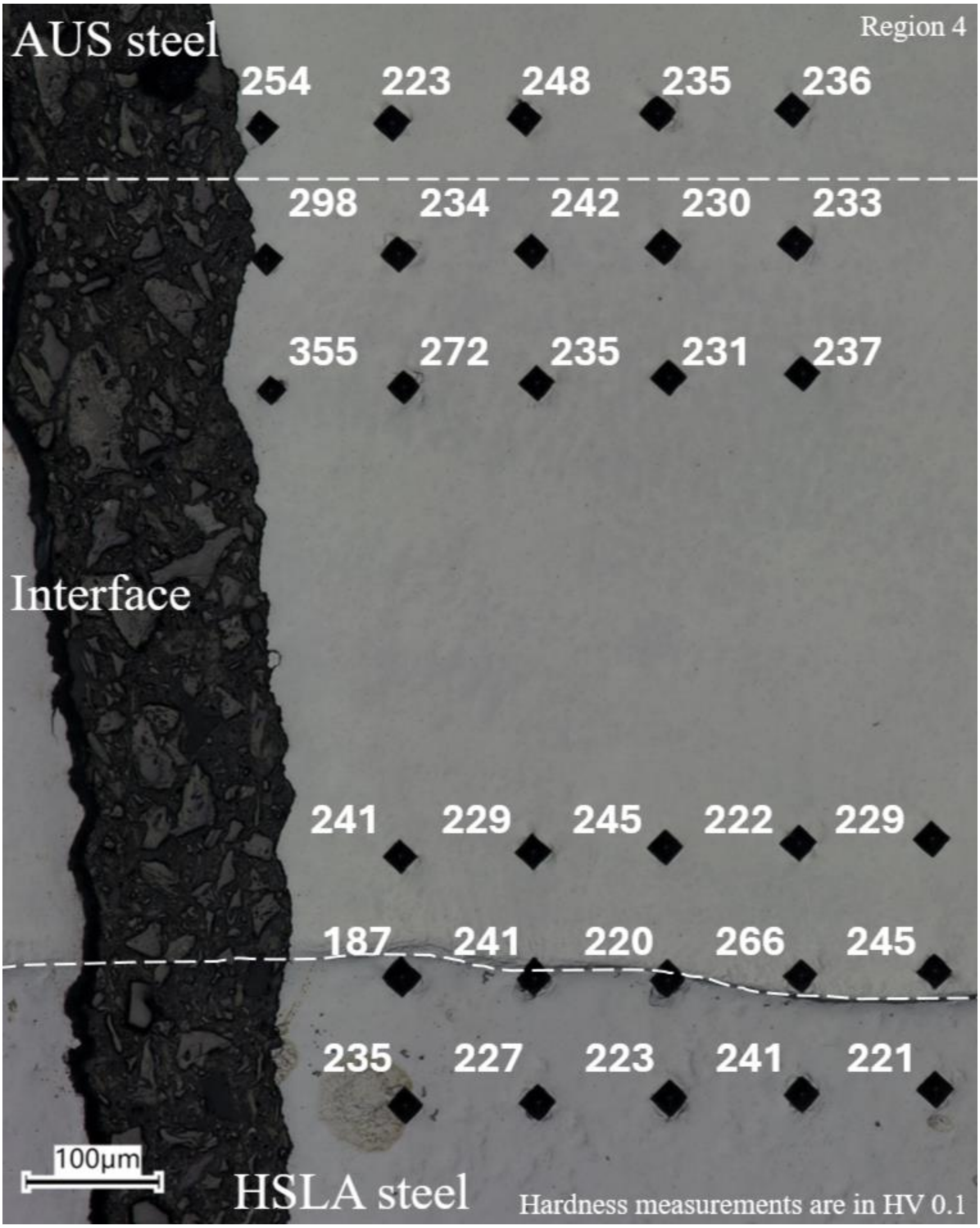

Figure 4.33 The hardness measurements of specimen DT in HV 0.1. The measurements are close to EBSD region 4, as shown in as shown in Figure 4.30.

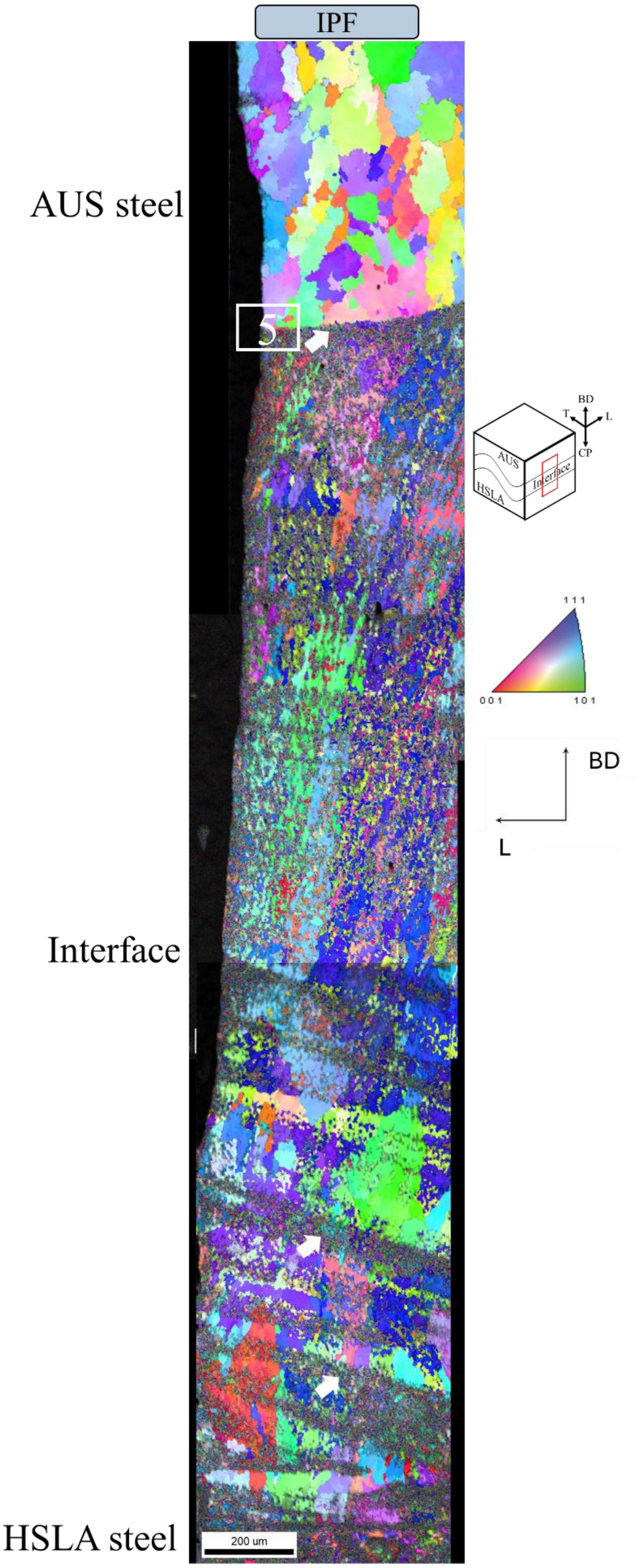

Figure 4.34 The middle section EBSD map of an L-oriented specimen tested under constant ΔK at load ratio of 0.5, labelled as DT-mid. Three IPF maps were digitally stitched to obtain this image. The white arrow points to the low image quality region in the interface. The scale shown is 200 μm. Region 5 is marked. Step size of 1.5 μm was used for scanning.

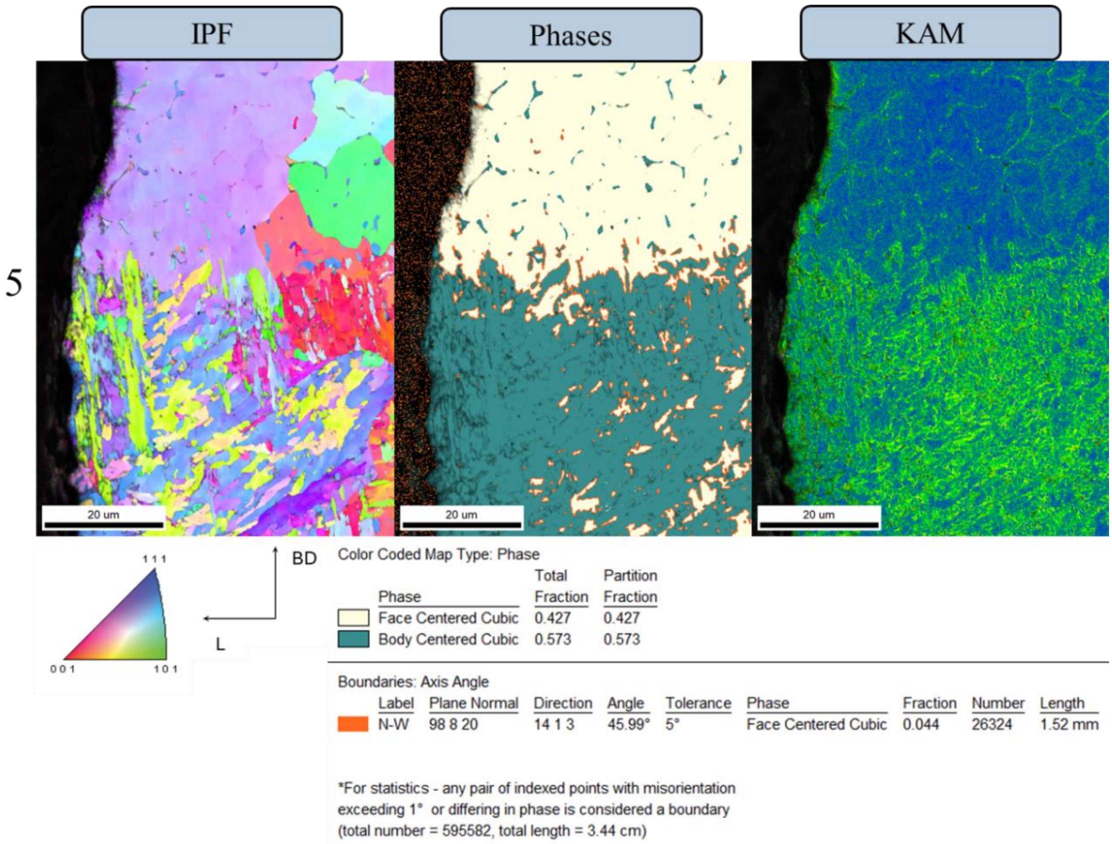

Color Coded Map Type: Phase

	Phase	Total Fraction	Partition Fraction
☐	Face Centered Cubic	0.427	0.427
■	Body Centered Cubic	0.573	0.573

Boundaries: Axis Angle

	Label	Plane Normal	Direction	Angle	Tolerance	Phase	Fraction	Number	Length
■	N-W	98 8 20	14 1 3	45.99°	5°	Face Centered Cubic	0.044	26324	1.52 mm

*For statistics - any pair of indexed points with misorientation exceeding 1° or differing in phase is considered a boundary (total number = 595582, total length = 3.44 cm)

Figure 4.35 The middle section EBSD map of region 5 of specimen DT-mid, as shown in Figure 4.34. Step size of 0.1 μm was used for scanning.

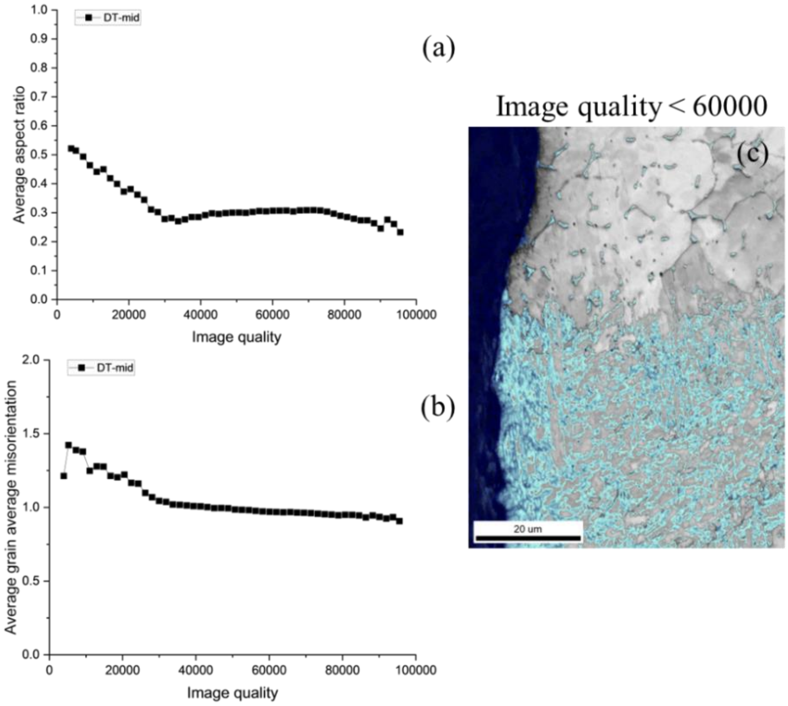

Figure 4.36 (a) Average aspect ratio and (b) average grain average misorientation with respect to the image quality. (c) Image quality of less than 60,000 for specimen DT-mid region 5, as shown in Figure 4.35.

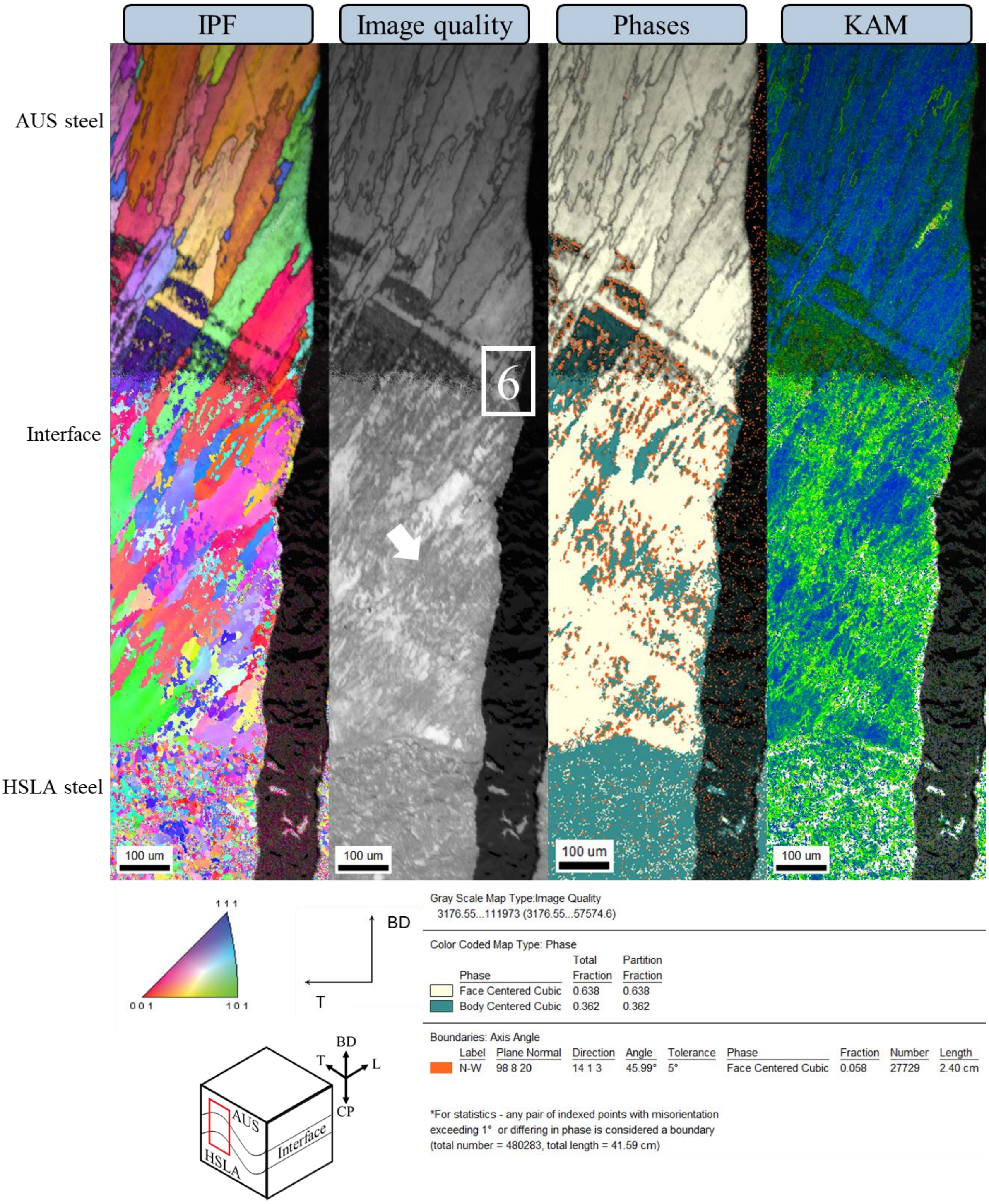

Gray Scale Map Type:Image Quality
3176.55...111973 (3176.55...57574.6)

Color Coded Map Type: Phase

	Phase	Total Fraction	Partition Fraction
▭	Face Centered Cubic	0.638	0.638
■	Body Centered Cubic	0.362	0.362

Boundaries: Axis Angle

	Label	Plane Normal	Direction	Angle	Tolerance	Phase	Fraction	Number	Length
■	N-W	98 8 20	14 1 3	45.99°	5°	Face Centered Cubic	0.058	27729	2.40 cm

*For statistics - any pair of indexed points with misorientation exceeding 1° or differing in phase is considered a boundary (total number = 480283, total length = 41.59 cm)

Figure 4.37 The middle section EBSD map of a T-oriented specimen tested under constant ΔK at load ratio of 0.5, labelled as GG-mid. The white arrow points to the low image quality region in the interface. The scale shown is 100 μm. Region 6 is marked. Step size of 1.5 μm was used for scanning.

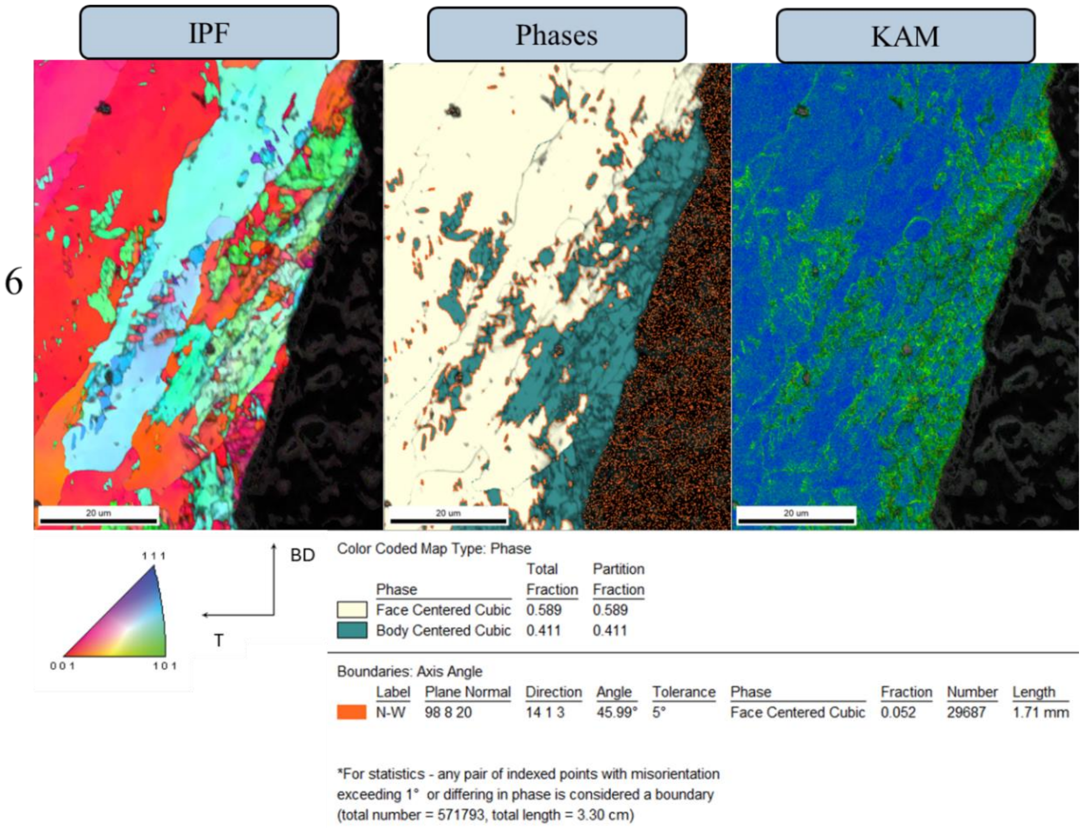

Color Coded Map Type: Phase

Phase	Total Fraction	Partition Fraction
Face Centered Cubic	0.589	0.589
Body Centered Cubic	0.411	0.411

Boundaries: Axis Angle

Label	Plane Normal	Direction	Angle	Tolerance	Phase	Fraction	Number	Length
N-W	98 8 20	14 1 3	45.99°	5°	Face Centered Cubic	0.052	29687	1.71 mm

*For statistics - any pair of indexed points with misorientation exceeding 1° or differing in phase is considered a boundary (total number = 571793, total length = 3.30 cm)

Figure 4.38 The middle section EBSD map of region 6 of specimen GG-mid, as shown in Figure 4.37. Step size of 0.1 μm was used for scanning.

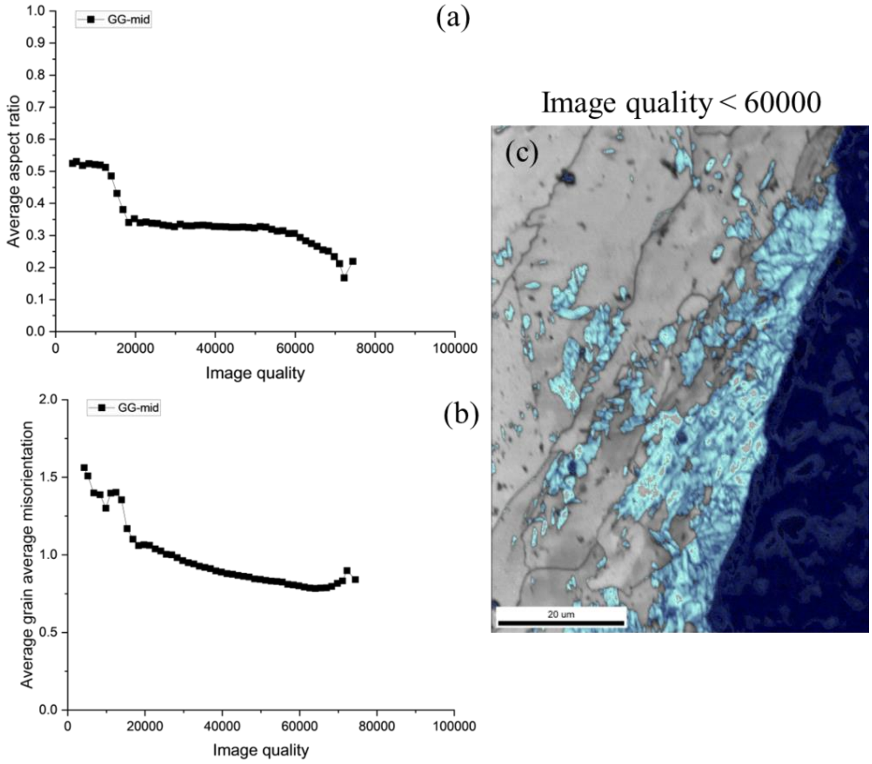

Figure 4.39 (a) Average aspect ratio and (b) average grain average misorientation with respect to the image quality. (c) Image quality of less than 60,000 for specimen GG-mid region 6, as shown in Figure 4.38.

The present EBSD analysis of the crack profile suggests that TRIP must have aided in the reduction of the crack propagation rate before the interface. In addition to the absorption of deformation, the transformation from FCC to BCC results in an increase of volume by 2.57%, thereby increasing crack closure effects. This results in an increased fatigue crack growth resistance. Such an improvement in fatigue crack growth resistance due to martensite transformation has been reported by multiple studies [106], [107].

However, this theory is contradictory to the gradual acceleration of the crack growth rate within the interface observed in this study. The accelerated crack growth rate is observed for R ratio of 0.1 and 0.5. The increased R ratio with larger load values can result in a larger TRIP zone as indicated by the hardness measurements. This should have resulted in a lower crack growth rate. Additionally, increased crack growth acceleration was also observed for near-threshold regions at lower load levels and higher load ratios of 0.9.

A possible reason for the anomaly could be the influence of TRIP on the roughness and plasticity-induced crack closure. Jambor et al. [108] studied the fatigue crack growth behaviour in the near-threshold region of 304L produced by laser powder bed fusion. Their tests revealed a lower fatigue crack growth resistance of 3D printed material in comparison to wrought material. This behaviour was attributed to an absence of crack closure. They suggest that the martensite formed around crack flanks causes a reduction in roughness and plastically induced crack closure. This is further supported by the quasi-brittle nature of the fracture surfaces in the present study.

A combined effect of brittle martensite zones and the martensite layer at the FB formed during material fabrication, and the reduced crack closure due to TRIP may be the reason for crack acceleration. However, in the present study, the effects of crack closure were not verified due to the small specimen size. In a future study, CTOD experiments should be conducted at different ΔK levels and R ratios to identify the influence of crack closure.

5. Conclusions

Based on the literature review of the state of the art, a set of research questions were formulated. The conclusions presented in this section are corresponding to each of the research questions.

- **Study and benchmark of fatigue properties of HSLA and AUS steel.**

The mono-materials HSLA steel (ER70S-6) and AUS steel (ER316L) manufactured by wire arc additive manufacturing were benchmarked and studied with fatigue crack growth rate experiments. The Paris parameters and the threshold stress intensity range were obtained. A comparison of the Paris slope parameter with literature revealed a 16% higher value for HSLA steel and a -5% to 20% variation for AUS steel. The significant variation in AUS steel was due to anisotropy. Upon comparison of mono-materials with each other, HSLA steel showed 43 to 77% lower Paris slope parameter. The threshold stress intensity range of both materials was similar. A lower Paris slope parameter suggested a better fatigue resistance for HSLA steel. HSLA steel also showed 8.5% higher hardness compared to AUS steel. A correlation study of hardness and Paris slope parameters was done for HSLA steel. A power law dependence was observed for the Paris slope parameter and hardness values. Higher hardness was related to lower Paris slope parameters and better fatigue crack growth resistance. The reason for this correlation was attributed to the grain sizes. Smaller grains can result in better fatigue resistance as well as a higher hardness. Hence, hardness measurements can be an indirect measurement of fatigue resistance.

HSLA steel showed no anisotropy which suggests a homogeneous behaviour due to small grain size which was in the order of 10 µm. AUS steel on the other hand showed an anisotropic behaviour, with the Paris slope parameter of AUS steel in Longitudinal orientation being 26.5% higher than Transverse orientation. The anisotropy of AUS steel was attributed to the 10 times larger grain size in diameter in comparison to HSLA steel, and the difference in bead structure, which resulted in lesser homogeneity.

Constant ΔK experiments at 20 MPa√m of mono-materials verified the anisotropy observed in AUS steel. In comparison to longitudinal orientation, transverse orientation showed an increase of 61.7% for an R ratio of 0.1 and 37.9% for an R ratio of 0.5. Additionally, an increase in crack growth rate was observed with an increase in the R ratio, suggesting a reduced crack closure effect. The increase between R ratios was 50% higher for HSLA steel than AUS steel. This was attributed to higher ductility and higher effective minimum stress intensity factor of austenitic stainless steels compared to ferritic steels reported in the literature. However, to verify this, an effective minimum stress intensity factor should be measured in a future study using crack tip opening displacement experiments.

- **Study and benchmark of fatigue properties at the interface of functionally graded HSLA and AUS steel.**

The bi-material composed of functionally graded HSLA steel and AUS steel were studied with fatigue crack growth rate experiment with the crack propagating from AUS steel to HSLA steel. The focus of this set of experiments was to gain an understanding of the fatigue properties at the interface formed during functional grading. The results showed significant scatter due to the inconsistent position of the interface. Under increasing and decreasing ΔK tests distinctions between the orientations were difficult to verify. However, a change in the crack growth rate at the interface region was observed. Obtaining Paris parameters and threshold stress intensity range was challenging owing to these changes observed in the interface region as well as due to the high scatter. Further investigation with constant ΔK experiments was done for better clarity.

Constant ΔK experiments at 20 MPa√m and R ratio of 0.1 and 0.5 revealed the effects of interface region on the crack propagation rates. The crack growth rate tends to decelerate mm/cycle before the interface region and gradually accelerates throughout the interface. The decrease during deceleration was in the range of 5.1E-05 to 6.1E-05 mm/cycle and the increase during acceleration was in the range of 5.5E-05 to 1.32E-04 mm/cycle. For deceleration, no significant dependence on orientation and R ratio was observed. However, the increase during acceleration for longitudinal orientation was twice that of transverse orientation. In addition, a sudden acceleration of 2 to 5 times higher than the gradual acceleration was observed in the HSLA steel part of the transverse-oriented bi-material. Further investigation of these observations was done through microscopy, fractography and EBSD analyses, to understand the influence of microstructure.

- **Investigate the influence of the microstructure on crack propagation at the interface.**

The microstructure of HSLA steel consists of mostly BCC and AUS steel consists of mostly FCC. The interface consisted of both FCC and BCC grains. When the crack grows from FCC in AUS steel to a mix of FCC and BCC grains in the interface region, more grain boundaries would be present to restrict the growth. Hence, the deceleration was attributed to the change in microstructure. Martensite was also present in the interface region and at the fusion boundary of HSLA steel. The hardness at the fusion boundary of HSLA steel was twice that of the ferrite in HSLA steel, thus validating the presence of martensite. These observations were consistent with the literature. These martensitic phases aided in the gradual acceleration of the crack growth rate within the interface.

The area of the interface was measured in the fractographs. The specimens in longitudinal orientation had a 33% larger interface than the transverse orientation. A larger presence of interface results in an increased presence of martensite. This resulted in the anisotropy in the gradual acceleration in constant ΔK experiments.

Fractographs also revealed the presence of porous defects in HSLA steel. These defects were oriented in the longitudinal direction suggesting that it was process-induced. The location of the pore in the fractograph matched the crack length at which sudden acceleration was observed in the constant ΔK experiment. Hence, porous defects resulted in the sudden acceleration of the crack growth rate. No defects were observed for AUS steel.

Fractographs of bi-materials under scanning electron microscope revealed features such as ridges, secondary cracks, pores, and striations. The secondary cracks were observed at the AUS steel near the interface region. As secondary cracks are known to absorb energy, it may have contributed to the deceleration observed before the interface region. The striations observed in fractographs were higher than the measurements from the experiment by 6.32E-04 mm/cycle. This difference was attributed to the errors associated with the potential drop method. Brittle regions were observed near the interface region and the fusion boundary, further supporting the detrimental effect of solidification martensite. The interface region appeared to be less rough compared to either of the mono-materials.

Electron back scattered diffraction analysis was done around the crack flanks from the fusion boundary of AUS steel and interface to interface and HSLA steel. Low image quality zones at the fusion boundary and within the interface region were observed for all maps which was related to the presence of martensite. The crack flanks always appeared to be the BCC phase within the interface. This suggests that the deformation is first absorbed through transformation into BCC structure followed by the crack extension. This was verified through a series of hardness measurements taken to compare the area close to and away from the crack flanks. In AUS steel, the area close to crack flanks had 7% higher hardness. Within the interface, this difference was 27 to 53%. The transformation-induced plasticity (TRIP) effect is commonly reported in the literature for metastable austenitic stainless steel. The consensus in the literature on the effect of TRIP effect is a reduced crack growth rate. This may be another reason for the reduced crack growth rate as the crack grows from AUS steel to the interface. However, following this theory, further decrease can be expected in the interface. This is contradictory to the accelerated crack growth observed within the interface. Further investigation suggested a possibility of reduction of roughness and plasticity-induced crack closure due to TRIP. This also explains the lower topographical features on the fracture surface observed for the interface region in comparison to the mono-materials. However, a future study with crack tip opening displacement should be done to verify the effects of crack closure.

➢ General conclusions

In the application of functionally graded HSLA and AUS steel, the AUS steel cladding would be at the surface where the cracks can initiate and propagate into the material. Though the fatigue resistance of AUS steel is lower than HSLA steel, the presence of the interface acts as a protective layer by decelerating the crack growth. However, within the interface region, gradual acceleration in crack growth rate is observed, which can be detrimental to a structure. This acceleration is due to the martensite present in the interface and a possible reduction of roughness and plasticity-induced crack closure caused by deformation-induced martensitic transformation. For reliable application of this functionally graded material, the presence of martensite should be mitigated.

The present work investigated the fatigue behaviour of functionally graded HSLA steel and AUS steel. Though an understanding of crack propagation in the FGM was obtained, this study lacks data on the crack closure effects. This should be measured with crack tip opening displacement experiments which was not possible in the present work due to the small size of the test specimen. Another limitation in the present work is the errors associated with the potential drop method for a functionally graded material. There is also a lack of standardisation of fatigue tests for graded materials. These issues should be addressed to improve the methodology in a future study.

6. Recommendations

In the present work, the fatigue properties of functionally graded HSLA and AUS steel were investigated. As seen in the conclusions, the present study can be enhanced for a better understanding of such graded material. Moreover, such graded material should also be tested under the conditions of the intended application. The following recommendations list the possible directions for a follow-up study:

1. Crack tip opening displacement experiments under different ΔK levels and different R ratios can be conducted to understand the crack closure effects on the observed behaviour of crack growth rate at the interface. For the HSLA steel and AUS steel, the effect of K_{op} can be understood.

2. Effects of the environment need to be studied for reliable application. The effect of a corrosive environment and extreme temperatures can be studied. This will validate the application of the FGM in offshore environments, arctic conditions, and nuclear power plants.

3. The effects of residual stress should be studied with X-ray or neutron diffraction. This study can be complemented with several post-weld heat treatments.

4. The effects of heat treatment on the microstructure can be studied. Heat treatment can affect the composition of the interface, especially the martensite.

5. The effects of different deposition strategies on fatigue behaviour can be studied. This is important to avoid process-induced defects. Additionally, the anisotropic behaviour of AUS steel can also be studied under different deposition strategies.

6. Standardization of the procedure for fatigue testing of functionally graded materials is required for an improved methodology.

7. A sensitivity analysis of the potential drop technique can be done to improve the accuracy.

7. Appendix

7.1. Simplified Correction Factor for K-solution

A simplified correction factor was used for K-solution in constant ΔK tests of BM. An example of this correction factor for a fusion line halfway across the specimen is shown in Figure 7.1. This correction factor was varied linearly with respect to the visible fusion line for each BM specimen.

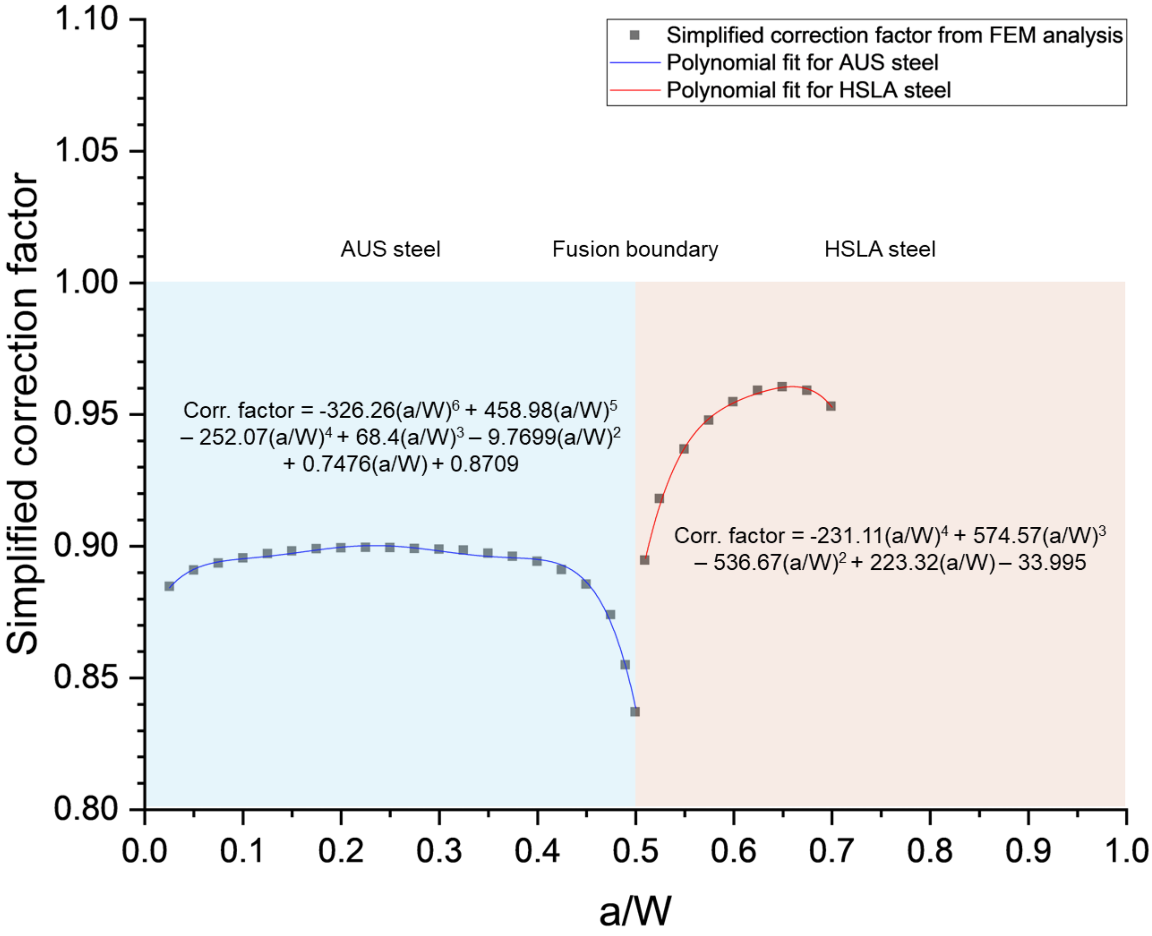

Figure 7.1 Simplified correction factor used for constant ΔK tests of BM.

7.2. Data Acquisition and Processing

The raw data obtained from tests contain a large number of data points. Three types of data acquisition were done, namely, peak-valley, timed and delta-level. Peak-valley data acquisition corresponds to the peak and valley of a load cycle. Timed data acquisition takes values at a rate of 100 Hz. The delta-level data acquisition takes data at every 0.1 mm crossing of crack length. For each acquisition, the number of cycles, force, stress intensity factor, displacement, DCPD signal V, and crack length were obtained.

The delta-level acquisition was done to obtain preliminary results and was not used for final results. The timed acquisition was used for the analysis of constant ΔF and constant ΔK tests. The peak-valley acquisition was used for the analysis of ΔKth tests. Table 7.1 shows the typical number of data points for each type of test.

The large number of data points needs to be meaningfully reduced for better manageability. Moreover, the DCPD signals often result in fluctuations which may give unreliable results. Hence a smoothening operation was performed on these raw data files to obtain the FCGR results. The algorithm used is shown in Figure 7.2. After data reduction, approximately 100 data points per mm can be obtained.

Table 7.1 The approximate number of data points for each type of test.

Type of test	**Type of data acquisition used for analysis**	**The approximate number of data points in the raw data file**
Constant ΔF test	Timed	500,000
Constant ΔK test	Timed	500,000
ΔKth test	Peak-valley	5,000,000

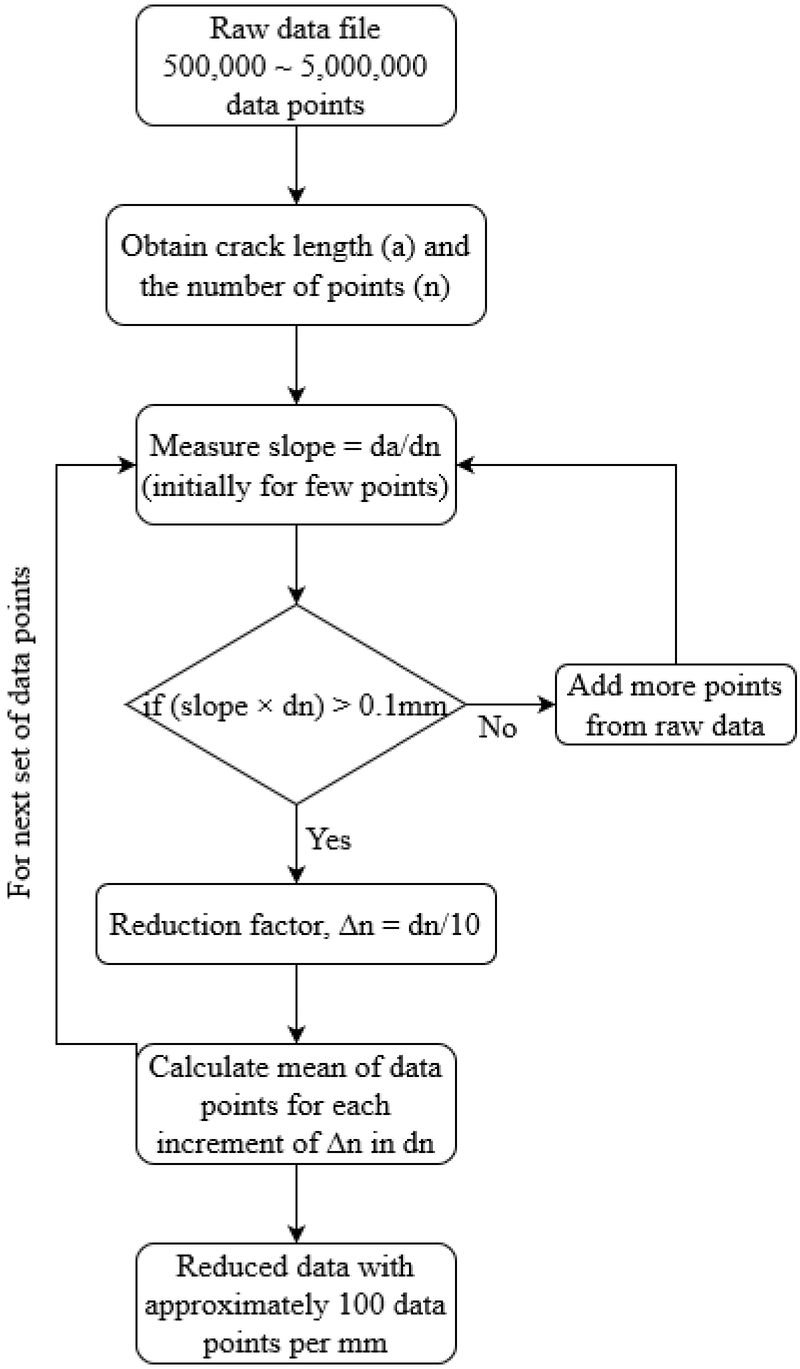

Figure 7.2 The flow chart depicting the algorithm used for data reduction.

7.3. Micrographs

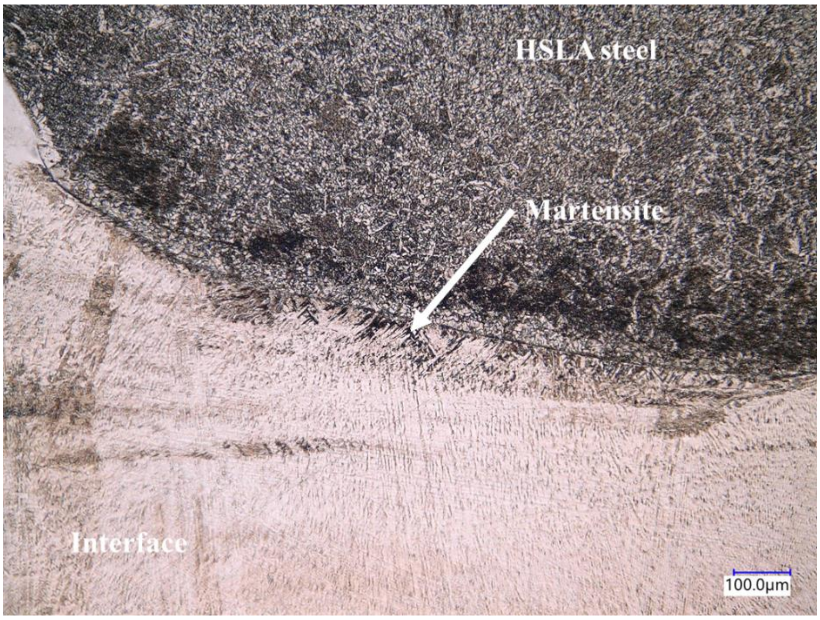

Figure 7.3 An over-etched specimen. Needle like martensitic features at the FB can be observed.

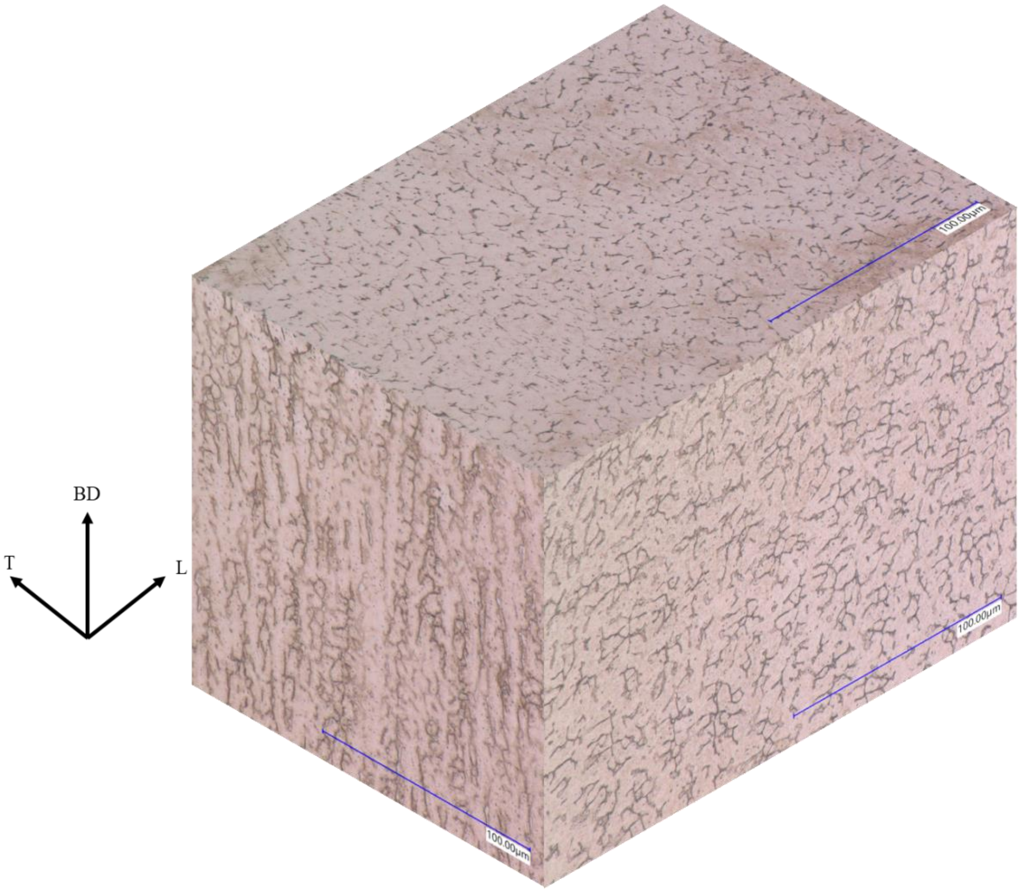

Figure 7.4 3D micrographs of AUS steel. Scale shows 100 μm.

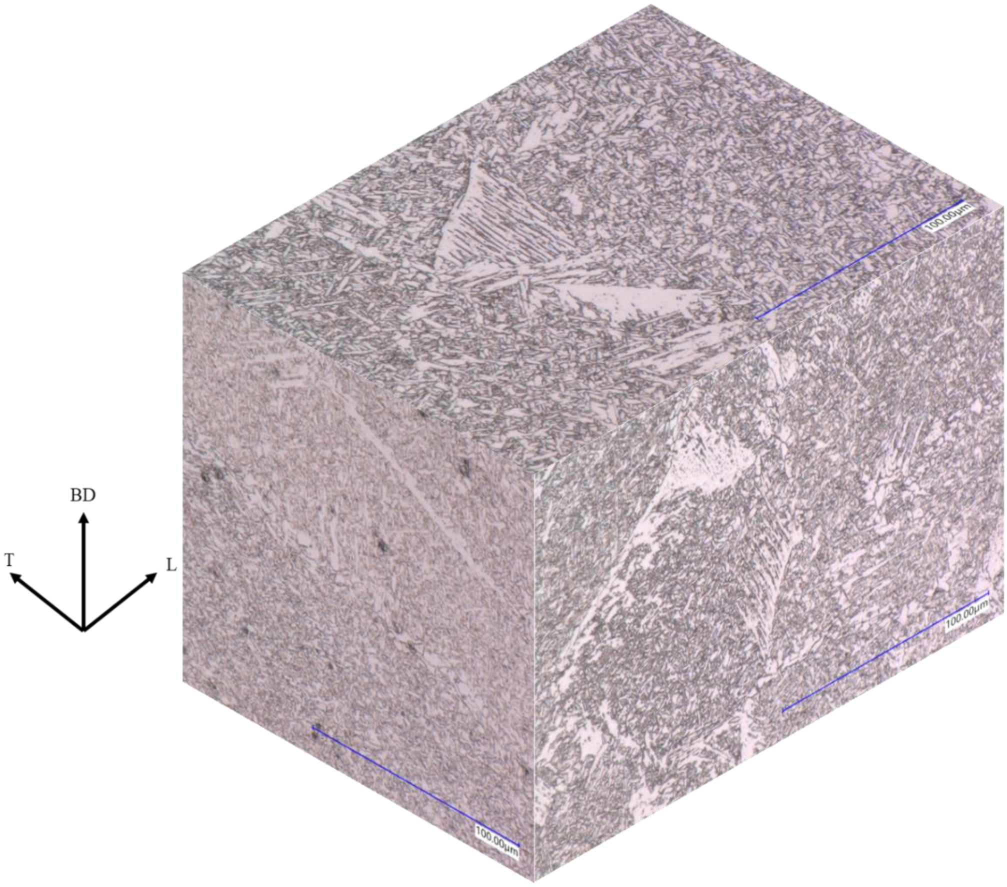

Figure 7.5 3D micrographs of HSLA steel. Scale shows 100 μm.

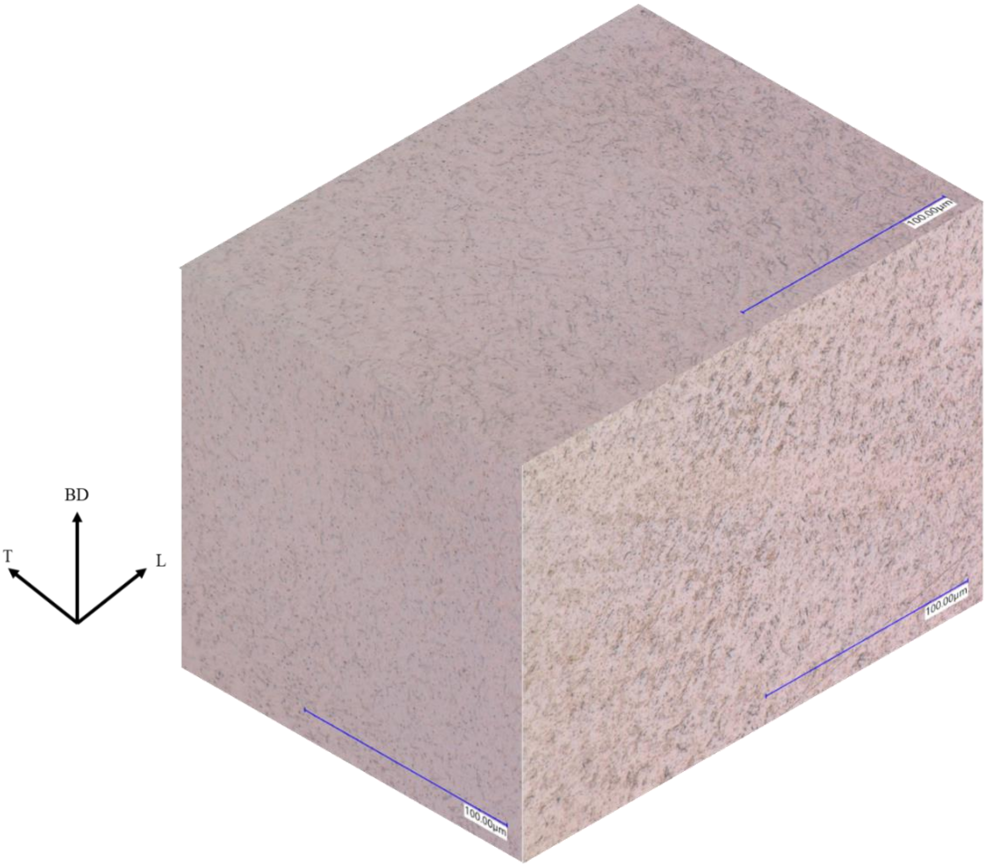

Figure 7.6 3D micrographs of Interface. Scale shows 100 μm.

7.4. DCPD Error Analysis

The measurements made by DCPD signal are not perfect. In this sub-section, the errors associated with the measurements are discussed. To measure the error, the constant ΔF specimens were selected. From the fractographs of the specimens, the final length can be measured, which is the actual measurement. The corresponding final measurement from the raw data file can also be obtained. By comparing these two, the differences in measurement for each type of specimen can be calculated. The error is tabulated as follows.

Table 7.2 The average magnitude of difference between actual and DCPD measurement.

Material type	Average difference (in magnitude) between the actual measurement and DCPD measurement (%)
HSLA-L	1.19
HSLA-T	5.35
AUS-L	6.91
AUS-T	3.47
BM-L	2.46
BM-T	6.80

It can be seen that the error ranges between 1.2% to 6.9%. These errors in measurements can affect the calculation of K for FCGR tests. Figure 7.7 shows the effect this range of error in the calculation of ΔK for a constant ΔF condition. It can be seen that the effect of the miscalculation increases with the crack length. This can mean that for experiments with smaller crack lengths, the results are more reliable than long cracks.

For constant ΔF experiments, the Paris parameters are calculated over a range of crack length. Hence, the effect of error may have been less. By measuring multiple specimens, the errors can be further minimized.

For threshold experiments, mono-materials were tested close to the notch. Hence the effect of error could have been lesser. The exception for this case was HSLA-T specimens. Due to pores, the experiments were started further away from the notch. Hence the effects of error could have been larger. This may be the reason for higher scatter for HSLA-T specimens. For BM specimens, all tests were carried out away from the notch. Hence, more errors are associated with the measurements. This makes it difficult to calculate the threshold value of the interface region.

For constant ΔK experiments in BM specimens, more scatter was seen for HSLA steel region than AUS steel region. As HSLA steel is further away from the notch, the errors associated with can be higher. Moreover, the changing position of the interface can also influence the calibration of the BM specimens. These two factors could have been the reason for the larger scattering in HSLA steel region.

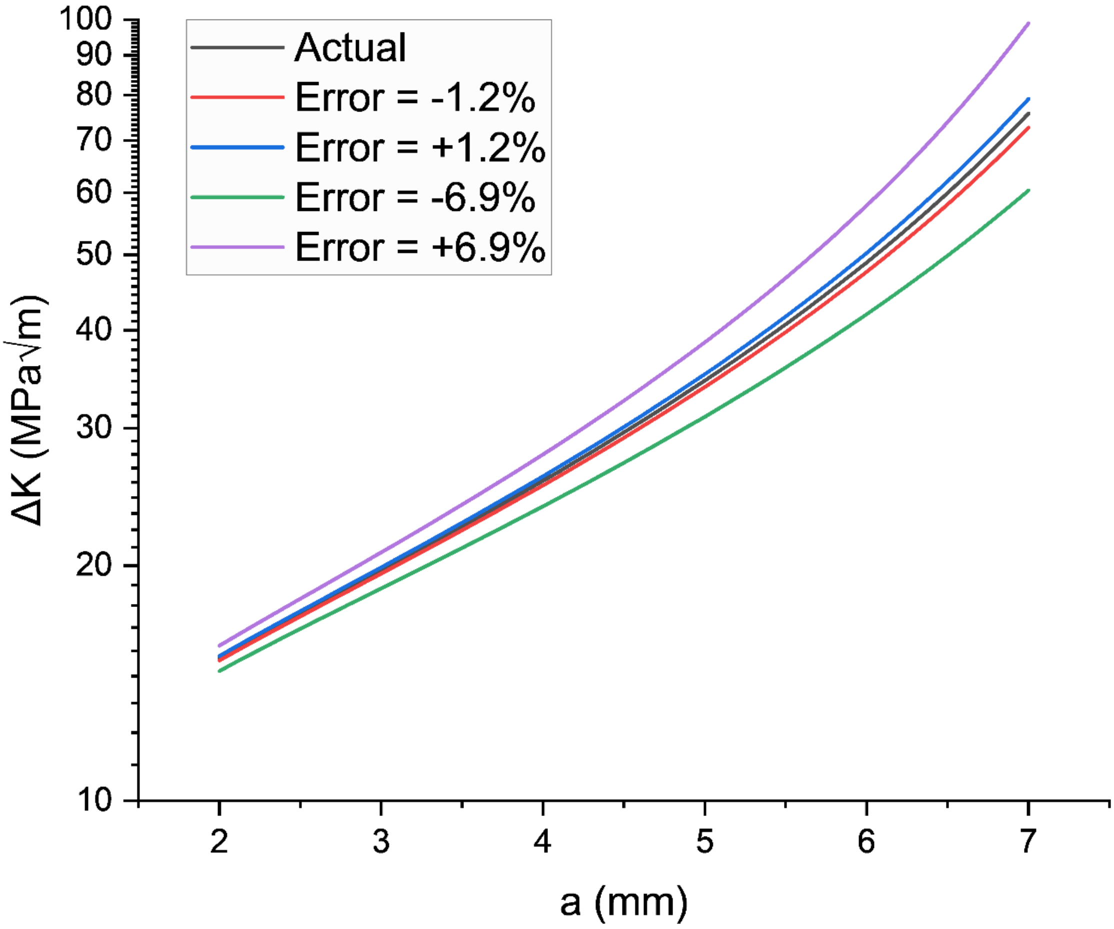

Figure 7.7 The error in ΔK due to error in crack length measurement.

7.5. FCGR Data

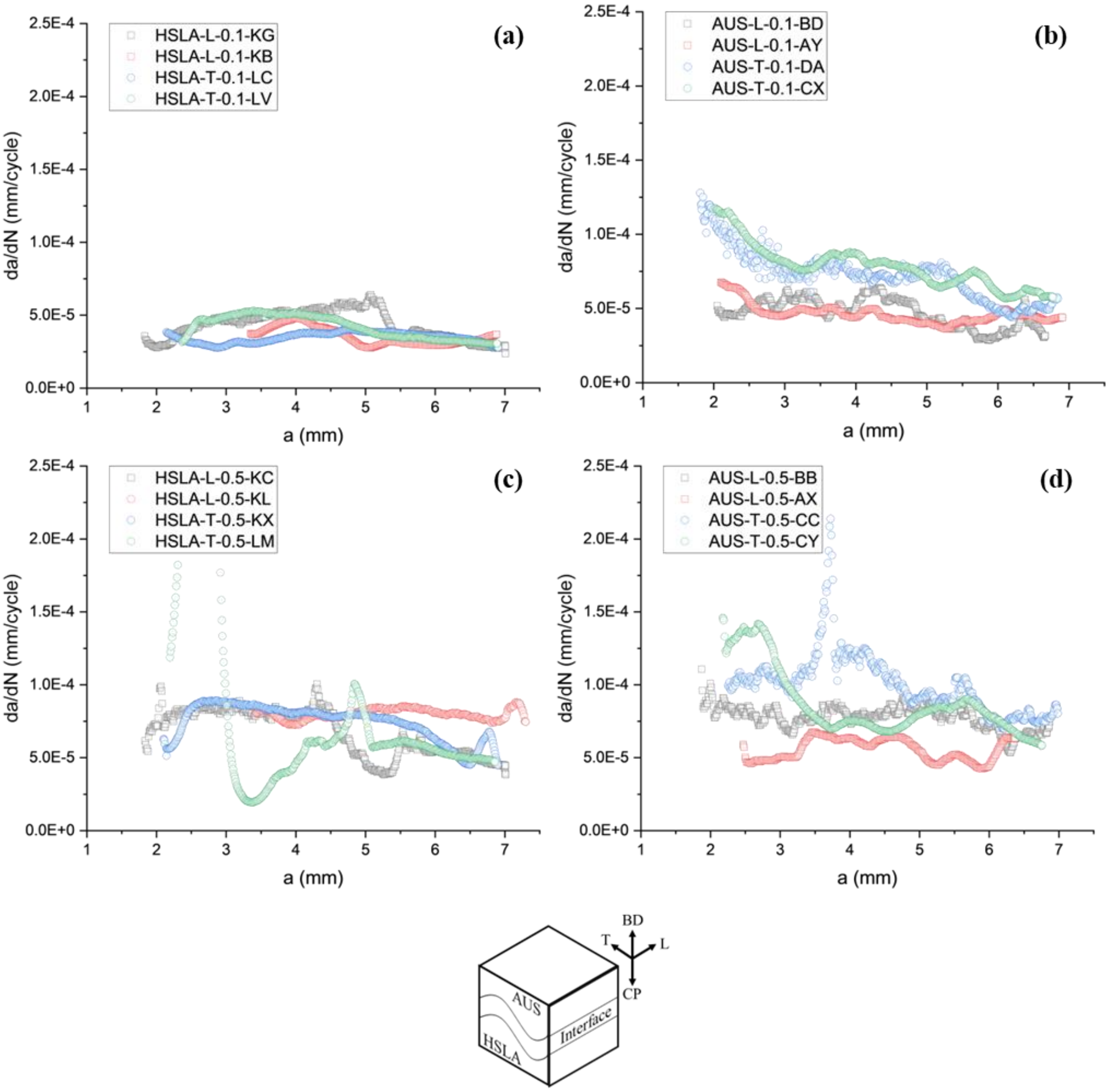

Figure 7.8 Constant ΔK experiments of mono-materials. (a) HSLA steel at R=0.1, (b) AUS steel at R=0.1, (c) HSLA steel at R=0.5, and (d) AUS steel at R=0.5. Two specimens per condition were tested. The test was conducted at 15 Hz.

Table 7.3 The data obtained for constant ΔK experiments shown in Figure 4.7.

Material	R ratio	Average crack growth rate (mm/cycle)	Standard deviation (mm/cycle)
HSLA-L	0.1	3.98E-05	9.43E-06
HSLA-L	0.5	7.24E-05	1.40E-05
HSLA-T	0.1	3.79E-05	7.02E-06
HSLA-T	0.5	6.47E-05	1.77E-05
AUS-L	0.1	4.65E-05	8.12E-06
AUS-L	0.5	6.78E-05	1.35E-05
AUS-T	0.1	7.52E-05	1.59E-05
AUS-T	0.5	9.35E-05	2.28E-05

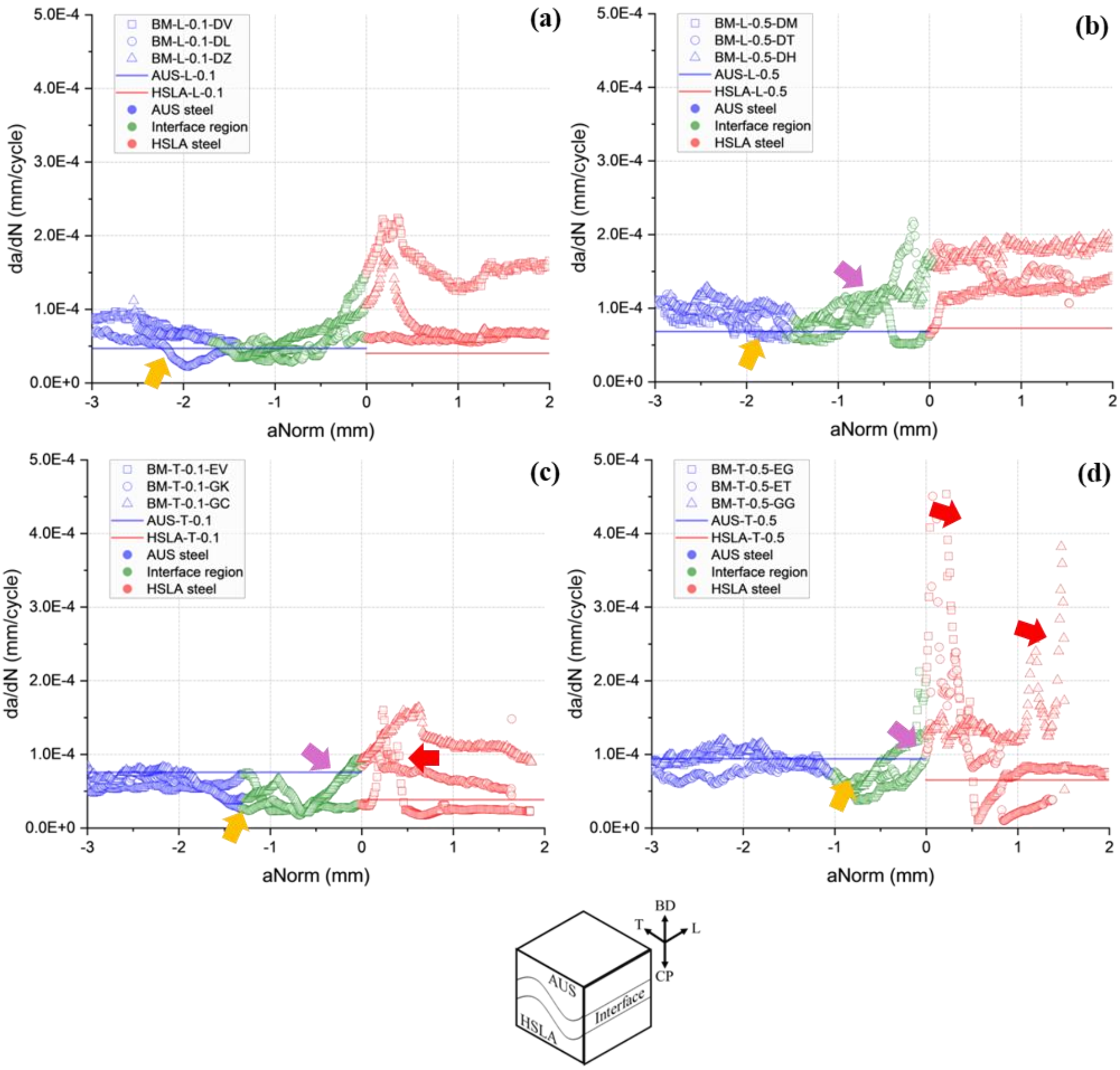

Figure 7.9 The constant ΔK tests with normalised crack length. (a) and (b) are L-oriented specimens, and (c) and (d) are T-oriented specimens. (a) and (c) are under R=0.1, and (b) and (d) and under R=0.5. The reference lines of constant ΔK tests of mono-materials are shown as well. The tests were conducted at ΔK = 20 MPa√m and frequency of 15 Hz. Three repetitions per condition are shown in this figure. This figure is at a lower scale version of Figure 4.11, for better visibility of sudden acceleration.

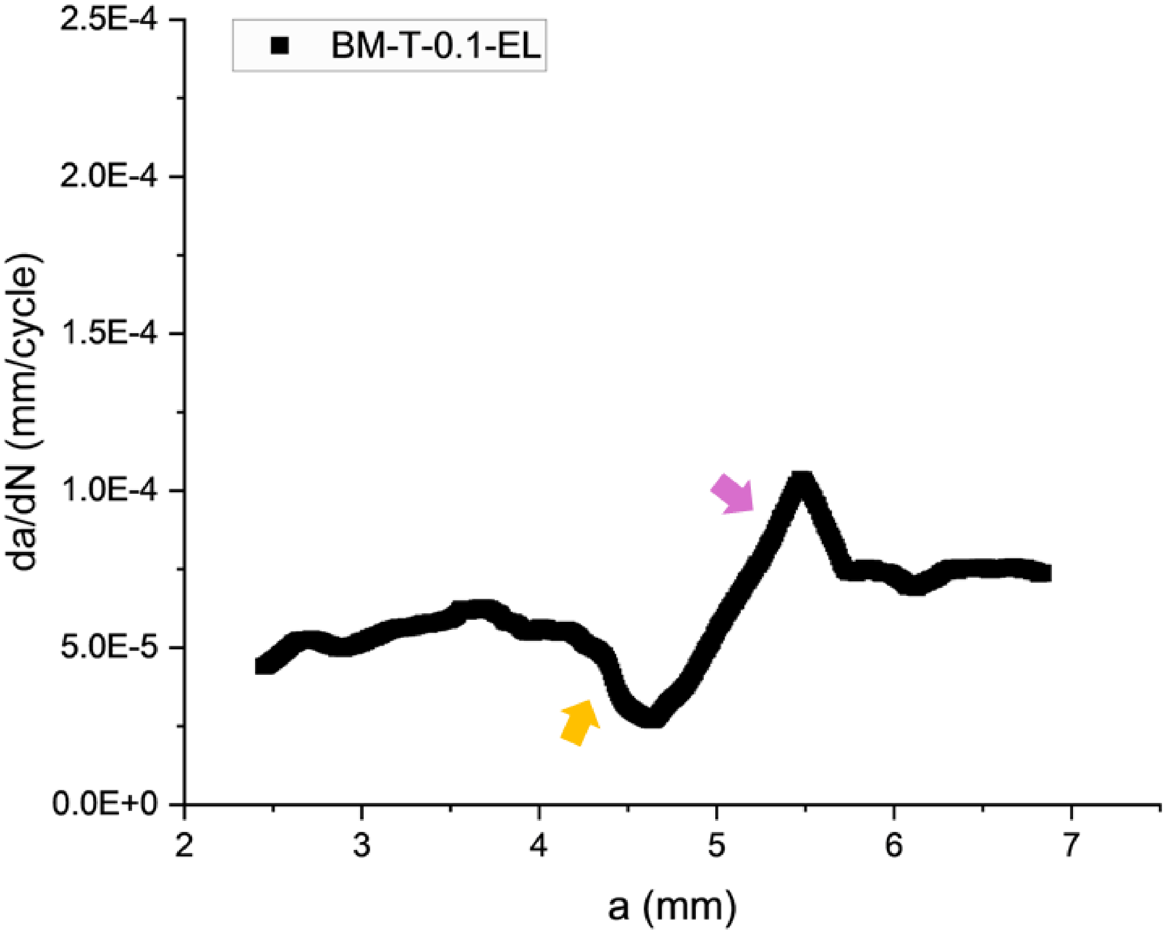

Figure 7.10 The constant ΔK test of a BM without using correction factor. The yellow and purple arrows show the decelerating and accelerating parts of the crack growth curve respectively. The test was conducted at 15 Hz.

7.6. Fractographs

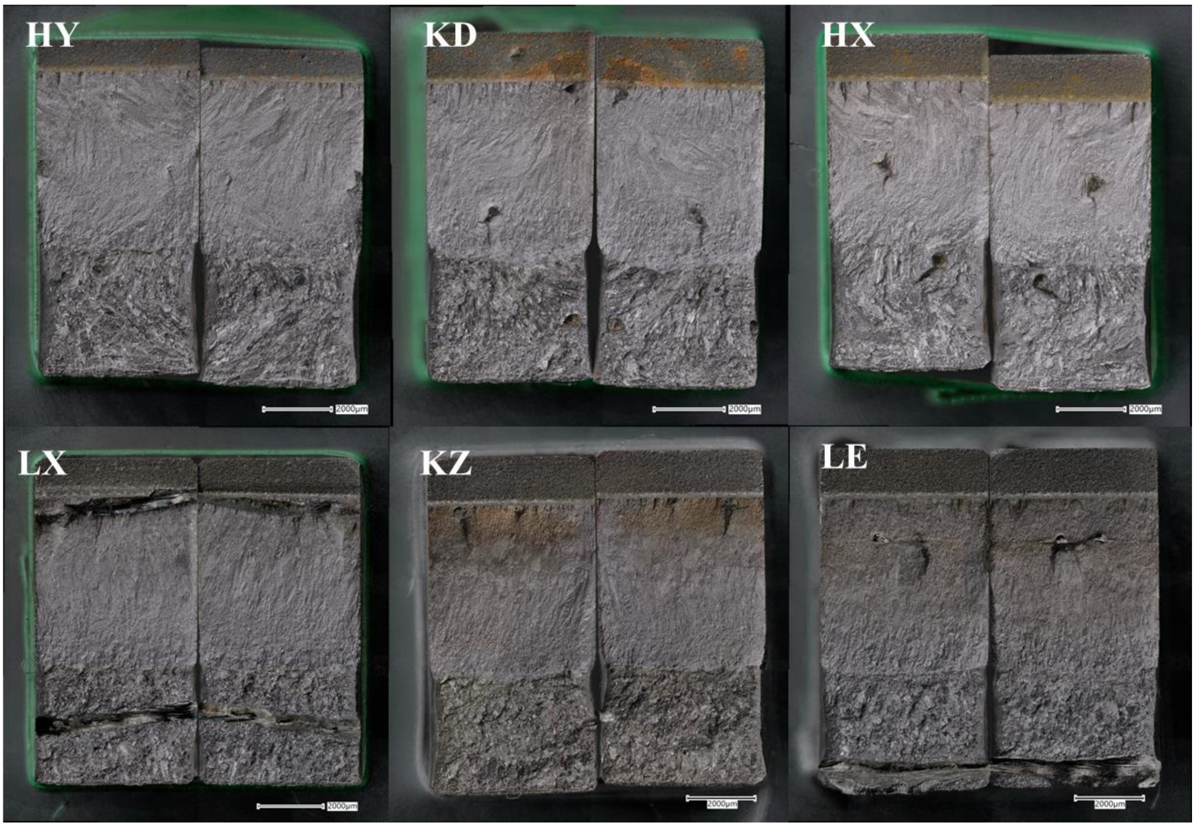

Figure 7.11 Fractographs of constant ΔF tests of HSLA steel. The scale shown is 2000 µm.

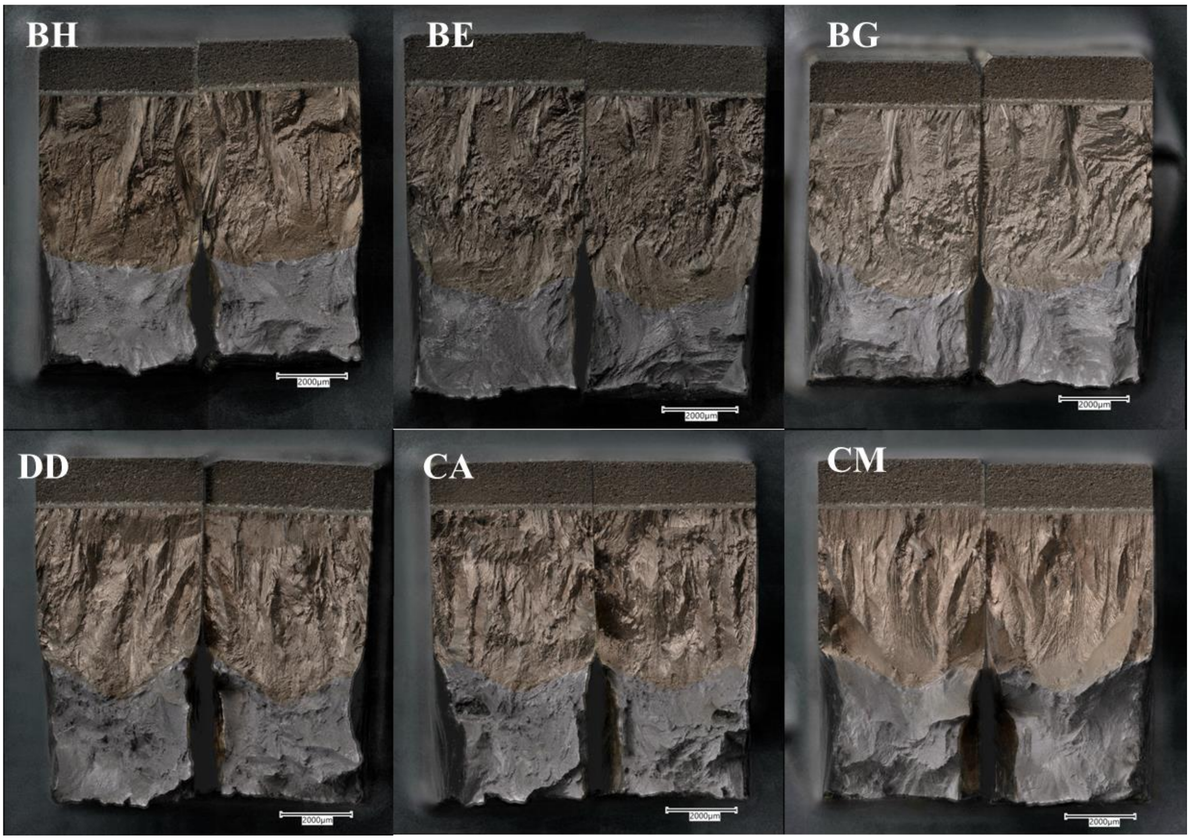

Figure 7.12 Fractographs of constant ΔF tests of AUS steel. The scale shown is 2000 µm.

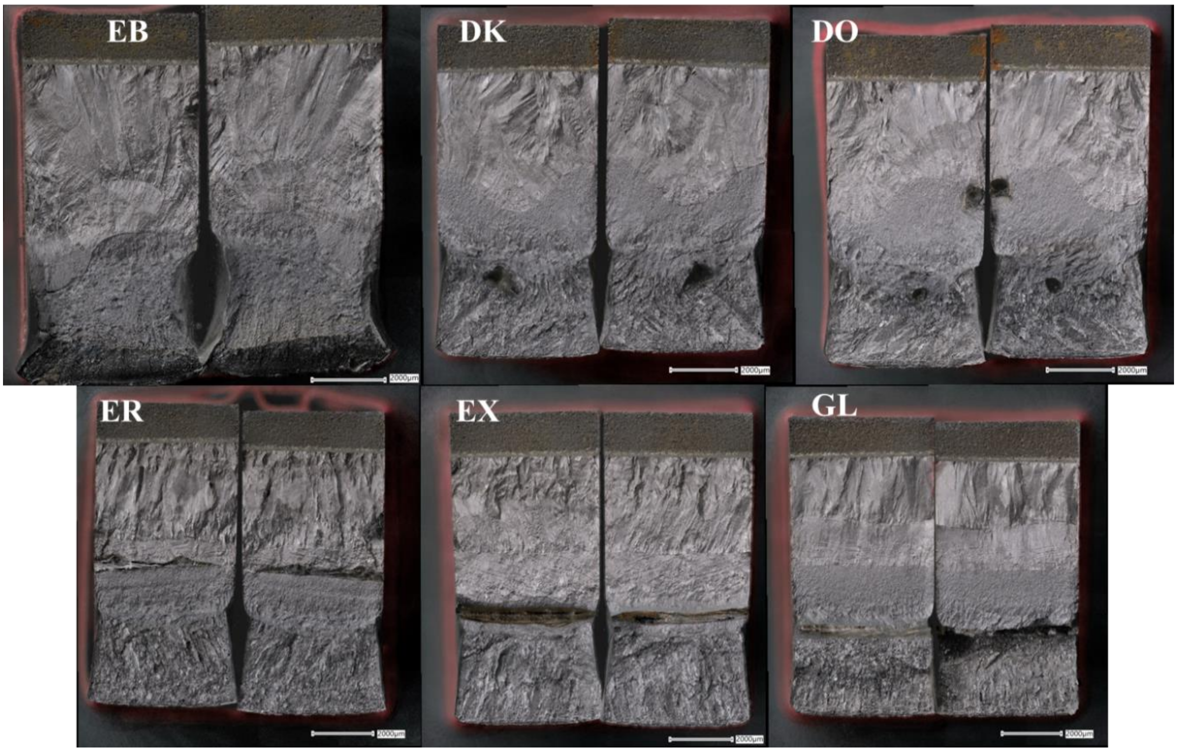

Figure 7.13 Fractographs of constant ΔF tests of BM. The scale shown is 2000 μm.

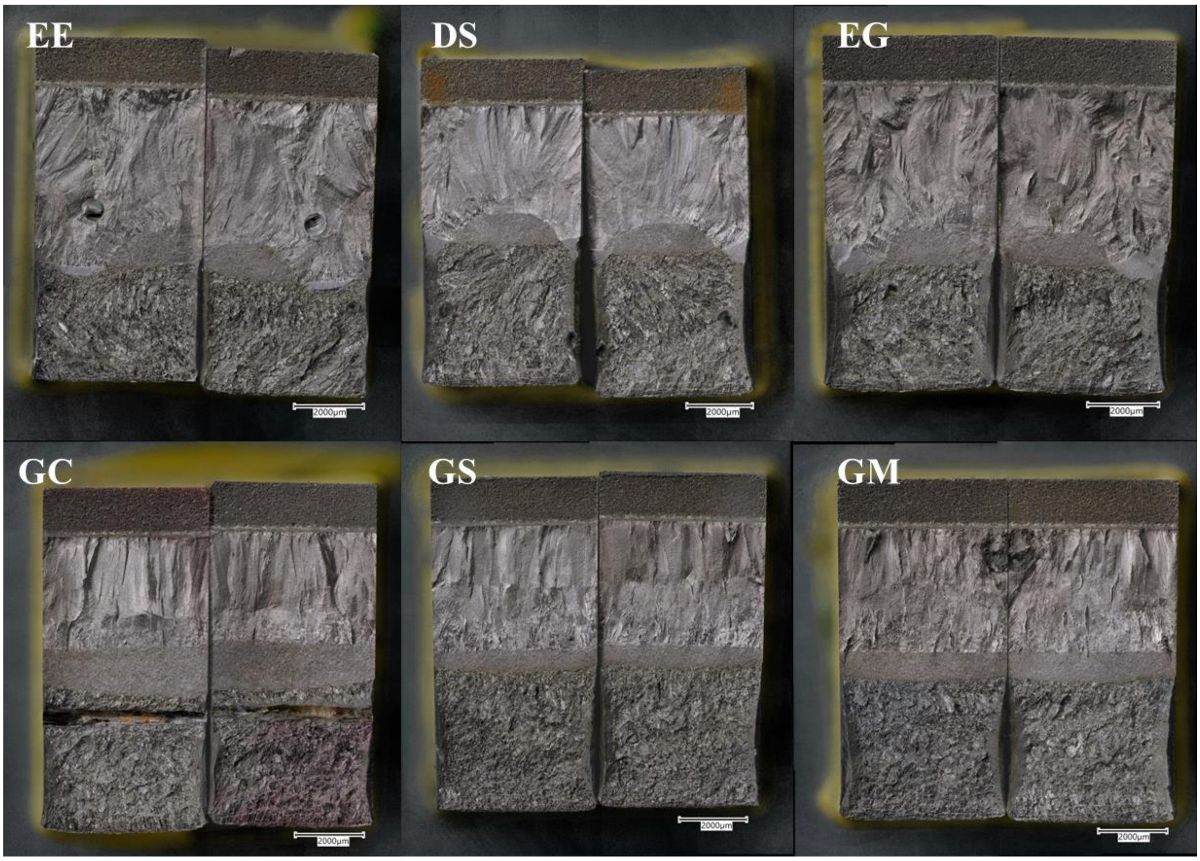

Figure 7.14 Fractographs of threshold stress intensity range of BM. The scale shown is 2000 μm.

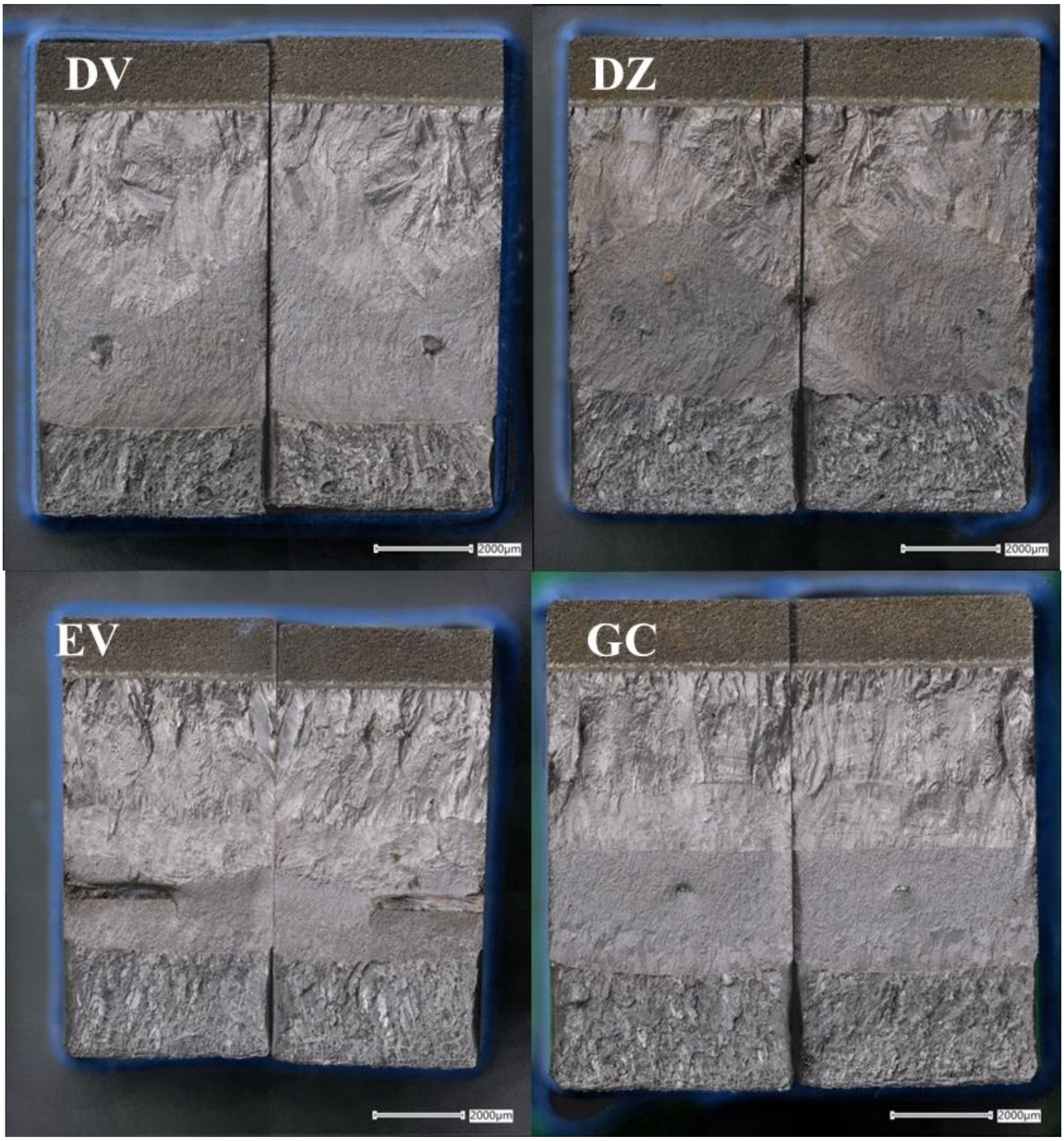

Figure 7.15 Fractographs of constant ΔK tests at R=0.1 of BM. The scale shown is 2000 µm.

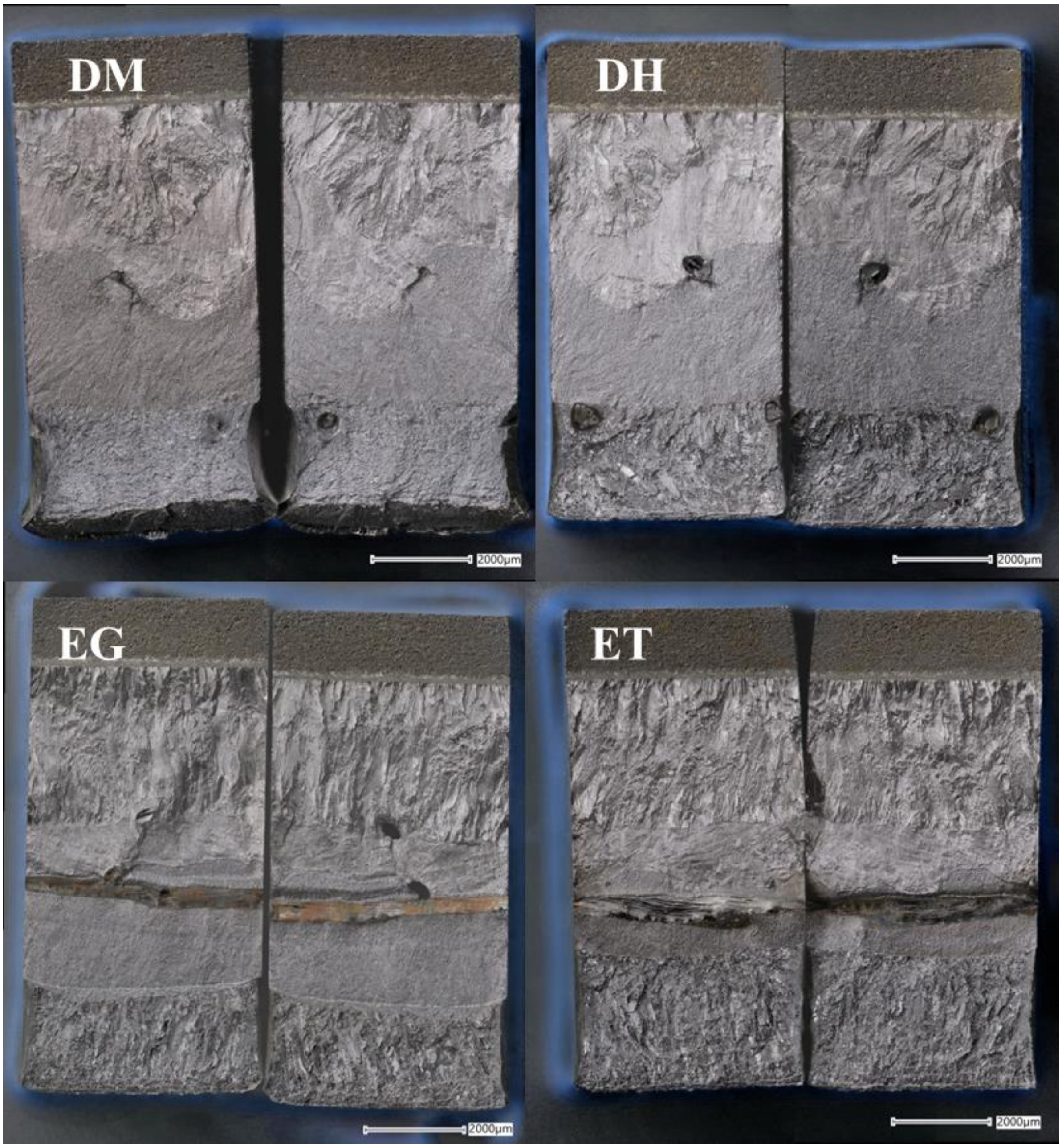

Figure 7.16 Fractographs of constant ΔK tests at R=0.5 of BM. The scale shown is 2000 µm.

References

[1] G. Marinelli, F. Martina, H. Lewtas, D. Hancock, S. Ganguly, and S. Williams, “Functionally graded structures of refractory metals by wire arc additive manufacturing,” *Science and Technology of Welding and Joining*, vol. 24, no. 5, pp. 495–503, 2019, doi: 10.1080/13621718.2019.1586162.

[2] B. Saleh *et al.*, “30 Years of functionally graded materials: An overview of manufacturing methods, Applications and Future Challenges,” *Composites Part B: Engineering*, vol. 201, p. 108376, Nov. 2020, doi: 10.1016/j.compositesb.2020.108376.

[3] C. Zhang *et al.*, “Additive manufacturing of functionally graded materials: A review,” *Materials Science and Engineering: A*, vol. 764, no. May, p. 138209, 2019, doi: 10.1016/j.msea.2019.138209.

[4] B. Zhang, P. Jaiswal, R. Rai, and S. Nelaturi, “Additive Manufacturing of Functionally Graded Material Objects: A Review,” *Journal of Computing and Information Science in Engineering*, vol. 18, no. 4, 2018, doi: 10.1115/1.4039683.

[5] Y. Li *et al.*, “A Review on Functionally Graded Materials and Structures via Additive Manufacturing: From Multi-Scale Design to Versatile Functional Properties,” *Advanced Materials Technologies*, vol. 5, no. 6, 2020, doi: 10.1002/admt.201900981.

[6] A. Reichardt *et al.*, “Advances in additive manufacturing of metal-based functionally graded materials,” *International Materials Reviews*, vol. 66, no. 1, pp. 1–29, 2021, doi: 10.1080/09506608.2019.1709354.

[7] F. I. Azam, A. M. Abdul Rani, K. Altaf, T. V. V. L. N. Rao, and H. A. Zaharin, “An In-Depth Review on Direct Additive Manufacturing of Metals,” *IOP Conf. Ser.: Mater. Sci. Eng.*, vol. 328, p. 012005, Mar. 2018, doi: 10.1088/1757-899X/328/1/012005.

[8] M. Mehrpouya, A. Dehghanghadikolaei, B. Fotovvati, A. Vosooghnia, S. S. Emamian, and A. Gisario, “The Potential of Additive Manufacturing in the Smart Factory Industrial 4.0: A Review,” *Applied Sciences*, vol. 9, no. 18, p. 3865, Sep. 2019, doi: 10.3390/app9183865.

[9] Y. Ayan and N. Kahraman, “Fabrication and characterization of functionally graded material (FGM) structure containing two dissimilar steels (ER70S-6 and 308LSi) by wire arc additive manufacturing (WAAM),” *Materials Today Communications*, vol. 33, p. 104457, Dec. 2022, doi: 10.1016/j.mtcomm.2022.104457.

[10] H. Jahns, J. Unglaub, J. Müller, J. Hensel, and K. Thiele, “Material Behavior of High-Strength Low-Alloy Steel (HSLA) WAAM Walls in Construction,” *Metals*, vol. 13, no. 3, p. 589, Mar. 2023, doi: 10.3390/met13030589.

[11] “Ramlab.” [Online]. Available: https://www.ramlab.com/

[12] David Appleyard, “Welding Pelton Runners.” [Online]. Available: https://www.hydroreview.com/business-finance/welding-pelton-runners/

[13] K. Treutler and V. Wesling, “The Current State of Research of Wire Arc Additive Manufacturing (WAAM): A Review,” *Applied Sciences*, vol. 11, no. 18, p. 8619, Sep. 2021, doi: 10.3390/app11188619.

[14] N. Rodideal, C. M. Machado, V. Infante, D. F. O. Braga, T. G. Santos, and C. Vidal, “Mechanical characterization and fatigue assessment of wire and arc additively manufactured HSLA steel parts,” *International Journal of Fatigue*, vol. 164, p. 107146, Nov. 2022, doi: 10.1016/j.ijfatigue.2022.107146.

[15] P. Dirisu, S. Ganguly, A. Mehmanparast, F. Martina, and S. Williams, “Analysis of fracture toughness properties of wire + arc additive manufactured high strength low

alloy structural steel components," *Materials Science and Engineering: A*, vol. 765, p. 138285, Sep. 2019, doi: 10.1016/j.msea.2019.138285.

[16] C. L. Walters, A. Alvaro, and J. Maljaars, "The effect of low temperatures on the fatigue crack growth of S460 structural steel," *International Journal of Fatigue*, vol. 82, pp. 110–118, Jan. 2016, doi: 10.1016/j.ijfatigue.2015.03.007.

[17] W. Wu, Q. Wang, L. Yang, Z. Liu, X. Li, and Y. Li, "Corrosion and SCC initiation behavior of low-alloy high-strength steels microalloyed with Nb and Sb in a simulated polluted marine atmosphere," *Journal of Materials Research and Technology*, vol. 9, no. 6, pp. 12976–12995, Nov. 2020, doi: 10.1016/j.jmrt.2020.09.033.

[18] N. Venkateswara Rao, G. Madhusudhan Reddy, and S. Nagarjuna, "Weld overlay cladding of high strength low alloy steel with austenitic stainless steel – Structure and properties," *Materials & Design*, vol. 32, no. 4, pp. 2496–2506, Apr. 2011, doi: 10.1016/j.matdes.2010.10.026.

[19] S. Chandrasekaran, S. Hari, and M. Amirthalingam, "Wire arc additive manufacturing of functionally graded material for marine risers," *Materials Science and Engineering: A*, vol. 792, p. 139530, Aug. 2020, doi: 10.1016/j.msea.2020.139530.

[20] J. L. Galán Argumedo, M. Mahmoudiniya, T. E. Reinton, L. A. I. Kestens, M. J. M. Hermans, and V. A. Popovich, "Functional grading of low alloy steel to 316 L by wire arc additive manufacturing – Microstructural and mechanical characterization of bi-metal interface," *Journal of Materials Processing Technology*, vol. 325, p. 118305, Apr. 2024, doi: 10.1016/j.jmatprotec.2024.118305.

[21] T. W. Nelson, J. C. Lippold, and M. J. Mills, "Nature and Evolution of the Fusion Boundary in Ferritic-Austenitic Dissimilar Weld Metals, Part 1 — Nucleation and Growth".

[22] T. W. Nelson, J. C. Lippold, and M. J. Mills, "Nature and Evolution of the Fusion Boundary in Ferritic-Austenitic Dissimilar Metal Welds — Part 2: On-Cooling Transformations".

[23] T. W. Nelson, J. C. Lippold, and M. J. Mills, "Investigation of boundaries and structures in dissimilar metal welds," *Science and Technology of Welding and Joining*, vol. 3, 1998.

[24] F. Erdogan, "Fracture mechanics of functionally graded materials," *Composites Engineering*, vol. 5, no. 7, pp. 753–770, Jan. 1995, doi: 10.1016/0961-9526(95)00029-M.

[25] Z. Jin and R. Batra, "Some basic fracture mechanics concepts in functionally graded materials," *Journal of the Mechanics and Physics of Solids*, vol. 44, no. 8, pp. 1221–1235, Aug. 1996, doi: 10.1016/0022-5096(96)00041-5.

[26] S. A. Meguid, X. D. Wang, and L. Y. Jiang, "On the dynamic propagation of a finite crack in functionally graded materials," *Engineering Fracture Mechanics*, vol. 69, no. 14–16, pp. 1753–1768, Sep. 2002, doi: 10.1016/S0013-7944(02)00046-2.

[27] P. Shanmugavel, G. B. Bhaskar, M. Chandrasekaran, P. S. Mani, and S. P. Srinivasan, "An Overview of Fracture Analysis in Functionally Graded Materials".

[28] S. Suresh, "Graded Materials for Resistance to Contact Deformation and Damage," *Science*, vol. 292, no. 5526, pp. 2447–2451, Jun. 2001, doi: 10.1126/science.1059716.

[29] Y. Li *et al.*, "A Review on Functionally Graded Materials and Structures via Additive Manufacturing: From Multi-Scale Design to Versatile Functional Properties," *Adv. Mater. Technol.*, vol. 5, no. 6, p. 1900981, Jun. 2020, doi: 10.1002/admt.201900981.

[30] B. Zhang, P. Jaiswal, R. Rai, and S. Nelaturi, "Additive Manufacturing of Functionally Graded Material Objects: A Review," *Journal of Computing and Information Science in Engineering*, vol. 18, no. 4, p. 041002, Dec. 2018, doi: 10.1115/1.4039683.

[31] C. Zhang *et al.*, "Additive manufacturing of functionally graded materials: A review," *Materials Science and Engineering: A*, vol. 764, p. 138209, Sep. 2019, doi: 10.1016/j.msea.2019.138209.

[32] U. Schulz, M. Peters, Fr.-W. Bach, and G. Tegeder, "Graded coatings for thermal, wear and corrosion barriers," *Materials Science and Engineering: A*, vol. 362, no. 1, pp. 61–80, Dec. 2003, doi: 10.1016/S0921-5093(03)00579-3.

[33] X. Li, L. Lu, J. Li, X. Zhang, and H. Gao, "Mechanical properties and deformation mechanisms of gradient nanostructured metals and alloys," *Nat Rev Mater*, vol. 5, no. 9, Art. no. 9, Sep. 2020, doi: 10.1038/s41578-020-0212-2.

[34] S. Ghorbanpour *et al.*, "Additive manufacturing of functionally graded inconel 718: Effect of heat treatment and building orientation on microstructure and fatigue behaviour," *Journal of Materials Processing Technology*, vol. 306, p. 117573, Aug. 2022, doi: 10.1016/j.jmatprotec.2022.117573.

[35] A. A. B. Fogliatto, C. H. Ahrens, P. A. P. Wendhausen, E. C. Santos, and D. Rodrigues, "Correlation between porosity and permeability of stainless steel filters with gradient porosity produced by SLS/SLM," *Rapid Prototyping Journal*, vol. 26, no. 1, pp. 73–81, Jan. 2019, doi: 10.1108/RPJ-09-2018-0224.

[36] B. Tomar, S. Shiva, and T. Nath, "A review on wire arc additive manufacturing: Processing parameters, defects, quality improvement and recent advances," *Materials Today Communications*, vol. 31, p. 103739, Jun. 2022, doi: 10.1016/j.mtcomm.2022.103739.

[37] B. Wu *et al.*, "A review of the wire arc additive manufacturing of metals: properties, defects and quality improvement," *Journal of Manufacturing Processes*, vol. 35, pp. 127–139, Oct. 2018, doi: 10.1016/j.jmapro.2018.08.001.

[38] T. Artaza *et al.*, "Design and integration of WAAM technology and in situ monitoring system in a gantry machine," *Procedia Manufacturing*, vol. 13, pp. 778–785, 2017, doi: 10.1016/j.promfg.2017.09.184.

[39] W. Zhang, X. Shang, S. Chen, and L. Zhang, "Comparison of microstructural characteristics and mechanical properties of the high-strength low-alloy steels fabricated by wire arc additive manufacturing versus conventional casting," *Materials Science and Engineering: A*, vol. 885, p. 145593, Oct. 2023, doi: 10.1016/j.msea.2023.145593.

[40] P. Long, D. Wen, J. Min, Z. Zheng, J. Li, and Y. Liu, "Microstructure Evolution and Mechanical Properties of a Wire-Arc Additive Manufactured Austenitic Stainless Steel: Effect of Processing Parameter," *Materials*, vol. 14, no. 7, Art. no. 7, Jan. 2021, doi: 10.3390/ma14071681.

[41] M. S. Rashid, "High-Strength, Low-Alloy Steels," *Science*, vol. 208, no. 4446, pp. 862–869, May 1980, doi: 10.1126/science.208.4446.862.

[42] T. A. Rodrigues *et al.*, "In-situ strengthening of a high strength low alloy steel during Wire and Arc Additive Manufacturing (WAAM)," *Additive Manufacturing*, vol. 34, p. 101200, Aug. 2020, doi: 10.1016/j.addma.2020.101200.

[43] T. A. Rodrigues, V. Duarte, J. A. Avila, T. G. Santos, R. M. Miranda, and J. P. Oliveira, "Wire and arc additive manufacturing of HSLA steel: Effect of thermal cycles on microstructure and mechanical properties," *Additive Manufacturing*, vol. 27, pp. 440–450, May 2019, doi: 10.1016/j.addma.2019.03.029.

[44] Q. Fang, L. Zhao, C. Chen, Y. Zhu, Y. Peng, and F. Yin, "Effect of heat input on microstructural and mechanical properties of high strength low alloy steel block parts fabricated by wire arc additive manufacturing," *Materials Today*

Communications, vol. 34, p. 105146, Mar. 2023, doi: 10.1016/j.mtcomm.2022.105146.

[45] A. S. Yildiz, K. Davut, B. Koc, and O. Yilmaz, “Wire arc additive manufacturing of high-strength low alloy steels: study of process parameters and their influence on the bead geometry and mechanical characteristics,” *Int J Adv Manuf Technol*, vol. 108, no. 11–12, pp. 3391–3404, Jun. 2020, doi: 10.1007/s00170-020-05482-9.

[46] W. Kingkam, C.-Z. Zhao, H. Li, H.-X. Zhang, and Z.-M. Li, “Hot Deformation and Corrosion Resistance of High-Strength Low-Alloy Steel,” *Acta Metall. Sin. (Engl. Lett.)*, vol. 32, no. 4, pp. 495–505, Apr. 2019, doi: 10.1007/s40195-018-0797-2.

[47] W. Liu, Q. Zhou, L. Li, Z. Wu, F. Cao, and Z. Gao, “Effect of alloy element on corrosion behavior of the huge crude oil storage tank steel in seawater,” *Journal of Alloys and Compounds*, vol. 598, pp. 198–204, Jun. 2014, doi: 10.1016/j.jallcom.2014.01.181.

[48] G. H. Majzoobi, A. H. Mahmoudi, and S. Moradi, “Ductile to brittle failure transition of HSLA-100 Steel at high strain rates and subzero temperatures,” *Engineering Fracture Mechanics*, vol. 158, pp. 179–193, Jun. 2016, doi: 10.1016/j.engfracmech.2016.03.001.

[49] J. C. Lippold and D. J. Kotecki, *Welding metallurgy and weldability of stainless steels*. Hoboken, NJ: John Wiley, 2005.

[50] L. P. Karjalainen, T. Taulavuori, M. Sellman, and A. Kyröläinen, “Some Strengthening Methods for Austenitic Stainless Steels,” *steel research international*, vol. 79, no. 6, pp. 404–412, Jun. 2008, doi: 10.1002/srin.200806146.

[51] A. S. Kumar, S. K. Sharma, and A. K. Shukla, “Microstructural, Mechanical, and Thermal Analysis of SS316L Weldment for Marine Engineering Application,” *J. of Materi Eng and Perform*, Nov. 2023, doi: 10.1007/s11665-023-08906-1.

[52] W. Jin, C. Zhang, S. Jin, Y. Tian, D. Wellmann, and W. Liu, “Wire Arc Additive Manufacturing of Stainless Steels: A Review,” *Applied Sciences*, vol. 10, no. 5, p. 1563, Feb. 2020, doi: 10.3390/app10051563.

[53] A. Karpagaraj, S. Baskaran, T. Arunnellaiappan, and N. R. Kumar, “A review on the suitability of wire arc additive manufacturing (WAAM) for stainless steel 316,” presented at the ADVANCES IN MECHANICAL DESIGN, MATERIALS AND MANUFACTURE: Proceeding of the Second International Conference on Design, Materials and Manufacture (ICDEM 2019), Surathkal, India, 2020, p. 050001. doi: 10.1063/5.0004148.

[54] V. Laghi, M. Palermo, L. Tonelli, G. Gasparini, L. Ceschini, and T. Trombetti, “Tensile properties and microstructural features of 304L austenitic stainless steel produced by wire-and-arc additive manufacturing,” *Int J Adv Manuf Technol*, vol. 106, no. 9–10, pp. 3693–3705, Feb. 2020, doi: 10.1007/s00170-019-04868-8.

[55] C. Jing *et al.*, “Improving mechanical strength and isotropy for wire-arc additive manufactured 304L stainless steels via controlling arc heat input,” *Materials Science and Engineering: A*, vol. 845, p. 143223, Jun. 2022, doi: 10.1016/j.msea.2022.143223.

[56] D. Kumar, S. Jhavar, A. Arya, K. G. Prashanth, and S. Suwas, “Mechanisms controlling fracture toughness of additively manufactured stainless steel 316L,” *Int J Fract*, vol. 235, no. 1, pp. 61–78, May 2022, doi: 10.1007/s10704-021-00574-3.

[57] L. Wang, J. Xue, and Q. Wang, “Correlation between arc mode, microstructure, and mechanical properties during wire arc additive manufacturing of 316L stainless steel,” *Materials Science and Engineering: A*, vol. 751, pp. 183–190, Mar. 2019, doi: 10.1016/j.msea.2019.02.078.

[58] B. Xie, J. Xue, and X. Ren, “Wire Arc Deposition Additive Manufacturing and Experimental Study of 316L Stainless Steel by CMT + P Process,” *Metals*, vol. 10, no. 11, p. 1419, Oct. 2020, doi: 10.3390/met10111419.

[59] J. S. Zuback, T. A. Palmer, and T. DebRoy, “Additive manufacturing of functionally graded transition joints between ferritic and austenitic alloys,” *Journal of Alloys and Compounds*, vol. 770, pp. 995–1003, Jan. 2019, doi: 10.1016/j.jallcom.2018.08.197.

[60] G. Shin *et al.*, “Microstructural evolution and mechanical properties of functionally graded austenitic–low-carbon steel produced via directed energy deposition,” *Materials & Design*, vol. 227, p. 111681, Mar. 2023, doi: 10.1016/j.matdes.2023.111681.

[61] J. N. DuPont, “Microstructural evolution and high temperature failure of ferritic to austenitic dissimilar welds,” *International Materials Reviews*, vol. 57, no. 4, pp. 208–234, Jul. 2012, doi: 10.1179/1743280412Y.0000000006.

[62] A. Yadav, M. Srivastava, P. K. Jain, and S. Rathee, “Functionally graded deposition of dissimilar steel (316LSi and ER70S-6) fabricated through twin-wire arc additive manufacturing,” *Materials Letters*, vol. 354, p. 135395, Jan. 2024, doi: 10.1016/j.matlet.2023.135395.

[63] Q. Wang *et al.*, “Study of type-II boundary behavior during SA508-3/EQ309L overlay weld interfacial failure process,” *Journal of Materials Processing Technology*, vol. 247, pp. 64–72, Sep. 2017, doi: 10.1016/j.jmatprotec.2017.04.009.

[64] Md. R. U. Ahsan, A. N. M. Tanvir, T. Ross, A. Elsawy, M.-S. Oh, and D. B. Kim, “Fabrication of bimetallic additively manufactured structure (BAMS) of low carbon steel and 316L austenitic stainless steel with wire + arc additive manufacturing,” *Rapid Prototyping Journal*, vol. 26, no. 3, pp. 519–530, Jan. 2020, doi: 10.1108/RPJ-09-2018-0235.

[65] A. Suárez, A. Panfilo, E. Aldalur, F. Veiga, and P. Gomez, “Microstructure and mechanical properties of mild steel-stainless steel bimetallic structures built using Wire Arc Additive Manufacturing,” *CIRP Journal of Manufacturing Science and Technology*, vol. 38, pp. 769–773, Aug. 2022, doi: 10.1016/j.cirpj.2022.06.018.

[66] U. Gürol, B. Turgut, N. Güleçyüz, S. DiLiBal, and M. Koçak, “DEVELOPMENT OF MULTI-MATERIAL COMPONENTS VIA ROBOTIC WIRE ARC ADDITIVE MANUFACTURING,” *International Journal of 3D Printing Technologies and Digital Industry*, vol. 5, no. 3, pp. 721–729, Dec. 2021, doi: 10.46519/ij3dptdi.1033374.

[67] J. Schijve, *Fatigue of structures and materials*, 2. ed. [Nachdr.]. Dordrecht: Springer, 2010.

[68] A. Ermakova, A. Mehmanparast, and S. Ganguly, “A review of present status and challenges of using additive manufacturing technology for offshore wind applications,” *Procedia Structural Integrity*, vol. 17, pp. 29–36, 2019, doi: 10.1016/j.prostr.2019.08.005.

[69] M. Kamal and M. M. Rahman, “Advances in fatigue life modeling: A review,” *Renewable and Sustainable Energy Reviews*, vol. 82, pp. 940–949, Feb. 2018, doi: 10.1016/j.rser.2017.09.047.

[70] E08 Committee, “Test Method for Measurement of Fatigue Crack Growth Rates.” ASTM International. doi: 10.1520/E0647-23.

[71] ISO/TC 164/SC 4 Technical Committee, “Metallic materials - Fatigue testing - Fatigue crack growth method.” ISO. [Online]. Available: https://www.iso.org/standard/73809.html

[72] Z.-H. Jin and N. Noda, “Crack-Tip Singular Fields in Nonhomogeneous Materials,” *Journal of Applied Mechanics*, vol. 61, no. 3, pp. 738–740, Sep. 1994, doi: 10.1115/1.2901529.

[73] P. Gu and R. J. Asaro, "Crack deflection in functionally graded materials," *International Journal of Solids and Structures*, vol. 34, no. 24, pp. 3085–3098, Aug. 1997, doi: 10.1016/S0020-7683(96)00175-8.

[74] T. Honein and G. Herrmann, "Conservation laws in nonhomogeneous plane elastostatics," *Journal of the Mechanics and Physics of Solids*, vol. 45, no. 5, pp. 789–805, May 1997, doi: 10.1016/S0022-5096(96)00087-7.

[75] S. Ghorbanpour *et al.*, "Effect of microstructure induced anisotropy on fatigue behaviour of functionally graded Inconel 718 fabricated by additive manufacturing," *Materials Characterization*, vol. 179, p. 111350, Sep. 2021, doi: 10.1016/j.matchar.2021.111350.

[76] M. Janssen, J. Zuidema, and R. Wanhill, *Fracture Mechanics: Fundamentals and Applications*, 0 ed. CRC Press, 2004. doi: 10.1201/9781482265583.

[77] A. Ermakova, A. Mehmanparast, S. Ganguly, N. Razavi, and F. Berto, "Fatigue crack growth behaviour of wire and arc additively manufactured ER70S-6 low carbon steel components," *Int J Fract*, vol. 235, no. 1, pp. 47–59, May 2022, doi: 10.1007/s10704-021-00545-8.

[78] M. Shamir *et al.*, "Assessment of mechanical and fatigue crack growth properties of wire + arc additively manufactured mild steel components," *Fatigue & Fracture of Engineering Materials & Structures*, vol. 45, no. 10, pp. 2978–2989, 2022, doi: 10.1111/ffe.13797.

[79] C. Huang, Y. Zheng, T. Chen, E. Ghafoori, and L. Gardner, "Fatigue crack growth behaviour of wire arc additively manufactured steels," *International Journal of Fatigue*, vol. 173, p. 107705, Aug. 2023, doi: 10.1016/j.ijfatigue.2023.107705.

[80] A. F. Hobbacher, *Recommendations for Fatigue Design of Welded Joints and Components*. in IIW Collection. Cham: Springer International Publishing, 2016. doi: 10.1007/978-3-319-23757-2.

[81] V. Ajay, J. Nakrani, N. K. Mishra, and A. Shrivastava, "Anisotropic fatigue crack propagation in wire arc additively manufactured 316L stainless steel," *International Journal of Fatigue*, vol. 177, p. 107976, Dec. 2023, doi: 10.1016/j.ijfatigue.2023.107976.

[82] J. V. Gordon, C. V. Haden, H. F. Nied, R. P. Vinci, and D. G. Harlow, "Fatigue crack growth anisotropy, texture and residual stress in austenitic steel made by wire and arc additive manufacturing," *Materials Science and Engineering: A*, vol. 724, pp. 431–438, May 2018, doi: 10.1016/j.msea.2018.03.075.

[83] A. Riemer, S. Leuders, M. Thöne, H. A. Richard, T. Tröster, and T. Niendorf, "On the fatigue crack growth behavior in 316L stainless steel manufactured by selective laser melting," *Engineering Fracture Mechanics*, vol. 120, pp. 15–25, Apr. 2014, doi: 10.1016/j.engfracmech.2014.03.008.

[84] M. Nani Babu, G. Sasikala, and S. K. Albert, "High-Temperature Fatigue Crack Growth Behaviour of SS 316LN," in *Proceedings of Fatigue, Durability and Fracture Mechanics*, S. Seetharamu, K. B. S. Rao, and R. W. Khare, Eds., in Lecture Notes in Mechanical Engineering. , Singapore: Springer Singapore, 2018, pp. 413–422. doi: 10.1007/978-981-10-6002-1_33.

[85] K. G. Samuel, G. Sasikala, and S. K. Ray, "On R ratio dependence of threshold stress intensity factor range for fatigue crack growth in type 316(N) stainless steel weld," *Materials Science and Technology*, vol. 27, no. 1, pp. 371–376, Jan. 2011, doi: 10.1179/026708310X12699498463048.

[86] A. Poonguzhali, M. N. Babu, S. Ravi, S. Ningshen, and G. Amarendra, "Effect of Environment on Fatigue Crack Growth Behavior of Type 316 LN Stainless Steel and

its Weldments," *J. of Materi Eng and Perform*, vol. 31, no. 5, pp. 3918–3929, May 2022, doi: 10.1007/s11665-021-06496-4.

[87] W. Elber, "The Significance of Fatigue Crack Closure," in *Damage Tolerance in Aircraft Structures*, M. Rosenfeld, Ed., 100 Barr Harbor Drive, PO Box C700, West Conshohocken, PA 19428-2959: ASTM International, 1971, pp. 230-230–13. doi: 10.1520/STP26680S.

[88] R. Pippan and A. Hohenwarter, "Fatigue crack closure: a review of the physical phenomena," *Fatigue Fract Eng Mater Struct*, vol. 40, no. 4, pp. 471–495, Apr. 2017, doi: 10.1111/ffe.12578.

[89] I. Roth, M. Kübbeler, U. Krupp, H.-J. Christ, and C.-P. Fritzen, "Crack initiation and short crack growth in metastable austenitic stainless steel in the high cycle fatigue regime," *Procedia Engineering*, vol. 2, no. 1, pp. 941–948, Apr. 2010, doi: 10.1016/j.proeng.2010.03.102.

[90] S. Dhar, "Fatigue crack closure in the near-threshold level in a high-strength low-alloy structural steel," *Theoretical and Applied Fracture Mechanics*, vol. 11, no. 1, pp. 21–25, Apr. 1989, doi: 10.1016/0167-8442(89)90022-0.

[91] K. Vor, C. Sarrazin-Baudoux, C. Gardin, and J. Petit, "Wake history effect on closure of short and long fatigue crack in 304L stainless steel," *Procedia Engineering*, vol. 2, no. 1, pp. 2327–2336, Apr. 2010, doi: 10.1016/j.proeng.2010.03.249.

[92] F. Jiang, Z. L. Deng, K. Zhao, and J. Sun, "Fatigue crack propagation normal to a plasticity mismatched bimaterial interface," *Materials Science and Engineering: A*, vol. 356, no. 1, pp. 258–266, Sep. 2003, doi: 10.1016/S0921-5093(03)00142-4.

[93] R. Cortés, N. K. Rodríguez, R. R. Ambriz, V. H. López, A. Ruiz, and D. Jaramillo, "Fatigue and crack growth behavior of Inconel 718–AL6XN dissimilar welds," *Materials Science and Engineering: A*, vol. 745, pp. 20–30, Feb. 2019, doi: 10.1016/j.msea.2018.12.087.

[94] M. S. Duval-Chaneac *et al.*, "Fatigue crack growth in IN718/316L multi-materials layered structures fabricated by laser powder bed fusion," *International Journal of Fatigue*, vol. 152, p. 106454, Nov. 2021, doi: 10.1016/j.ijfatigue.2021.106454.

[95] R. Pippan and F. O. Riemelmoser, "Fatigue of bimaterials. Investigation of the plastic mismatch in case of cracks perpendicular to the interface," *Computational Materials Science*, vol. 13, no. 1, pp. 108–116, Dec. 1998, doi: 10.1016/S0927-0256(98)00051-2.

[96] R. Pippan, K. Flechsig, and F. O. Riemelmoser, "Fatigue crack propagation behavior in the vicinity of an interface between materials with different yield stresses," *Materials Science and Engineering: A*, vol. 283, no. 1, pp. 225–233, May 2000, doi: 10.1016/S0921-5093(00)00703-6.

[97] AWS, A., "9/A5. 9M: 2012: Specification for Bare Stainless Steel Welding Electrodes and Rods." 2012.

[98] AWS, A., "18/A5. 18M: 2005: Specification for carbon steel electrodes and rods for gas shielded arc welding." Miami, 2005.

[99] D. Xie *et al.*, "A Review on Distortion and Residual Stress in Additive Manufacturing," *Chinese Journal of Mechanical Engineering: Additive Manufacturing Frontiers*, vol. 1, no. 3, p. 100039, Sep. 2022, doi: 10.1016/j.cjmeam.2022.100039.

[100] E08 Committee, "Test Method for Linear-Elastic Plane-Strain Fracture Toughness of Metallic Materials." ASTM International. doi: 10.1520/E0399-22.

[101] N. Macallister *et al.*, "Sub-size specimen testing for near-threshold fatigue crack behaviour of additively manufactured Ti-6Al-4V," *Materialia*, vol. 30, p. 101852, Aug. 2023, doi: 10.1016/j.mtla.2023.101852.

[102] E04 Committee, “Test Methods for Determining Average Grain Size.” ASTM International. doi: 10.1520/E0112-13R21.

[103] N. Saeidi, F. Ashrafizadeh, B. Niroumand, and F. Barlat, “EBSD Study of Damage Mechanisms in a High-Strength Ferrite-Martensite Dual-Phase Steel,” *J. of Materi Eng and Perform*, vol. 24, no. 1, pp. 53–58, Jan. 2015, doi: 10.1007/s11665-014-1257-4.

[104] D. F. Martelo, A. Mateo, and M. D. Chapetti, “Crack closure and fatigue crack growth near threshold of a metastable austenitic stainless steel,” *International Journal of Fatigue*, vol. 77, pp. 64–77, Aug. 2015, doi: 10.1016/j.ijfatigue.2015.02.016.

[105] A. Baghdadchi, V. A. Hosseini, and L. Karlsson, “Identification and quantification of martensite in ferritic-austenitic stainless steels and welds,” *Journal of Materials Research and Technology*, vol. 15, pp. 3610–3621, Nov. 2021, doi: 10.1016/j.jmrt.2021.09.153.

[106] Z. Mei and J. W. Morris, “Influence of deformation-induced martensite on fatigue crack propagation in 304-type steels,” *Metall Trans A*, vol. 21, no. 12, pp. 3137–3152, Dec. 1990, doi: 10.1007/BF02647310.

[107] P. Kumar, R. Jayaraj, Z. Zhu, R. L. Narayan, and U. Ramamurty, “Role of metastable austenite in the fatigue resistance of 304L stainless steel produced by laser-based powder bed fusion,” *Materials Science and Engineering: A*, vol. 837, p. 142744, Mar. 2022, doi: 10.1016/j.msea.2022.142744.

[108] M. Jambor *et al.*, “Anomalous fatigue crack propagation behavior in near-threshold region of L-PBF prepared austenitic stainless steel,” *Materials Science and Engineering: A*, vol. 872, p. 144982, May 2023, doi: 10.1016/j.msea.2023.144982.